Environment International 125 (2019) 200–228

Contents lists available at ScienceDirect

Environment International

journal homepage: www.elsevier.com/locate/envint

Review article

Titanium oxide based photocatalytic materials development and their role of in the air pollutants degradation: Overview and forecast

Chi Him A. Tsang[a,b,c], Kai Li[a], Yuxuan Zeng[a], Wei Zhao[d], Tao Zhang[a,b,*], Yujie Zhan[a], Ruijie Xie[a], Dennis Y.C. Leung[d,**], Haibao Huang[a,b,c,*]

[a] School of Environmental Sciences and Engineering, Sun Yat-Sen University, Guangzhou, China
[b] Guangdong-Hong Kong Joint Research Center for Air Pollution Control, China
[c] Guangdong Provincial Key Laboratory of Environmental Pollution Control and Remediation Technology, Guangzhou, China
[d] Department of Mechanical Engineering, The University of Hong Kong, Hong Kong

ARTICLE INFO

Handling Editor: Robert Letcher

Keywords:
TiO_2
Photocatalyst
Doping
Photocatalytic oxidation
Air pollutant
VOCs

ABSTRACT

Due to the anthropogenic pollution, especially the environmental crisis caused by air pollutants, the development of air pollutant degradation photocatalyst has become one of the major directions to the crisis relief. Among them, titania (titanium dioxide, TiO_2) family materials were extensively studied in the past two decades due to their strong activity in the photocatalytic reactions. However, TiO_2 had a drawback of large bandgap which limited its applications, several modification techniques were hence developed to enhance its catalytic activity and light sensitivity. In recent years, other metal oxide based materials have been developed as replacements for TiO_2 photocatalysts. In this review, background information and developments from pure TiO_2 to chemically modified TiO_2-based materials as photocatalysts were discussed in detail, which covered their basic properties and their role in the air pollutant removal. It also proposes to solve the shortcomings of TiO_2 by developing other metal oxide-based materials and predict the future development of TiO_2 materials in future environmental applications.

1. Introduction

Behind the rapid development of the society due to urbanization and industrialization all over the world including China in the past decades, many environmental problems have arisen (Wang et al., 2016; Huang et al., 2017a; Guo et al., 2017; Shu et al., 2018), especially the air pollution caused by different kinds of chemical generally produced from human beings and chemical transportation. These include fossil fuel combustion from industrial boilers, internal combustion engines, indoor construction materials like glue, antifreeze admixtures for concrete and paint, fertilizer production, exhaust gas produced from sewage treatment plants and sewage from chemical plants in the river. These atmospheric pollutants included volatile organic compounds (VOCs) (Huang et al., 2017a; Shu et al., 2018; Ji et al., 2017; Cai et al., 2014), nitric oxides (NO_x) (Xu et al., 2017; Trapalis et al., 2016; Y.X. Liu et al., 2017; Papailias et al., 2017), ammonia (NH_3) (Yamazoe et al., 2008; Kolinko and Kozlov, 2009), sulphur dioxide (SO_2) (Wang et al., 2016; Y.X. Liu et al., 2017; Y.X. Liu et al., 2018; Wang et al., 2017), and hydrogen sulphide (H_2S) (Grzeskowiak et al., 2014; Alonso-Tellez et al., 2014; Kataoka et al., 2005; G.Y. Liu et al., 2018). They are regarded as major species causing photochemical smog, acid rain, unpleasant odor, ground-level ozone, fine particulates formation (PM2.5), and even global warming (Wang et al., 2016; Shu et al., 2018; Y.X. Liu et al., 2017; G.Y. Liu et al., 2018). These cause adverse effect or even hazardous to human health, such as respiratory attack, allergies, skin disease, asthma, sick building syndromes (SBS), on-job disease, organs attack, chronic respiratory disease, cardiovascular and nervous system attack, and even cancer induced by VOCs (Huang et al., 2017a; Shu et al., 2018; Cai et al., 2014; Lyu et al., 2017), NO_x (Trapalis et al., 2016; Chaisiwamongkhol et al., 2017; Seifvand and Kowsari, 2015), NH_3 (Kolinko and Kozlov, 2009), and H_2S (Xu et al., 2014). Environmental damage caused by VOCs (Shu et al., 2018; Ji et al., 2017), NO_x (Xu et al., 2017; Trapalis et al., 2016; Y.X. Liu et al., 2017; Papailias et al., 2017), SO_2 (Wang et al., 2016; Y.X. Liu et al., 2017; Y.X. Liu et al., 2018; Wang et al., 2017), and H_2S (Kataoka et al., 2005; G.Y. Liu et al., 2018) included vegetation damage, building facilities corrosion, haze, tropospheric ozone layer destruction, regional acid rain, and photochemical smog. Such problems are a worldwide scale issue (Wang

* Corresponding authors at: School of Environmental Sciences and Engineering, Sun Yat-Sen University, Guangzhou, China.
** Corresponding author.
E-mail addresses: zhangt47@mail.sysu.edu.cn (T. Zhang), ycleung@hku.hk (D.Y.C. Leung), seabao8@gmail.com (H. Huang).

https://doi.org/10.1016/j.envint.2019.01.015
Received 4 December 2018; Received in revised form 6 January 2019; Accepted 6 January 2019
Available online 02 February 2019

et al., 2016; Huang et al., 2017a; Guo et al., 2017; Shu et al., 2018; Seifvand and Kowsari, 2015; Huang et al., 2016; Huang et al., 2013; Huang et al., 2017b). In order to reduce the adverse effect of the air pollutant, appropriate strategy becomes an important key to success.

Traditional air pollutants such as VOCs, NO_x, NH_3, and H_2S are mainly removed via adsorption (Xu et al., 2017; Grzeskowiak et al., 2014; Kataoka et al., 2005; Kim and Ahn, 2012; Ma et al., 2016; G.Y. Liu et al., 2017), catalytic process (Yamazoe et al., 2008; Kataoka et al., 2005; Ma et al., 2016; G.Y. Liu et al., 2017; Tsitonaki et al., 2010; Zhan et al., 2018), and biological treatment (Yamazoe et al., 2008; Grzeskowiak et al., 2014; Kataoka et al., 2005; Ma et al., 2016; G.Y. Liu et al., 2017; Zhan et al., 2018; Zehraoui et al., 2012). Flue gas desulphurization (FGD) is applied for removing SO_2 (Wang et al., 2017). Selective non-catalytic reaction (SNCR) (Xu et al., 2017) or selective catalytic reaction (SCR) (Xu et al., 2017; Yamazoe et al., 2008; Ma et al., 2016; Teramura et al., 2004) are used for removal of NO_x and NH_3. However, some of these methods suffer from certain drawbacks. For example, adsorption is a complicated technique that will cause wastage of material resource; chemical oxidation has selectivity to VOCs and only economically suitable for the removal of VOCs at high concentrations; biological treatment is strongly limited by the temperature, pH, and the growth of microorganisms. Relatively, photocatalytic degradation of VOCs offers many advantages, including the ability to thoroughly and rapidly degrade a wide range of VOCs, even at mild temperature and pressure environment. Recently, a large number of studies on photocatalytic degradation of VOCs have been reported, such as alcohols, ketones, aromatic hydrocarbons and chlorinated hydrocarbons (Zhang et al., 2007; Bianchi et al., 2014; Assadi et al., 2014) Additionally, Bianchi et al. (2014) put forward that micro-sized titania (TiO_2) are very promising materials to be employed in the photocatalytic degradation of VOCs limiting the possible risks for the human health deriving from the use of nanoparticles (NP). Another advantage is that mineralized products (i.e. H_2O, CO_2) produced from VOCs photodegradation are harmless to our environment, even if the VOCs concentration is in the ppb level (Fu et al., 2011). Furthermore, it is a mild oxidation reaction which can be applied in ambient temperature and can use visible-light from solar spectrum to completely mineralize VOCs once the photocatalyst is being modified (Jo and Kim, 2009; Devaraji et al., 2014).

Nanomaterials, defined as particles ranging from 1 to 100 nm diameter, have become widely utilized because of their unique physicochemical properties. Such property became the origin of nano-catalysts. This is especially important to environmental research, such as carbon dioxide reduction for mitigation of greenhouse gas (Dinh et al., 2018; Cometto et al., 2018; Qiao et al., 2017), and energy production via hydrogen generation by water splitting (Zou et al., 2001; Maeda et al., 2006; Debe, 2012; Han et al., 2018; W. Liu et al., 2017; Wang et al., 2018; Zhang and Dai, 2016; Chen et al., 2011; Liu et al., 2015; Helm et al., 2011; Fasciani et al., 2017; Song et al., 2018). Among them, TiO_2 is the most popular and extensively used semiconductor as photocatalyst due to its low cost, high chemical stability, and its non-toxic properties (Wang et al., 2016; Papailias et al., 2017; Chaisiwamongkhol et al., 2017; Shayegan et al., 2018). The photocatalytic process is emerging as a promising alternative technology for the degradation of VOCs. The thin film nano-TiO_2/UV process is an advanced oxidation process and also widely used.

Up to date, most of the photocatalyst are metal-oxide (MO_x) based semiconductors (pure or doped form) in nature. From the schematic diagram of photocatalytic reaction for VOCs removal by semiconductor base photocatalysts as shown in Fig. 1, they have valence band (VB) and conduction band (CB) with a bandgap of 3.2 eV (Shayegan et al., 2018). When a photocatalyst is irradiated with light with energy greater than the bandgap energy, electron (e^-) in the VB will move to CB, leaving a positive hole (h^+) in the VB (Shayegan et al., 2018; Pelizzetti and Minero, 1999; Devipriya and Yesodharan, 2005; Ohtani, 2014). Those excited holes and electrons have strong energy potentials which can migrate to the surface of the semiconductor for generating highly reactive free radicals or recombine (Zhang et al., 2007; Shayegan et al., 2018; Konstantinou and Albanis, 2003). Water (H_2O) and oxygen (O_2) molecules from the gas mixture will be trapped by excited hole in VB and excited electron in CB on the semiconductor surface, respectively. Finally, trapped H_2O will be oxidized into strong oxidizing hydroxyl radicals ($\cdot OH$) at VB, while oxygen will be reduced into active superoxide radical ion ($\cdot O_2^-$) at CB. They can promote the oxidation and eventual completely degrade VOCs into CO_2 and H_2O according to the summarized scheme shown in Fig. 1 (Shayegan et al., 2018).

Development of air pollutant treatment technology was an important focus for air pollutant removal in past decades. However, such technology also suffers from weaknesses like low degradation rate of pollutant at very low concentration (e.g. ppb level of VOCs in indoor air quality (IAQ) control) (Yang et al., 2007), and even lead to catalyst poisoning (e.g. SO_4^{2-} and S poisoning in H_2S degradation) (Alonso-Tellez et al., 2014). In order to overcome limitations of traditional photocatalysis on air pollutant removal, photocatalytic oxidation (PCO) was then developed as it was regarded as an effective pathway for VOCs, SO_2 and H_2S degradation (Shu et al., 2018; Ji et al., 2017; Wang et al., 2017; Grzeskowiak et al., 2014; Alonso-Tellez et al., 2014; Kataoka et al., 2005; G.Y. Liu et al., 2018; Huang et al., 2013; Huang et al., 2017b; Huang et al., 2017c; Fu et al., 2012; Han et al., 2016; Yuan et al., 2012; Li et al., 2012; Zhang et al., 2004; Zhong et al., 2013; Portela et al., 2007; Farhanian and Haghighat, 2014). It has another bright point that it can be operated at room temperature and pressure (Xu et al., 2017; Alonso-Tellez et al., 2014; Yang et al., 2007; Seifvand and Kowsari, 2016). However, traditional PCO also associated with series of problems, such as photocatalyst deactivation, electron-hole (e^-/h^+) pairs recombination, and low reaction efficiency (G.Y. Liu et al., 2018; Huang et al., 2013; Huang et al., 2017b; Huang et al., 2017c; Fu et al., 2012). Other enhancement methods including the use of microwave and magnetic field also associated with another problem of high process cost (Zhang et al., 2004). Relatively, use of strong UV light sources like 185 nm UV or even VUV lamp can enhance the pollutant removal efficiency, removal of residual ozone, and cost reduction simultaneously (Zhang et al., 2004). Most importantly, it was also an effective way of producing active oxidizing species for photocatalytic air pollutant degradation (Zhang et al., 2004). As a result, it became a new direction for photocatalytic air pollutant degradation in recent years.

In this review, the development of the TiO_2 based photocatalyst and its role in air pollutant removal was covered. Several sections are included, where the method of VOCs removal and background of using TiO_2 as VOCs degradation catalyst and its drawback was the first part of the discussion. Secondly, due to the drawback of pure TiO_2, series of modification by chemical doping and use of the nanomaterials support, such as carbon nanomaterials, and nanoporous macrostructure array was the focus of this part. Thirdly, a brief review on their application from bench-top scale to out of the batch reactor scale, problem of catalyst deactivation and solution to them were also discussed together. Fourthly, brief development of alternative metal oxides as TiO_2 replacement was described with serval examples. Finally, the future development of TiO_2 in air pollutants degradation will be forecasted.

2. Titanium dioxide (TiO_2)

Among all semiconductor photocatalysts, TiO_2 is receiving overwhelming concern as a promising photocatalyst due to its superior characteristics, such as nontoxicity, chemical stability, highly photocatalytic activity, ability to be coated as a thin film on a substrate, environmentally friendly (Hoffmann et al., 1995; Wang et al., 2009; Su et al., 2006) etc. TiO_2 exists as three different polymorphs: anatase, rutile and brookite (Nolan et al., 2009; Fischer et al., 2017). The primary source and the most stable form of TiO_2 is rutile, anatase TiO_2 is more active form than rutile TiO_2 in terms of photocatalytic activity

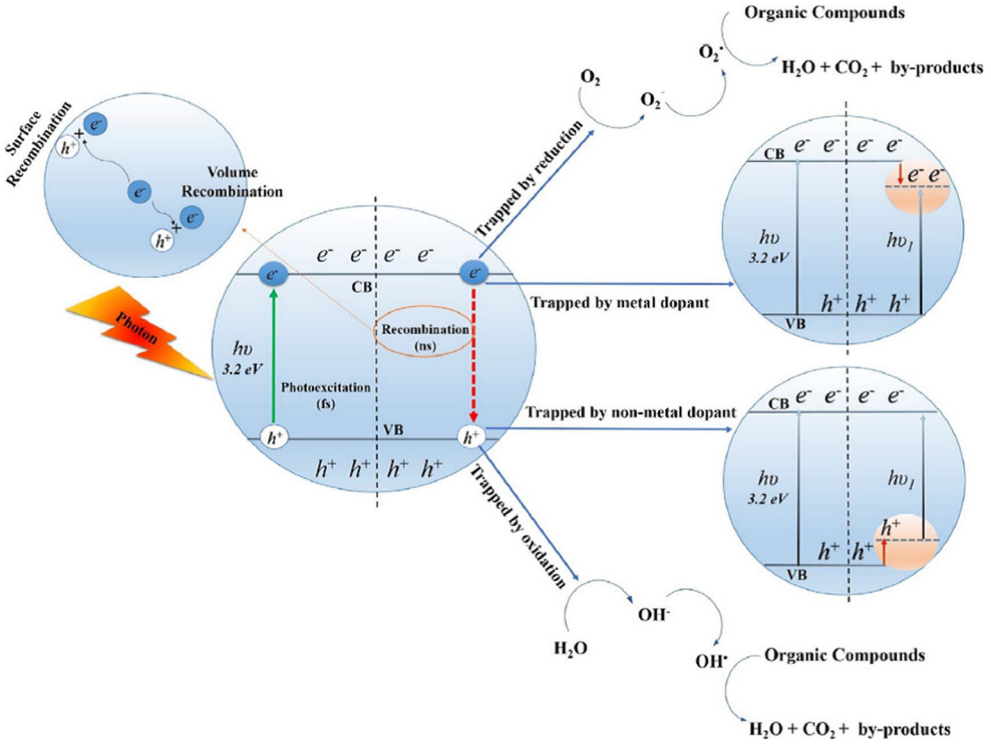

Fig. 1. Basic principle of PCO for removal of VOCs (Shayegan et al., 2018) (Reproduced with permission from Elsevier BV).

(Fischer et al., 2017). Even though anatase have larger bandgap (3.2 eV) than that of rutile TiO_2, anatase TiO_2 has an indirect bandgap, while rutile has direct bandgap (Fischer et al., 2017). Such property result in anatase has stronger photocatalytic activity than that of rutile form due to longer lifetime, which inhibits the e^-/h^+ pairs recombination (Fischer et al., 2017). Brookite is another metastable form among the three TiO_2 phases since it is an intermediate phase in the anatase-to-brookite-to-rutile transformation or brookite-to-anatase-to-rutile transformation (Monai et al., 2017). However, brookite phase is most active among all three TiO_2 phases. Although it has a wider range of bandgap (3.1–3.4 eV) than that of anatase (3.2 eV), due to electron can be trapped in the intermediate depth in this form, which can further increase the lifetime (Fischer et al., 2017; Monai et al., 2017). Other than pure anatase TiO_2 products, there are also some commercial TiO_2 products which contain pure anatase (1077), or a mixture composed of 25:75 rutile and anatase (P25) with a range of bandgap of 3.15–3.21 eV (Stucchi et al., 2018). TiO_2 is the most commonly used photocatalysts with a bandgap of ca. 3.2 eV (see the middle part of Fig. 1) (Shayegan et al., 2018). Since 1972, Fujishima and Honda have discovered that water could be split into hydrogen and oxygen through photoinduction on TiO_2 electrodes (Fujishima and Honda, 1972), numerous experiments on modified TiO_2 were carried out to improve its catalytic performance. Details on the TiO_2 modification will be discussed in the coming sections. However, there are lots of researches focused on modelling and simulation of VOCs removal (Assadi et al., 2014; Cloteaux et al., 2014), because researchers realized that relevant mathematical models are required for industrial applications.

Mesoporous TiO_2 with macroporous structure is of considerable interest as potential catalytic support or photocatalytic material. This is because the macroporous channels could serve as light-transfer paths for the distribution of photon energy onto the large surface of inner photoactive mesoporous frameworks. As a result, the light utilization efficiency of heterogeneous photocatalytic systems, such as photo-oxidation reactors or solar cells, could be enhanced. In addition, the hierarchical structure-in-structure arrangement of mesopore and macropore is important in molecule traffic control and in the resistance of the photocatalyst to poisoning by inert deposits (Rolison, 2003). Such structure not only provides a readily accessible pore-wall system but also optimizes the transport of matter by minimizing the pressure drop over the monolithic material. Microporous TiO_2 also drew particular interest since the mix up of the bandgap between microporous TiO_2 grown on anatase TiO_2 in the resulting hybrid structure (micropore-anatase TiO_2 composite (MA)) enhanced the electron/hole (e^-/h^+) separation at the interface of macroporous TiO_2 and anatase in MA, as illustrated in Fig. 2 (Lyu et al., 2017).

Besides the mesoporous TiO_2, TiO_2 nanoparticles (NP) were another popular materials since this group of materials has higher flexibility in the application, such as dispersing on the glass for TiO_2 film preparation (Falk et al., 2018; Kim et al., 2017). In addition, its bandgap can also be tuned to around 2.9–2.95 eV from 3.17 to 3.2 eV upon microwave treatment throughout the TiO_2 NP synthesis (Falk et al., 2018), or

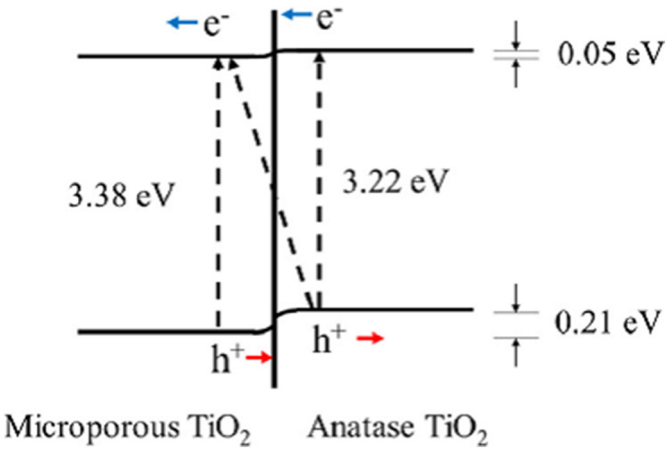

Fig. 2. Primary photoprocess at the interface of microporous TiO_2 and anatase TiO_2 (dotted arrow: band to band leaps of electrons; solid arrows: transfer directions of photogenerated charge carriers at the interface region) (Lyu et al., 2017) (Reproduced with permission from Elsevier BV).

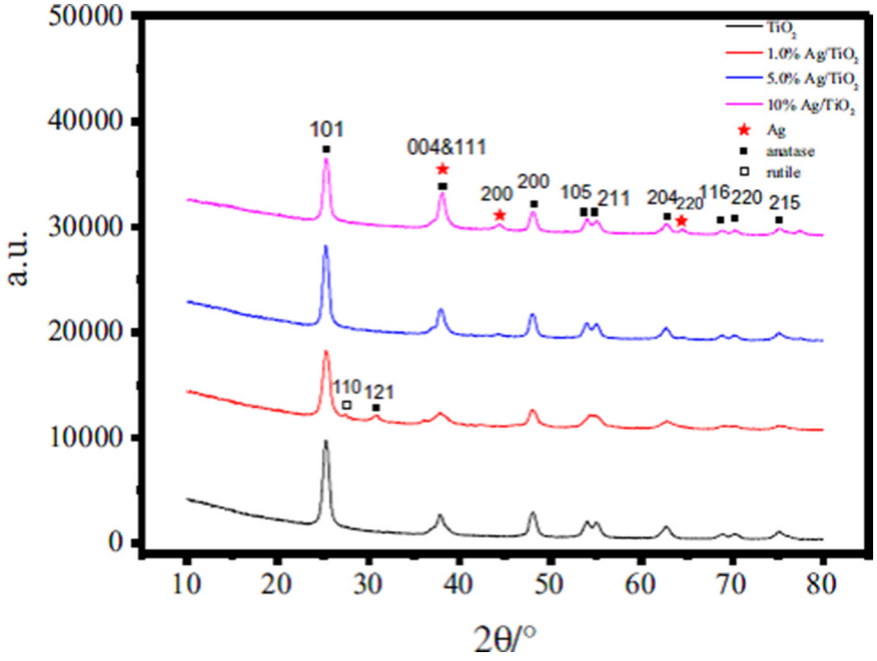

Fig. 3. XRD patterns of TiO_2 and various Ag/TiO_2 composites (Xu et al., 2017) (Reproduced with permission from Elsevier BV).

different thermal treatment method achieved by furnace and flame (Kim et al., 2017). Some of the TiO_2 films were fabricated on glass surface by sol-gel synthesized from direct mixing of the Ti sources with thickening agents like polyvinyl pyrrolidone K30 (PVP-K30) with calcination at high temperature (Xie et al., 2016). It exhibited strong UV capturing ability with the evidence of high visible-light transmittance as claimed by Xie's group (Xie et al., 2016). Micro-sized TiO_2 such as commercial available pigmentary TiO_2 was also attracted by some research groups, which exhibited comparable light absorption properties (3.15–3.28 eV) to the P25 products (3.21 eV) (Bianchi et al., 2015).

3. Enhancement of photocatalytic activity by chemically modified TiO_2

TiO_2 is an efficient photocatalyst, however, one severe disadvantage of this pure semiconductor material is the large bandgap (i.e. 3.2 eV) for bulk TiO_2, which limits its photosensitivity to the UV region. Various methods have been applied to extend the light response to visible-light (400–800 nm) for photocatalytic activity improvement.

The most common approach of enhancement of TiO_2 is the development of TiO_2 nanoparticles (< 10 nm) for boosting the photocatalytic activity. Various approaches have been developed, which include doping the TiO_2 with metals (e.g., V, Cr, Mn, Fe, Co, Ni, Cu, and W) and non-metals elements doping (e.g. carbon, nitrogen, fluorine, phosphorus, and sulphur); doping with semiconductor (e.g. WO_3, MnO_2 and ZnO); and the use of nanomaterial as TiO_2 support.

3.1. Metals doped TiO_2

Doping TiO_2 with metal ions was considered a good tool to improve photocatalytic properties. It was because effective charge separation by narrowing down the TiO_2 bandgap could be achieved, resulting in an enhanced response to the visible-light region. In other words, the recombination of e^-/h^+ pair can be prevented throughout the light irradiation. Generally, normal metals and transitional metals (d and f-block elements) were the commonly used dopants, which included Al, Cu, Cr, Fe, Pt, Pd, Rh, Mo, Mn, Mg, Y, Ga, Zr, Zn, Nb, Sb, Au, Ag, V, Ni, Co, Ce, Ti and so on (Shu et al., 2018; Xu et al., 2017; Kolinko and Kozlov, 2009; Wang et al., 2017; G.Y. Liu et al., 2018; Huang et al., 2013; Huang et al., 2017b; Fu et al., 2012; Seifvand and Kowsari, 2016; Ghosh and Maruska, 1977; Zhang et al., 1998; Anpo and Takeuchi, 2003; Stucchi et al., 2016; Ravikumar et al., 2018; Feng et al., 2018; Shakir et al., 2018; Luo et al., 2018; Moradi et al., 2018; Bhachu et al., 2017; Nethi et al., 2017; Singh et al., 2017; Erjavec et al., 2017; Rodriguez et al., 2017; Tan et al., 2017; Yang et al., 2015; Yan et al., 2017; Song et al., 2012). The metal-doped TiO_2 (M-doped TiO_2) composites were synthesized by chemical reactions, including hydrothermal reaction (Xu et al., 2017; Ravikumar et al., 2018; Tan et al., 2017), chemical reduction (Kolinko and Kozlov, 2009), high temperature with inert gas environment (Feng et al., 2018), thin film synthesis (Shakir et al., 2018), direct mixing with heating (Shu et al., 2018; G.Y. Liu et al., 2018; Luo et al., 2018; Rodriguez et al., 2017; Song et al., 2012), direct mixing with calcination (Kolinko and Kozlov, 2009; Huang et al., 2013; Huang et al., 2017b; Moradi et al., 2018; Nethi et al., 2017; Singh et al., 2017), chemical vapor deposition (CVD) (Bhachu et al., 2017; Yan et al., 2017), sol-gel (Seifvand and Kowsari, 2016; Yang et al., 2015), photo-deposition (Rodriguez et al., 2017), and photoreduction with stirring (Kolinko and Kozlov, 2009; Erjavec et al., 2017). Some of M-doped TiO_2 was synthesized by ultrasonic mixing between TiO_2 and metal precursor (Stucchi et al., 2016), electrostatic self-assembly (Fu et al., 2012), or electrospinning (Wang et al., 2017). Even though M-doped TiO_2 was obtained from reaction between metal salt ion and TiO_2 from different precursors, not all of them existed in the form of pure metallic metal nanoparticles in the final M-doped TiO_2 products. Examples of the pure metal nanoparticles deposited TiO_2 in the M-doped TiO_2 include Pt-TiO_2, Au-TiO_2, Fe-TiO_2, Zr-TiO_2, Pd/IL-TiO_2, Ag/TiO_2, and CeTN (Xu et al., 2017; Wang et al., 2017; Fu et al., 2012; Seifvand and Kowsari, 2016; Moradi et al., 2018; Singh et al., 2017), all of which form clear signal pattern of metallic dopant in XRD spectrum of products. Ag/TiO_2 synthesized by Xu's group was chosen as representative with XRD pattern shown in Fig. 3 (Xu et al., 2017). After TiO_2 doped with monometallic dopant, their visible-light absorption activity was enhanced. This is reflected by the red shifting of the bandgap (2.67–3.33 eV) or the absorption edge (326–1100 nm) in the M-doped TiO_2 as compared with those of pure TiO_2 (bandgap: 3.05–3.45 eV, absorption edge: 300–412.9 nm) (Xu et al., 2017; Seifvand and Kowsari, 2016; Stucchi et al., 2016; Ravikumar et al., 2018; Feng et al., 2018; Shakir et al., 2018; Luo et al., 2018; Moradi et al., 2018; Bhachu et al.,

2017; Nethi et al., 2017; Singh et al., 2017; Erjavec et al., 2017; Rodriguez et al., 2017; Tan et al., 2017; Yang et al., 2015; Yan et al., 2017). The enhancement was orientated from the introduction of intra conduction band to TiO_2 (Seifvand and Kowsari, 2016; Stucchi et al., 2016; Ravikumar et al., 2018; Feng et al., 2018; Shakir et al., 2018; Moradi et al., 2018; Bhachu et al., 2017; Erjavec et al., 2017; Tan et al., 2017; Yang et al., 2015; Yan et al., 2017), surface plasmon resonance of doped metal (Xu et al., 2017; Rodriguez et al., 2017), or change in the nanostructure (Luo et al., 2018; Nethi et al., 2017; Singh et al., 2017) upon doping of the dopant with TiO_2 throughout the doping reaction. Monometallic doping of TiO_2 was also achieved on the nonmetal elements doped TiO_2, Pt/N-TiO_2 synthesized by sol-gel method between Pt ions/N-precursor solution and Ti-precursor solution was an example (Sun et al., 2011). The product showed strong visible-light absorption (Bandgap: 2.69 eV, absorption band: 495 nm) when compared to corresponding pure TiO_2 (Bandgap: 3.10 eV, absorption band: 400 nm) (Sun et al., 2011). Such properties resulted in the strong visible-light photocatalytic activity in the gas phase indoor VOCs degradation compared to pure TiO_2 (P25) (Sun et al., 2011).

Early in 1977, Ghosh and Maruska (1977) found that aluminum doping increased the minority carrier diffusion length, which was indicated from the increase in the quantum efficiency up to 80% after the semiconductor electrode doped with Al. They also reported that chromium doping allowed generation of hydrogen and oxygen using visible-light, with sunlight conversion efficiency raised from 0.4% to 1.3% (Ghosh and Maruska, 1977). Such results indicated the enhancement of the TiO_2 doping by metal.

Many transitional metal ion dopants have been previously investigated for TiO_2 system, among which Fe^{3+} was widely examined. Although it has been known that the effect of Fe^{3+} doping depends on the dopant concentration, the particle size of the TiO_2 catalyst is not strongly dependent on dopant concentration (Zhang et al., 1998). However, its photonic efficiency was strongly dependent on the Fe^{3+} dopant concentration. It reflected from the maximum photonic efficiency of 4.8% (Fe-doped TiO_2 with 0.2 at% Fe^{3+} and TiO_2 with particles of 6 nm) and 4.9% (Fe-doped TiO_2 with 0.05 at% Fe^{3+} and TiO_2 with particles of 11 nm) in the CH_3Cl photodecomposition catalyzed by these Fe-doped TiO_2, respectively (Zhang et al., 1998).

The photocatalytic reactivity of semiconducting TiO_2 is remarkably enhanced by the addition of small amounts of noble metals such as Pt or Rh; this is explained by the quick transfer of photogenerated electrons in TiO_2 semiconductors to the loaded metal particles, resulting in a decrease in e^-/h^+ pair recombination, as well as efficient charge separation (Anpo and Takeuchi, 2003).

Anpo and Takeuchi (2003) discovered that a large shift in the absorption band of the TiO_2 catalysts towards the visible-light region could be possibly made when metal-ion was implanted with various transition-metal ions such as V, Cr, Mn, Fe, and Ni. As can be seen in Fig. 4, the absorption band of the Cr-ion-implanted TiO_2 was shifted towards the visible-light region. However, Cr-, Mg-, or Ti-ion-implanted TiO_2 exhibited no shift in the absorption spectra, hence they concluded that the shift is caused by some interaction between the transition metal ions and the TiO_2 catalyst.

Besides single metal-doped TiO_2, bimetallic dopants doped TiO_2 was also developed recently, such as Er-W codoped TiO_2 (Kubacka et al., 2018), and Bi-W codoped TiO_2 (Ratova et al., 2017). Bimetallic species doped TiO_2 was found to possess strong visible-light absorption ability when compared to the monometallic species doped TiO_2. The codoping of TiO_2 was mainly achieved by either magneton sputtering of Bi and W based species towards TiO_2 target (Ratova et al., 2017), or direct chemical reaction between dopants (Er and W) and titanium based compounds (Kubacka et al., 2018). All the resulting materials showed strong visible-light absorption when compared to the bare TiO_2 (Kubacka et al., 2018; Ratova et al., 2017). Er-W codoped TiO_2 (ErWTi) synthesized by Kubacka's group even showed absorption at the near-IR range (800–1000 nm) (Kubacka et al., 2018).

3.2. Metal oxide doped TiO_2

Unfortunately, since deposited metal particles only serve as electron trapping agent, they are not effective to enhance the adsorption of the pollutants. Other kinds of TiO_2 coupled with semiconductors have been reported to perform both the above mentioned functions. Alternative doping method was then developed to achieve the TiO_2 bandgap reduction. While WO_3, MnO_2, FeO_x, YO_x, VO_x, NiO, and ZnO were widely used metal oxides dopants (Alonso-Tellez et al., 2014; Kwon et al., 2000; Gholami et al., 2014; Kaky et al., 2017; Hunge et al., 2018; Zhang et al., 2017; Zdravkov et al., 2018; Mazabuel-Collazos and Rodriguez-Paez, 2018; J. Liu et al., 2018). In general practice, this group of modified TiO_2 materials was obtained from heating in furnaces (Kaky et al., 2017), spray pyrolysis (Hunge et al., 2018), hydrothermal reaction (Zhang et al., 2017; J. Liu et al., 2018), and impregnating between TiO_2 and dopant precursor (Alonso-Tellez et al., 2014). At the same time, some of the metal oxide-doped TiO_2 (MO_x-TiO_2) were obtained from the reaction between metal ion salt and TiO_2 based precursors, such as Cu-TiO_2 and CuTN, WO_3/TiO_2, PdO-TiO_2, Mn/TiO_2, PtO/TiO_2, Fe_2O_3/TiO_2, V_2O_5/TiO_2, NiO/TiO_2, MoO_3/TiO_2, ZnO-TiO_2 and CoO/TiO_2 (Shu et al., 2018; Kolinko and Kozlov, 2009; Wang et al., 2017; G.Y. Liu et al., 2018; Huang et al., 2017b; Fu et al., 2012; Stucchi et al., 2016; Song et al., 2012; Hunge et al., 2018; Mazabuel-Collazos and Rodriguez-Paez, 2018; J. Liu et al., 2018). This is reflected from the clear appearance of MO_x in XRD pattern in the MO_x-TiO_2 products (Fu et al., 2012; Stucchi et al., 2016; Hunge et al., 2018; J. Liu et al., 2018). Copper doped TiO_2 (K_75) synthesized by Stucchi's team was chosen as representative, where the CuO and Cu_2O can be observed clearly from the XRD patterns in Fig. 5 (Stucchi et al., 2016). XPS may help in proving their existence if XRD cannot identify them (Shu et al., 2018; Wang et al., 2017; G.Y. Liu et al., 2018; Huang et al., 2017b; Song et al., 2012). Evidence includes (i) the shifting of the metal ion (M^{n+}) peak from the standard position, and (ii) presence of MO_x signal (i.e. HR-XPS peak) in the resulting MO_x-TiO_2 samples (Shu et al., 2018; Wang et al., 2017; G.Y. Liu et al., 2018; Song et al., 2012).

Generally, bandgap and absorption edge of the MO_x-TiO_2 hybrids were red shifted to 2.75–3.05 eV or double edge at 389 and 475 nm from 3.10 eV or 389 nm in the corresponding pure TiO_2 (Kaky et al., 2017; Hunge et al., 2018; Zhang et al., 2017; J. Liu et al., 2018). This is obvious evidence for the enhancement of the absorption at visible-light region.

This has been realized by coupling the WO_3 semiconductor with TiO_2. As a basic function, WO_3 has a suitable conduction band potential to allow the transfer of photogenerated electrons from TiO_2 facilitating effective charge separation. Additionally, formation of a monolayer of WO_x species on TiO_2 can significantly increase the surface acidity, as WO_3 is 15 times more acidic than TiO_2 (Kwon et al., 2000). Because of this increased acidity, WO_3/TiO_2 can adsorb more hydroxyl groups and simultaneously more organic reactants on its surface. Thus, significant improvement of the photocatalytic activity (PCA) has been achieved in comparison to the standard commercial photocatalysts. Besides using WO_3, other metal oxides like ZnO was also tried in the hybrid metal oxide doping (Gholami et al., 2014; Mazabuel-Collazos and Rodriguez-Paez, 2018). ZnO-TiO_2 synthesized by Mazabuel-Collazos and Rodriguez-Paez (2018) showed that the visible-light absorption in the range of 400–425 nm was strengthened upon the increase in the amount of Ti^{4+} precursor added to ZnO throughout the synthesis at 500 °C post-treatment. Such properties were important for the enhancement in the visible-light absorption.

Besides the traditional metal oxides for TiO_2 doping, use of multi-metallic oxides composed of d-block and f-block metal like $InVO_4$ and $LaVO_4$ were also popular targets for the modification of TiO_2 for bandgap reduction (Xiao et al., 2008; H.J. Huang et al., 2009). Visible-light sensitive materials like $InVO_4$/TiO_2 and $LaVO_4$ were synthesized by the sol-gel method after mixing TiO_2 with $InVO_4$ sol or $LaVO_4$ sol, followed by hydrothermal reaction for the merging of two oxides (Xiao

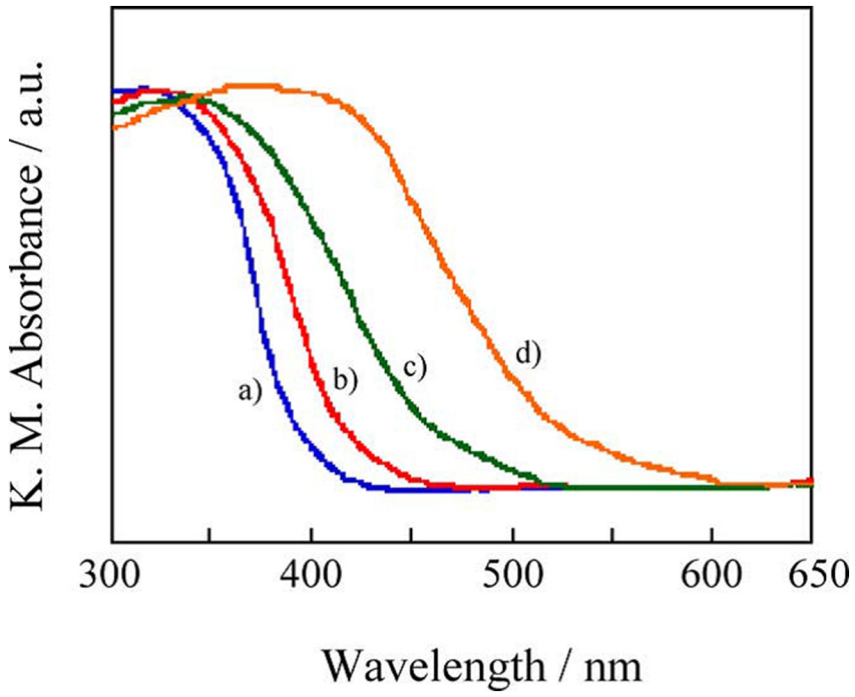

Fig. 4. The UV–vis absorption spectra of TiO_2 (a) and Cr ion-implanted TiO_2 photocatalysts (b–d). The amount of implanted Cr ions (μmol/g); (a) 0, (b) 0.22, (c) 0.66, (d) 1.3 (Anpo and Takeuchi, 2003) (Reproduced with permission from Elsevier BV).

et al., 2008; H.J. Huang et al., 2009). The resulting materials showed an obvious red shift in the absorption peak onset wavelength from 400 nm in pure TiO_2 to 540 nm after hybridization of TiO_2 with $InVO_4$, which is reflected from the ultraviolet photoelectron spectra (UPS) spectrum of $InVO_4/TiO_2$ illustrated in Fig. 6 as representative (Xiao et al., 2008). Since the $InVO_4$ have a bandgap of 2.1 eV based on Xiao's group hypothesis, the shifting of the bandgap in the $InVO_4/TiO_2$ product was contributed from the modification of $InVO_4$. This means the bandgap was reduced that allowed the absorption of visible-light for photon generation (Xiao et al., 2008). Similar observation was recorded in the $LaVO_4/TiO_2$ with the appearance of a clear peak at the visible-light region (> 400 nm) when compared to the pure TiO_2 like P25, T400, and T500. Its bandgap was also shifted to the value of 2.1 eV, which showed the evidence of successful chemical doping between $LaVO_4$ and TiO_2 after hydrothermal reaction (H.J. Huang et al., 2009). Extra characterization carried out by H.J. Huang et al. (2009) by means of photoluminescence (PL) showed that no PL peak was observed in $LaVO_4/TiO_2$ composite at 450 nm–700 nm region, while it observed in the case of pure $LaVO_4$. This showed that the origin of the strong visible-light absorption was the inhabitation of the e^-/h^+ pair recombination due to the presence of the $LaVO_4$ which acted as the heterojunction of $LaVO_4/TiO_2$ that benefited the visible-light

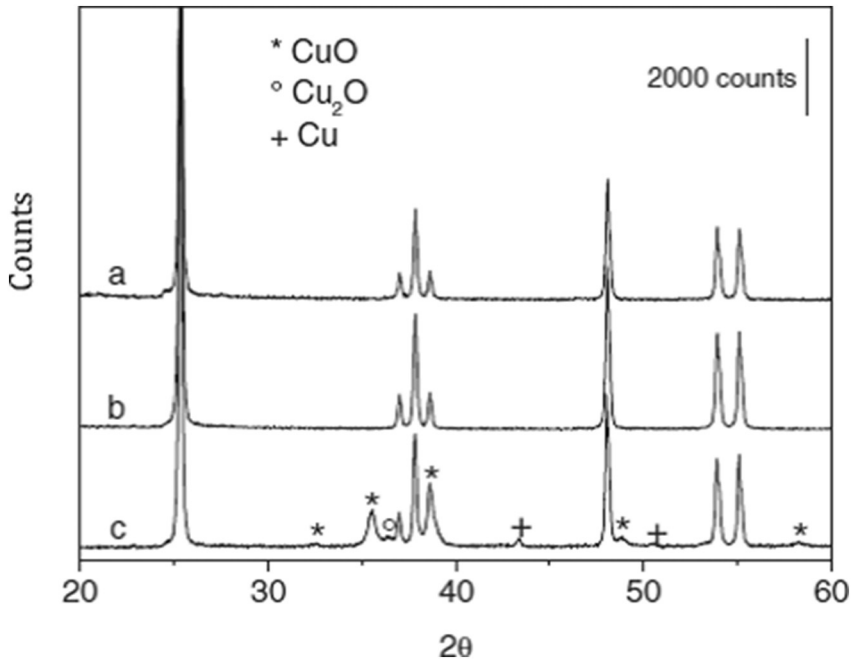

Fig. 5. XRD patterns of Kronos 1077 TiO_2 (curve a), K_40 (curve b) and K_75 (curve c) samples (Stucchi et al., 2016) (Reproduced with permission from Elsevier BV).

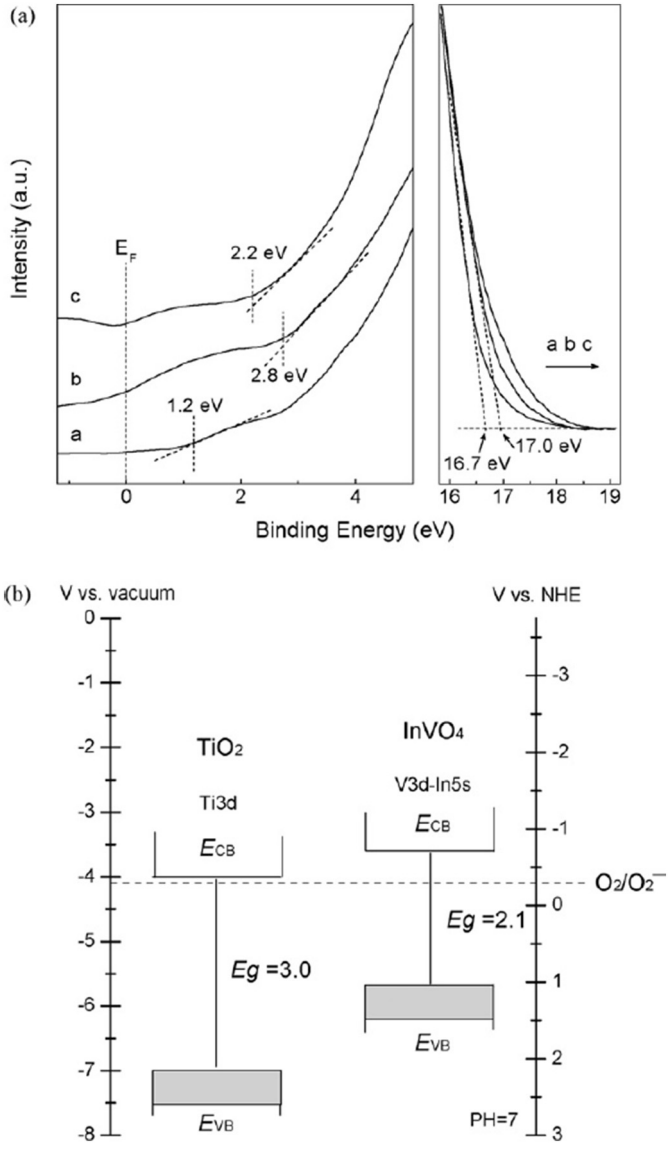

Fig. 6. (a) Ultraviolet photoelectron spectra (UPS) of $InVO_4$ (a), TiO_2 (b) and $InVO_4/TiO_2$ (c). (b) Position of the ECB and EVB for TiO_2 and $InVO_4$ on the absolute vacuum energy scale and with respect to normal hydrogen electrode (NHE). The relationship between the absolute vacuum energy (E_{abs}) and the normal electrode potential (E°) is expressed as follows: $E_{abs} = -E^{\circ} - 4.44$ (at 298 K). $E^{\circ}(O_2/O_2^{\cdot -})$ of -0.33 V is taken as a reference (Xiao et al., 2008) (Reproduced with permission from Elsevier BV).

absorption (H.J. Huang et al., 2009).

3.3. Nonmetal elements doped TiO_2

Although metal doping showed advantages in lowering the bandgap and enhancing visible-light absorption, several drawbacks exist such as thermal instability of doped TiO_2, electron trapping by metal centres, and requirement of more expensive ion-implantation facilities (Wang et al., 1999; Yamashita et al., 1998). As a result, alternative doping methods avoiding the use of metal based dopant was then proposed.

Doping titania based materials with anions, such as N^{3-}, C^{4-}, S^{4-} (Belver et al., 2006) or halides (F^-, I^-) (C.L. Yu et al., 2009; Yu et al., 2003; J.G. Yu et al., 2009; Yu et al., 2002; Liu et al., 2006), mix with N-precursor (ammonia solution (Tryba et al., 2018) or amine (Kannangara et al., 2018)) via sol-gel method are regarded as another approach to producing visible-light activated TiO_2 photocatalysts. The investigation carried out by Tryba's group suggested that these species substitute the oxygen lattice on TiO_2 and lead to a bandgap narrowing via the formation of mid-gap inside the bandgap of TiO_2, which resulted in double bandgap respectively at UV range (3.18–3.34 eV) and at visible-light range (400–520 nm) with bandgap (1.57–2.25 eV) (Tryba et al., 2018). Interestingly, the calcination temperature of the N-doped TiO_2 obtained also affected their bandgaps, and hence the visible-light absorption ability strongly. Maximum visible-light absorption ability was recorded at a calcination temperature of 200 °C which covered the full range of visible-light by its low bandgap of 1.57 eV. However, increase in calcination temperature (> 300 °C) reduced the visible-light sensitive bandgap, and disappeared finally when the temperature further increased to 500 °C, i.e. only UV sensitive bandgap (Tryba et al., 2018).

The substitutional doping of N is the most effective because its *p* states contribute to the bandgap narrowing by mixing with O 2*p* states. Although doping with S shows a similar bandgap narrowing, it would be difficult to incorporate it into the TiO_2 crystal because of its large ionic radius, as evidenced by a much larger formation energy required for the substitution of S than that required for the substitution of N. The states introduced by C and P are too deep in the gap (Asahi et al., 2001).

Other than nitrogen doping to TiO_2, doping with other elements like carbon (Luna-Flores et al., 2017; Islam et al., 2017) and silicon (Gaidau et al., 2017) were alternatives. Similar to some of the metal-doped TiO_2, nonmetallic element doped TiO_2 was synthesized by hydrothermal reaction under high temperature (200 °C) after mixing Ti based salt with silicon dioxide together (Gaidau et al., 2017), and direct mixing of Ti salt with carbon source like 1-decanol under heating (Luna-Flores et al., 2017). The resulting Si-doped TiO_2 products (TiO_2-10SiO_2 NP and TiO_2-20SiO_2 NP) showed enhancement in the absorption at visible-light wavelength range when the SiO_2 doping level was 10% when compared to pure TiO_2 based on investigation from Gaidau's group, which may be contributed from the reduced e^-/h^+ pair recombination rate with the presence of photoadsorption of O_2 and self-cleaning in the materials (Gaidau et al., 2017). Such properties were beneficial to the UV–vis light assisted self-cleaning ability (Gaidau et al., 2017). In contrast, the recorded bandgap of carbon doped TiO_2 (CD-aTiO_2: 3.37–3.41 eV) was similar to that of corresponding pure TiO_2 (DP25: 3.10 eV) as claimed by Luna's group (Luna-Flores et al., 2017). Possible reason for such phenomenon may be due to the change of the surface morphology of CD-aTiO_2 after the carbon doping of DP25 (Luna-Flores et al., 2017).

Halogen doped TiO_2 was also the interest of study recently, which included fluorine (F) (C.L. Yu et al., 2009; Yu et al., 2003; J.G. Yu et al., 2009; Yu et al., 2002), chlorine (Cl) (Sun et al., 2010), and iodine (I) (Liu et al., 2006) doped TiO_2. After the TiO_2 doped with fluorine, chlorine or iodine, its light absorption properties were red shifted when compared to pure TiO_2 (Yu et al., 2002; Liu et al., 2006; Sun et al., 2010). It was indicated by the (i) recorded bandgap of 2.90 eV (fluorine-doped TiO_2 (F-doped TiO_2)) (Yu et al., 2002) and ~3.00 eV (chlorine-doped TiO_2 (Cl-TiO_2)) (Sun et al., 2010), (ii) slightly reduced transmittance at 400–600 nm (F-doped TiO_2) (Yu et al., 2003), or (iii) strengthened absorption at visible-light range (420–550 nm) for F-doped (J.G. Yu et al., 2009) and I-doped mesoporous TiO_2 (MTI) (Liu et al., 2006). Such properties were indicative to the improvement of the visible-light driven photocatalytic reactions or visible-light driven PCOs reactions.

Besides single dopant doped TiO_2, sometimes two elements codoped TiO_2 samples were also the targets of study, one of the examples was C-N codoped TiO_2 (Zhang et al., 2018; Janus et al., 2015). It was achieved by direct reaction between TiO_2 powder with gaseous ammonia and n-hexane vapor under an inert gas flow environment and high temperature at a closed tube furnace system (Janus et al., 2015), or direct reaction between amino group containing TiO_2, and carbon nano molecular sieves via hydrothermal reaction (Zhang et al., 2018). The resulting C, N-codoped TiO_2 showed strong visible-light absorption properties according to the significant red shifting of the bandgap from 3.04 eV of pure P25 to 2.76 eV of the C, N-codoped TiO_2 product. At the

same time, the degree of shifting was also increased upon increase in the argon treatment temperature for the as-prepared CN-codoped TiO_2 from 700 °C (CN-T700) to 1100 °C (CN-T1100) under a constant amount of N-containing titanium source and carbon source of toluene (Zhang et al., 2018). Another example was metal-nonmetal codoping to TiO_2. It was found that N-Fe co-doped TiO_2 had much higher photocatalytic activity than pure TiO_2, N-doped TiO_2 and Fe-doped TiO_2 in the visible-light region due to the creation of surface oxygen vacancies. Cong et al. (Cong et al., 2007) reported that titania co-doped with nitrogen and iron (0.5 wt%) decomposed a 50 mL Rhodamine B (RB) (20 mg L^{-1}) solution completely within 4 h under visible-light irradiation, faster than that of N-doped TiO_2 or Fe-doped TiO_2. However, under UV light, the photocatalytic activities of Fe-N co-doped TiO_2 was lower than that of undoped TiO_2. The nitrogen ions and Fe^{3+} dopants could act as a recombination centre of electrons and holes, thus decreasing the UV photoactivity (Cong et al., 2007). As a result, the correct selection of the dopant for TiO_2 doping became important.

3.4. TiO_2 supported on secondary substrates

Besides the traditional doping methods for the modification of TiO_2 based photocatalyst, use of nanomaterials as support is another approach. Among them, carbon based one, including carbon nanotube (CNT), graphitic carbon nitrile (g-C_3N_4), carbon fiber, and graphene is most popular used since large electron-storage capacity can improve the surface area and charge separation of the metal oxides based photocatalysts (Ma et al., 2016; Tian et al., 2017; Andryushina and Stroyuk, 2014).

In TiO_2 loaded CNT group, the loading of TiO_2 with CNT promotes the electron transfer and prevents the electron/hole (e^-/h^+) pair recombination (Natarajan et al., 2017; Petronella et al., 2015; Leary and Westwood, 2011; Woan et al., 2009; Gui et al., 2014; Karousis et al., 2010). In the case of 2D graphene supported P25 based materials, most studies showed that P25 loaded 2D graphene exhibited strong absorption in the visible-light region once the P25 or chemically modified TiO_2 loaded into graphene nanosheet array, bandgap reduction increased upon increase in GO added in the raw solution (Trapalis et al., 2016; Andryushina and Stroyuk, 2014; Morales-Torres et al., 2013; Li et al., 2013; Jing et al., 2014; Haldorai et al., 2014; Roso et al., 2017; Ebrahimi and Fatemi, 2017; Zhang et al., 2013; Wang et al., 2012; Jo and Kang, 2013; Roso et al., 2015; Neppolian et al., 2015; Yang et al., 2017; Bhirud et al., 2015). Example from Morales-Torres's group showed that the bandgap of P25 loaded graphene was shifted to a lower value when the amount of GO increased from 1 wt% to 6 wt% as shown in Fig. 7 (Morales-Torres et al., 2013). However, the enhancement will be reduced when the TiO_2/GO ratio was larger than the optimum value (Trapalis et al., 2016; Seifvand and Kowsari, 2015; Zhang et al., 2013; Jo and Kang, 2013; Yang et al., 2017). In recent years, 3D graphene aerogel becomes a new star due to its mesoporous structure with bulk block size (foam sheet or bulk pillet block), which lead to the widening of the application as photocatalyst (Chen et al., 2018; Hou et al., 2012; Nawaz et al., 2017; Li et al., 2016). Same as TiO_2 based 2D graphene, the TiO_2 can also be assembled into the 3D graphene aerogel array during the stacking of the graphene oxide nanosheets via chemical reduction under hydrothermal environment. The absorption peak of the product was also widened in the visible-light region when compared to the pure TiO_2 or P25 (< 400 nm). It was proved from the UV–visible diffuse reflection spectra (DRS) spectrum Kubelka-Munk function plotted against the photon energy as illustrated in Fig. 8 from 3D TiO_2/GR composite synthesized by Li's group as representative. Bandgap variation was clearly observed with TiO_2 loading (Li et al., 2016).

Other than CNT and graphene used as TiO_2 support, carbon fibers (Tian et al., 2017; M. Li et al., 2017), and graphitic carbon nitrile (g-C_3N_4) (Papailias et al., 2017; Ma et al., 2016; Chang et al., 2014; Li et al., 2015; Y.H. Li et al., 2017; Song et al., 2016; Reli et al., 2016; Koci et al., 2017; Yu et al., 2013; Munoz-Batista et al., 2014) are also extensively used TiO_2 support for photocatalyst preparation. In the group of carbon fibers as support, activated carbon fibers (ACF) were the major component. TiO_2/carbon fibers based materials were mainly synthesized by direct mixing of commercial activated carbon fiber flets (ACFF) with tert-butyl titanate (TBT) for the formation of TiO_2/ACFF precursor as the first step. The final TiO_2/ACFF product was then obtained by hydrothermal reaction in a sealed system (Tian et al., 2017; M. Li et al., 2017). While TiO_2/g-C_3N_4 were synthesized by reaction between carbon source like melamine with Ti foil (Li et al., 2015) or P25 (Papailias et al., 2017; Ma et al., 2016; Y.H. Li et al., 2017), reaction between urea and P25 (Yu et al., 2013), or direct reaction between TBT and g-C_3N_4 (Chang et al., 2014), or mixing TiO_2 directly with g-C_3N_4 (Song et al., 2016; Reli et al., 2016; Koci et al., 2017; Munoz-Batista et al., 2014). Most of them were synthesized by a simple treatment under heating (60–100 °C) after the reaction or mechanical mixing in common practice (Papailias et al., 2017; Ma et al., 2016; Chang et al., 2014; Y.H. Li et al., 2017; Song et al., 2016; Reli et al., 2016; Koci et al., 2017; Yu et al., 2013; Munoz-Batista et al., 2014), while some were obtained via hydrothermal reaction (Li et al., 2015). The resulting TiO_2/ACFF or TiNF/ACFF showed strong visible-light absorption at 306–334 nm and red shifted bandgap (2.95–2.99 eV) when compared to that of pure ACF (no bandgap and absorption improvement) and pure TiO_2 based structures (absorption peak: 299–302 nm, bandgap = 3.17–3.22 eV) (Tian et al., 2017; M. Li et al., 2017). Similar phenomenon was also observed in the g-C_3N_4 as supporting material, which was reflected by the shifting of the absorption to 400–550 nm and bandgap lowered to 2.48–3.16 eV when compared to pure TiO_2 (384–418 nm, bandgap: 3.02–3.26) (Papailias et al., 2017; Ma et al., 2016; Chang et al., 2014; Li et al., 2015; Y.H. Li et al., 2017; Song et al., 2016; Reli et al., 2016; Koci et al., 2017; Yu et al., 2013; Munoz-Batista et al., 2014). Such phenomena were proposed to be the synergistic effect between ACF or g-C_3N_4 and TiO_2 due to the mixing of lattice between ACF or g-C_3N_4 and TiO_2, which inhibited the e^-/h^+ pair recombination, and enhanced the charge transfer (Papailias et al., 2017; Ma et al., 2016; Tian et al., 2017; M. Li et al., 2017; Chang et al., 2014; Li et al., 2015; Y.H. Li et al., 2017; Song et al., 2016; Reli et al., 2016; Koci et al., 2017; Yu et al., 2013; Munoz-Batista et al., 2014).

Besides carbon nanomaterials as support, nanoporous macrostructures were also used as supporting materials for improving photochemical properties of pure TiO_2. For example, TiO_2-aluminum silicate (TAS) fiber synthesized by Yuan's group showed that once tetrabutyl titanate (TEOT) mixed with TAS fiber followed by calcination, absorption peaks appeared at the region of 300–400 nm (zero absorption for pure TAS fiber) (Yuan et al., 2012). The maximum absorption intensity was recorded when the calcination temperature for TAS formation was 500 °C, but the intensity was reduced when the calcination temperature was out of the optimum temperature (Yuan et al., 2012). Similar tendency was observed in the variation of BET specific area and pore size volume properties of TAS calcinated from 300 to 700 °C (Yuan et al., 2012). Such properties played an important role in the simultaneous removal of NO_x, SO_2, and Hg^{2+} in the simulated flue gas (Yuan et al., 2012). Another two examples involve the use of molecular sieve like zeolite (ZSM-5) for the modification of TiO_2 (Huang et al., 2017b; Huang et al., 2017c). The supported TiO_2 on ZSM resulted in the reduction of TiO_2 particle size and the pore size of ZSM, which was beneficial for VOCs adsorption and the effective charge separation in the composite. Such synergistic effect finally enhanced VOCs degradation in the VUV-induced TiO_2 photocatalysis (Huang et al., 2017b; Huang et al., 2017c).

4. TiO_2-based photocatalysts for air pollutant degradation

4.1. VOCs decomposition

VOCs are one of the major group of air pollutants nowadays, which are divided into several subgroups: Monoaromatic hydrocarbons

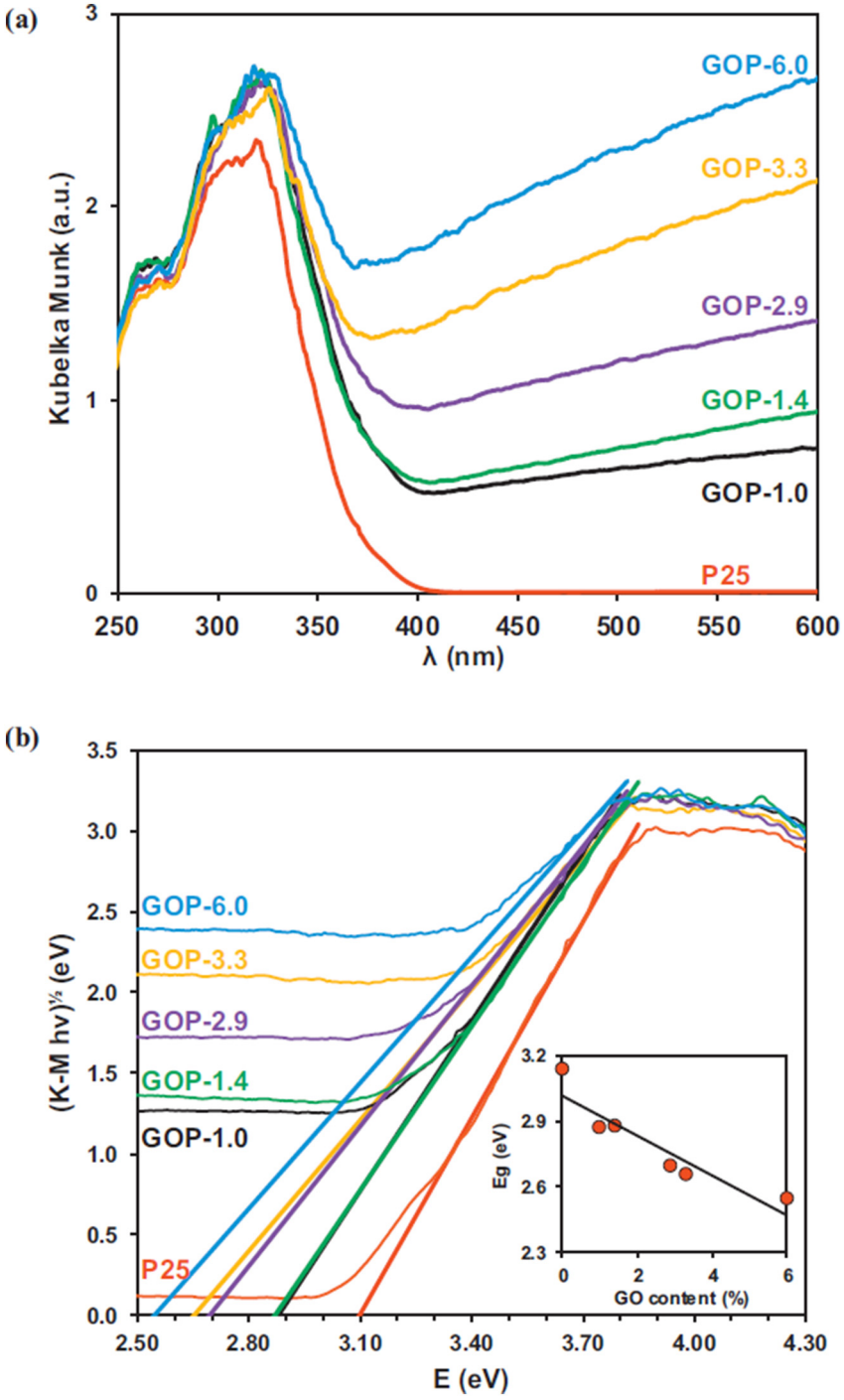

Fig. 7. DRUV spectra of P25 and GOP composites without thermal treatment (a), plot of transformed Kubelka–Munk as a function of the energy of light (b) and correlation between bandgap energy and GO content (b, inset) (Morales-Torres et al., 2013) (Reproduced with permission from Elsevier BV).

(Benzene, Toluene, Ethyl benzene, Xylene: BTEX) (Huang et al., 2017; Shu et al., 2018; Ji et al., 2017; Huang et al., 2016; Huang et al., 2013; Huang et al., 2017b; G.Y. Liu et al., 2017; Huang et al., 2017c; Gholami et al., 2014; Tian et al., 2017; Zhao et al., 2012), carbonyl group (C═O: aldehyde/ketone) compounds and methanol (Cai et al., 2014; Yang et al., 2007), and chlorinated VOCs (CVOCs) (Weng et al., 2019). They are generally produced from combustion of fossil fuel in industrial boilers, internal combustion engines, petrochemical refineries, indoor construction materials like glue and paint, solvents for painting and insect repellent, cooking, office equipment and consumer products (Huang et al., 2017; Shu et al., 2018; Ji et al., 2017; Cai et al., 2014; Huang et al., 2016; Huang et al., 2013; Huang et al., 2017b; G.Y. Liu et al., 2017; Yang et al., 2007; Huang et al., 2017c; Gholami et al., 2014; Tian et al., 2017; Zhao et al., 2012; Wang et al., 2007). It is regarded as precursor of photochemical smog (Shu et al., 2018; Ji et al., 2017; Huang et al., 2016; Huang et al., 2017b; Huang et al., 2017c), ozone formation (Huang et al., 2017c), and fine particulates formation (PM2.5) (Shu et al., 2018; Ji et al., 2017; Lyu et al., 2017). Their adverse effects towards human health include allergies (Zhao et al., 2012), asthma (Zhao et al., 2012), skin disease (Gholami et al., 2014; Tian et al., 2017), sick building syndromes (SBS) (Huang et al., 2017a; Tian et al., 2017; Zhao et al., 2012; Wang et al., 2007), organs attack (Cai

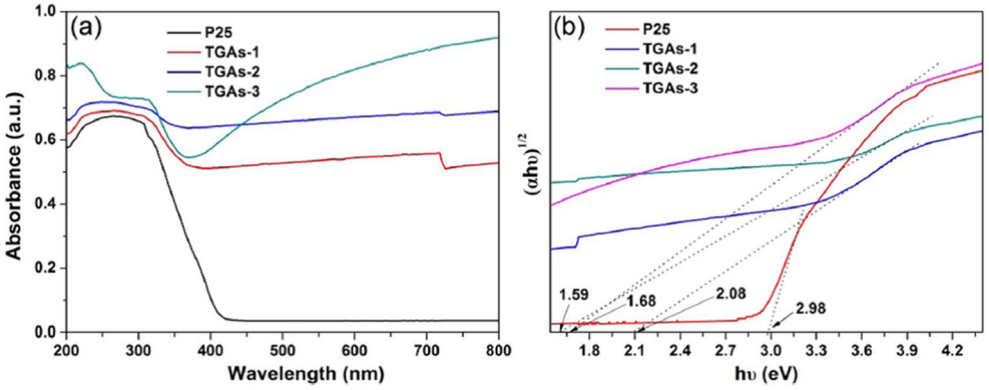

Fig. 8. (a) UV–vis spectra for the pure P25 and TGAs products; (b) the curves of the Kubelka-Munk function plotted against the photon energy (Li et al., 2016) (Reproduced with permission from Elsevier BV).

et al., 2014), chronic respiratory disease (Lyu et al., 2017), heart attack (Lyu et al., 2017), nervous system depression (Gholami et al., 2014; Tian et al., 2017), and even cancer (Shu et al., 2018; Lyu et al., 2017; Huang et al., 2016; Huang et al., 2017b; G.Y. Liu et al., 2017; Yang et al., 2007; Huang et al., 2017c; Gholami et al., 2014; Weng et al., 2019). Environmental damage caused by VOCs included haze (Huang et al., 2013; G.Y. Liu et al., 2017), regional photochemical smog (Shu et al., 2018; Ji et al., 2017; Huang et al., 2016; Huang et al., 2017b; Huang et al., 2017c), greenhouse effect (Gholami et al., 2014), and stratospheric ozone layer depletion (Gholami et al., 2014). So, removal of VOCs becomes an urgent issue for health and ecological protection. Photocatalytic oxidation (PCO) is a method commonly used for VOCs degradation with high efficiency (Cai et al., 2014; Huang et al., 2013; Huang et al., 2017b; Fu et al., 2012; Zhong et al., 2013) and low cost (Wang et al., 2007). This high performance is due to the fact that reactive free radicals and ozone can be effectively produced by the UV sources (254 nm or 185 nm), which can activate the photocatalyst easily (Huang et al., 2013; Huang et al., 2017b; Fu et al., 2012). Such properties are important for the PCO stability and efficiency enhancement (Huang et al., 2013; Huang et al., 2017b; Fu et al., 2012). It is also regarded as one of the energy saving and low cost methods for indoor air quality (IAQ) control (Huang et al., 2013). These strengths made it popular for VOCs decomposition (Shu et al., 2018; Ji et al., 2017; Huang et al., 2017b; Huang et al., 2017c; Zhong et al., 2013). As a result, the use of photocatalyst becomes an important key to achieve effective VOCs decomposition and the removal of residual ozone in the system (Huang et al., 2013; Fu et al., 2012). Up to date, TiO_2 based nanomaterials were extensively used in the gaseous VOCs decomposition with excellent performance. This covered from the pure TiO_2 (Cai et al., 2014; Lyu et al., 2017; Zhong et al., 2013; Stucchi et al., 2018; Xie et al., 2016; K.Y. Chen et al., 2015; Ren et al., 2016), chemically modified TiO_2 (Huang et al., 2013; Huang et al., 2017b; Fu et al., 2012; Yang et al., 2015; Yan et al., 2017; Ratova et al., 2017; Gholami et al., 2014; Zhang et al., 2017; Xiao et al., 2008; H.J. Huang et al., 2009; Yu et al., 2003; J.G. Yu et al., 2009; Yu et al., 2002; Tryba et al., 2018; Asahi et al., 2001; Miyauchi et al., 2004; Ihara et al., 2003; Irokawa et al., 2006; Li et al., 2005), to the carbon-based nanomaterials supported TiO_2 family (Tian et al., 2017; Andryushina and Stroyuk, 2014; Roso et al., 2017; Ebrahimi and Fatemi, 2017; Wang et al., 2012; Jo and Kang, 2013; Roso et al., 2015; M. Li et al., 2017; Yu et al., 2013; Munoz-Batista et al., 2014; Wongaree et al., 2016; Mull et al., 2017; Petronella et al., 2017). Table 1 summarized their corresponding activity. First of all, in the group of pure TiO_2, the VOCs removal efficiency achieved by TiO_2 was in the range of 54–100% in terms of mineralization efficiency (Lyu et al., 2017; Stucchi et al., 2018; Xie et al., 2016; K.Y. Chen et al., 2015; Ren et al., 2016). Origin of the high efficiency in the VOCs removal catalyzed by different TiO_2 under UV-light was mainly the effective charge transfer due to the e^-/h^+ pair separation between TiO_2 and adsorbed VOCs molecules throughout the VOCs degradation process (Lyu et al., 2017; Stucchi et al., 2018; Xie et al., 2016; K.Y. Chen et al., 2015; Ren et al., 2016). In one of the studies of Chen's group, variations of acid treatment (e.g. HF, H_2SO_4, CH_3OOH, HNO_3, and HCl) throughout the TiO_2 nanostructure synthesis resulted in the variation of the VOCs degradation efficiency (K.Y. Chen et al., 2015). They found that in general, the larger the amount of acid used (up to the optimum concentration) throughout the treatment of anatase TiO_2, the stronger the photocatalytic activity achieved in the gaseous toluene decomposition (K.Y. Chen et al., 2015). Reason of the activity enhancement was proposed to be the improved e^-/h^+ pair separation rate due to the improvement in the crystalline structure of the acid treated TiO_2, the introduction of functional groups from acid, or the change in phase of TiO_2 by acid (K.Y. Chen et al., 2015).

Due to the high bandgap of pure TiO_2 limiting its usage as visible-light driven photocatalyst, the use of foreign materials doped TiO_2 becomes the solution. In the category of metal-doped TiO_2 such as transitional metal-doped TiO_2 for VOCs removal, Li et al. (Li et al., 2005) reported the preparation of Ln^{3+} doped TiO_2 catalysts for enhanced photocatalytic oxidation of BTEX for indoor air purification. The enhanced photodegradation of BTEX is possibly due to the improved adsorption ability and the enhanced e^-/h^+ pairs separation due to the presence of Ti^{3+} on the surface of Ln^{3+}–TiO_2 catalysts and the electron transfer between the conduction band/defect level and lanthanide crystal field state (Fig. 9) (Li et al., 2005). Some of the groups use d-block metals like Fe (Yang et al., 2015), Pd, Cu, and Mn (Yan et al., 2017) instead of the f-block metal (Ln^{3+}) as TiO_2 dopant for the VOCs decomposition photocatalyst research due to the relatively high cost of the f-block metal as TiO_2 dopant. In addition to the active free radical and ozone formed by the strong UV source, different results showed that enhanced photocatalytic activity was mainly oriented from (i) the insertion of new energy level to TiO_2 after doping with metal ions (Yang et al., 2015; Yan et al., 2017); (ii) increased surface area of the TiO_2 nanostructures after doping with foreign materials for ozone adsorption (Huang et al., 2013); (iii) effective e^-/h^+ pair separation after doping process with strengthened electronic interaction with ozone molecules (Fu et al., 2012); or (iv) combination of both factors (Huang et al., 2017b). Such hypothesis was reflected from the strong activity achieved in the BTEX removal by Fe-TiO_2 on glass fiber with efficiency varied from 4% (benzene) to 74% (o-xylene) under visible-light source relative to very weak activity achieved by TiO_2 from Yang's group (Yang et al., 2015). Another prove of the mentioned hypothesis was based on the results from Yan's group involving the use of Pd-TiO_2, Cu-TiO_2, and Mn-TiO_2 in the CO_2 reduction to CH_4, where Pd-TiO_2 achieved the strongest conversion activity (Yan et al., 2017). The efficiency of M-doped TiO_2 synthesized by different groups also achieved enhanced activity (Formaldehyde: 65.7–68.8%, benzene: 8–51.5%) over pure TiO_2 (Formaldehyde: 57.4%, benzene: 45.7–50.2%) in the

Table 1
Photocatalytic activity of TiO_2 based materials in VOCs decomposition.

TiO_2 catalysts	Light source	VOCs pollutant	Efficiency (%)	Ref
P25	UV-PCO	Ethanol	~100	(Cai et al., 2014)
P25	UV-PCO	Acetone	~100	(Cai et al., 2014)
MA	UV	Toluene	75 (mineralization)	(Lyu et al., 2017)
MA	UV	Toluene	100	(Lyu et al., 2017)
1% Co-TiO_2	185-PCO	Benzene	51.5	(Huang et al., 2013)
1% Co-TiO_2	254-PCO	Benzene	2	(Huang et al., 2013)
Pd-TiO_2	UV	Formaldehyde	37.6	(Fu et al., 2012)
Pt-TiO_2	UV	Formaldehyde	56.7	(Fu et al., 2012)
Au-TiO_2	UV	Formaldehyde	45.2	(Fu et al., 2012)
Pd-TiO_2	Ozone + UV	Formaldehyde	65.7	(Fu et al., 2012)
Pt-TiO_2	Ozone + UV	Formaldehyde	68.6	(Fu et al., 2012)
Au-TiO_2	Ozone + UV	Formaldehyde	68.8	(Fu et al., 2012)
TiO_2	UV	Toluene	40	(Zhang et al., 2004)
TiO_2/FGFs	UVC-PCO	Ethanol	22.5	(Zhong et al., 2013)
TiO_2/FGFs	UVC-PCO	1-Butanol	9.5	(Zhong et al., 2013)
TiO_2/FGFs	UVC-PCO	Hexane	4	(Zhong et al., 2013)
TiO_2/FGFs	UVC-PCO	Octane	4.2	(Zhong et al., 2013)
TiO_2/FGFs	UVC-PCO	Acetone	20.5	(Zhong et al., 2013)
TiO_2/FGFs	UVC-PCO	MEK	9	(Zhong et al., 2013)
TiO_2/FGFs	UVC-PCO	Toluene	14	(Zhong et al., 2013)
TiO_2/FGFs	UVC-PCO	p-Xylene	4.9	(Zhong et al., 2013)
P25	UV	Formaldehyde	61.0	(Stucchi et al., 2018)
P25	UV	Acetaldehyde	71.6	(Stucchi et al., 2018)
P25	UV	Benzene	62.4	(Stucchi et al., 2018)
P25	UV	Toluene	84.8	(Stucchi et al., 2018)
P25	UV	Methanol	75.9	(Stucchi et al., 2018)
P25	UV	Ethanol	83.1	(Stucchi et al., 2018)
P25	UV	2-Butanone	88.1	(Stucchi et al., 2018)
1077 KRONOS	UV	Formaldehyde	23.6	(Stucchi et al., 2018)
1077 KRONOS	UV	Acetaldehyde	54.9	(Stucchi et al., 2018)
1077 KRONOS	UV	Benzene	31.8	(Stucchi et al., 2018)
1077 KRONOS	UV	Toluene	68.5	(Stucchi et al., 2018)
1077 KRONOS	UV	Methanol	70.7	(Stucchi et al., 2018)
1077 KRONOS	UV	Ethanol	85.3	(Stucchi et al., 2018)
1077 KRONOS	UV	2-Butanone	85.1	(Stucchi et al., 2018)
S3-TiO_2	Sunlight	Acetone	98	(Xie et al., 2016)
S3-TiO_2	Sunlight	Benzene	80	(Xie et al., 2016)
0.5-GF-Fe-TiO_2	UV	Benzene	15	(Yang et al., 2015)
0.01-GF-Fe-TiO_2	Visible-light	Benzene	4	(Yang et al., 2015)
0.5-GF-Fe-TiO_2	UV	Toluene	63	(Yang et al., 2015)
0.01-GF-Fe-TiO_2	Visible-light	Toluene	33	(Yang et al., 2015)
0.5-GF-Fe-TiO_2	UV	Ethylbenzene	79	(Yang et al., 2015)
0.01-GF-Fe-TiO_2	Visible-light	Ethylbenzene	51	(Yang et al., 2015)
0.5-GF-Fe-TiO_2	UV	o-Xylene	86	(Yang et al., 2015)
0.01-GF-Fe-TiO_2	Visible-light	o-Xylene	74	(Yang et al., 2015)
TiO_2/ZnO	UV	Benzene	78	(Gholami et al., 2014)
TiO_2/ZnO	UV	Toluene	93	(Gholami et al., 2014)
TiO_2/WO_3	Visible-light	Toluene	85.3	(Zhang et al., 2017)
0.5 wt%-InVO_4/TiO_2	Visible-light	Benzene	48.7	(Xiao et al., 2008)
$LaVO_4$/TiO_2	UV	Benzene	43	(H.J. Huang et al., 2009)
$LaVO_4$/TiO_2	Visible-light	Benzene	57	(H.J. Huang et al., 2009)
N-T300	UV	Acetaldehyde	100	(Tryba et al., 2018)
N-T300	Visible-light	Acetaldehyde	57	(Tryba et al., 2018)
TiNF/ACF	UV	Toluene	100	(Tian et al., 2017)
PAN/GO + TiO_2	UV	Methanol	100	(Roso et al., 2017)
P25-RGO 0.5%	UV	Acetaldehyde	100	(Ebrahimi and Fatemi, 2017)
P25-RGO 0.5%	Visible-light	Acetaldehyde	69	(Ebrahimi and Fatemi, 2017)
Graphene-TiO_2	UV	Methanol	100	(Roso et al., 2015)
TiO_2/ACFF	UV	Toluene	100	(M. Li et al., 2017)
U100	UV	Formaldehyde	94	(Yu et al., 2013)
1 g-C_3N_4/Ti (1 wt%)	UV	Toluene	1.6	(Munoz-Batista et al., 2014)
1 g-C_3N_4/Ti (1 wt%)	Visible-light	Toluene	1.35	(Munoz-Batista et al., 2014)
THAc-15	UV	Toluene	94.3	(K.Y. Chen et al., 2015)
$THNO_3$-0.75	UV	Toluene	91.6	(K.Y. Chen et al., 2015)
TNS-F	UV	Benzene	60	(Ren et al., 2016)
TNS	UV	Benzene	100	(Ren et al., 2016)
CNT/TiO_2	Visible-light	Toluene	52	(Wongaree et al., 2016)
C2 (1% GO, TiO_2 78 mg)	UV	Butyl Acetate	95	(Mull et al., 2017)
C2 (1% GO, TiO_2 78 mg)	Blue LED	Butyl Acetate	39	(Mull et al., 2017)
Mn/meso-TiO_2	VUV-PCO	Benzene	70	(Shu et al., 2018)
T400	VUV-PCO	Benzene	80	(Ji et al., 2017)
0.1% Mn/TiO_2/ZSM-5	VUV-PCO	Benzene	100	(Huang et al., 2017b)
TiO_2/ZSM-5(200)	VUV-PCO	Benzene	100	(Huang et al., 2017c)
Pd-TiO_2	VUV-PCO	Formaldehyde	95.3	(Fu et al., 2012)

(*continued on next page*)

Table 1 (*continued*)

TiO_2 catalysts	Light source	VOCs pollutant	Efficiency (%)	Ref
Pt-TiO_2	VUV-PCO	Formaldehyde	97.7	(Fu et al., 2012)
Au-TiO_2	VUV-PCO	Formaldehyde	93.6	(Fu et al., 2012)
TiO_2	VUV-PCO	Toluene	56	(Zhang et al., 2004)
TiO_2-FGFs	VUV-PCO	Ethanol	26	(Zhong et al., 2013)
TiO_2-FGFs	VUV-PCO	1-Butanol	17	(Zhong et al., 2013)
TiO_2-FGFs	VUV-PCO	Hexane	11.5	(Zhong et al., 2013)
TiO_2-FGFs	VUV-PCO	Octane	14	(Zhong et al., 2013)
TiO_2-FGFs	VUV-PCO	Acetone	21	(Zhong et al., 2013)
TiO_2-FGFs	VUV-PCO	MEK	11	(Zhong et al., 2013)
TiO_2-FGFs	VUV-PCO	Toluene	17	(Zhong et al., 2013)
TiO_2-FGFs	VUV-PCO	p-Xylene	14	(Zhong et al., 2013)
TiO_2-CCFs	VUV-PCO	Ethanol	34	(Zhong et al., 2013)
TiO_2-CCFs	VUV-PCO	1-Butanol	41	(Zhong et al., 2013)
TiO_2-CCFs	VUV-PCO	Hexane	14	(Zhong et al., 2013)
TiO_2-CCFs	VUV-PCO	Octane	15.5	(Zhong et al., 2013)
TiO_2-CCFs	VUV-PCO	Acetone	24.5	(Zhong et al., 2013)
TiO_2-CCFs	VUV-PCO	MEK	29	(Zhong et al., 2013)
TiO_2-CCFs	VUV-PCO	Toluene	20	(Zhong et al., 2013)
TiO_2-CCFs	VUV-PCO	p-Xylene	21.5	(Zhong et al., 2013)
TiO_2-FG	VUV-PCO	1-Butanol	17	(Farhanian and Haghighat, 2014)
TiO_2-FG	VUV-PCO	n-Hexane	10	(Farhanian and Haghighat, 2014)
TiO_2-FG	VUV-PCO	n-Octane	13	(Farhanian and Haghighat, 2014)
TiO_2-FG	VUV-PCO	MEK	11	(Farhanian and Haghighat, 2014)
TiO_2-FG	VUV-PCO	Acetone	12	(Farhanian and Haghighat, 2014)
TiO_2-FG	VUV-PCO	Toluene	19	(Farhanian and Haghighat, 2014)
TiO_2-FG	VUV-PCO	p-Xylene	7	(Farhanian and Haghighat, 2014)
TiO_2-AC	VUV-PCO	1-Butanol	40	(Farhanian and Haghighat, 2014)
TiO_2-AC	VUV-PCO	n-Hexane	12	(Farhanian and Haghighat, 2014)
TiO_2-AC	VUV-PCO	n-Octane	11	(Farhanian and Haghighat, 2014)
TiO_2-AC	VUV-PCO	MEK	30	(Farhanian and Haghighat, 2014)
TiO_2-AC	VUV-PCO	Acetone	22	(Farhanian and Haghighat, 2014)
TiO_2-AC	VUV-PCO	Toluene	20	(Farhanian and Haghighat, 2014)
TiO_2-AC	VUV-PCO	p-Xylene	18	(Farhanian and Haghighat, 2014)

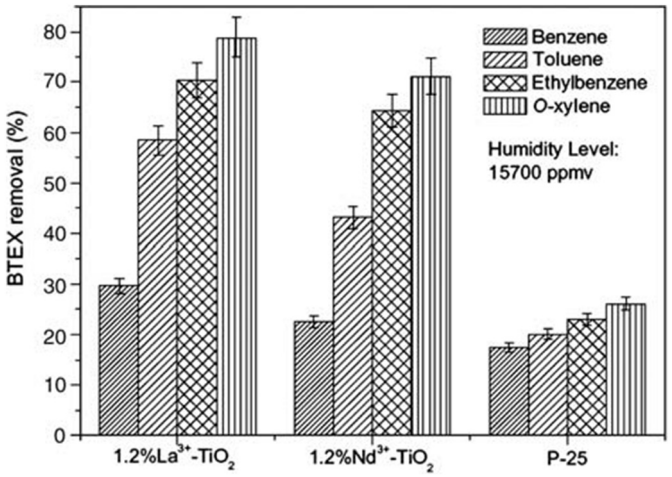

Fig. 9. Photocatalytic removal percentage of benzene, toluene, ethylbenzene and o-xylene in the continuous gas flow reactor with an initial concentration: 23 ± 2 ppbv, residence time: 72 s by using different catalysts at a same humidity level: 15700 ppmv (Li et al., 2005) (Reproduced with permission from Elsevier BV).

same group of UV-PCO assisted VOCs decomposition, and ordinary UV photocatalytic VOCs decomposition (Formaldehyde: 37.6–56.7%) as listed in Table 1 (Huang et al., 2013; Huang et al., 2017b; Fu et al., 2012). It was evidence for the enhanced VOCs degradation activity by the M-doped TiO_2 with hypothesis on the effective charge separation throughout the doping process with enhanced interaction with ozone, and the increase in surface area of TiO_2 after doping (Huang et al., 2013; Huang et al., 2017b; Fu et al., 2012).

Besides the use of monometallic doped TiO_2 based photocatalysts, transitional metal centred multimetallic oxides doped TiO_2 (Xiao et al., 2008; H.J. Huang et al., 2009) and bimetallic codoped TiO_2 (Ratova et al., 2017) were also the targets of investigation. Among them, both $LaVO_4/TiO_2$ nanocomposite (H.J. Huang et al., 2009) and $InVO_4/TiO_2$ nanocomposite (Xiao et al., 2008) achieved very strong activity in the visible-light driven benzene photodecomposition ($LaVO_4/TiO_2$: 57% vs 43% under UV-light (H.J. Huang et al., 2009), $InVO_4/TiO_2$: 48% (Xiao et al., 2008)) with high stability over 5 consecutive runs. For comparison, relatively very weak or even zero activity was recorded when pure TiO_2 materials were used. Their strong activity was originated from the mixing of the energy level between TiO_2 and the multimetal oxides that prevent the e^-/h^+ pair recombination (Xiao et al., 2008; H.J. Huang et al., 2009). At the same time, the Bi-W codoped anatase-TiO_2 achieved a strong activity in acetone degradation under simulated visible-light environment (fluorescent lamp) as reflected from the high level of CO_2 evolved from the catalytic reaction system (Ratova et al., 2017). In contrast, the reactivity in the same reaction was relatively weak when the anatase-TiO_2 was changed to rutile-TiO_2 indicating that the TiO_2's structure strongly affects its photocatalytic activity (Ratova et al., 2017). In addition, the variation in activity was probably caused by the stronger charge carrier dynamic ability since the bandgap of Bi-W codoped TiO_2 species (2.97–3.04 eV) were similar to that of corresponding pure TiO_2 (Anatase: 3.12 eV, rutile: 3.20 eV) (Ratova et al., 2017).

In non-metal elements doped TiO_2, Asahi et al. (Asahi et al., 2001) first reported the visible-light photocatalysis in N-doped TiO_2 samples. They tested various $TiO_{2-x}N_x$ catalysts for VOCs decomposition. These catalysts were found to photodegrade gaseous acetaldehyde (Asahi et al., 2001), 2-propanol (Miyauchi et al., 2004), acetone (Ihara et al., 2003) and benzene (Kannangara et al., 2018) by visible-light irradiation. Irokawa et al. (2006) reported the photooxidation of aromatics over nitrogen-doped TiO_2 ($TiO_{2-x}N_x$) under visible-light irradiation. Results indicated that toluene, which could weakly adsorb on the catalyst surface, is initially photooxidized to benzaldehyde. This oxidized

species adsorbs onto the $TiO_{2-x}N_x$ surface more strongly, leading to the formation of ring-opening products such as carboxylic acids and aldehydes. Major intermediates adsorbed on the catalyst surface were gradually photodegraded to CO_2 and H_2O even under visible-light irradiation. In another example carried out by Tryba's group, they observed that the N-doped TiO_2 (N-T300) exhibited strong activity in the photocatalytic degradation of formaldehyde under UV light (~100%) as compared to that of pure TiO_2 (~95%) by taking into account the CO_2 formation due to the acetaldehyde decomposition (Tryba et al., 2018). In contrast, the activity in the same reaction was reduced (N-T300: 57% vs pure TiO_2: 77%) when fluorescent lamp was used as a simulated visible-light source (Tryba et al., 2018). Besides N-doped TiO_2, fluorine-doped TiO_2 (F-doped TiO_2) also played an active role in gas phase VOCs degradation via UV-PCO, where acetone was chosen as the candidate (Yu et al., 2003; J.G. Yu et al., 2009; Yu et al., 2002). Overall performance of F-doped TiO_2 was stronger than pure TiO_2. It was indicated by strong kinetics exhibited by different F-doped TiO_2 ($4.05 \times 10^{-5}\,s^{-1}$ and 5.81×10^{-3}–$17.35 \times 10^{-3}\,min^{-1}$) when compared with that achieved by pure P25 ($2 \times 10^{-5}\,s^{-1}$ and 4.19×10^{-3}–$6.33 \times 10^{-3}\,min^{-1}$) in acetone degradation (Yu et al., 2003; J.G. Yu et al., 2009; Yu et al., 2002). The activity enhancement was proposed to be (i) e^-/h^+ pairs recombination was inhibited due to the presence of trifluoroacetic acid (TFA) bound on TiO_2 surface which acted as electron scavenger (Yu et al., 2003), (ii) strong electron withdrawing ability exhibited by the Ti—F bond on F-TiO_2 surface (J.G. Yu et al., 2009), or (iii) prevention of TiO_2 phase change from anatase to rutile and with crystallinity improvement of the anatase upon F-doping (Yu et al., 2002).

MO_x-TiO_2 was also commonly investigated for VOCs degradation (Gholami et al., 2014; Zhang et al., 2017). One of the studies was carried out by Gholami's who used TiO_2/ZnO as photocatalyst for the removal of BTEX under UV-light irradiation (Gholami et al., 2014). The photocatalyst showed high activity in photocatalytic decomposition of toluene and benzene with 93% and 78% removal efficiency, respectively (Gholami et al., 2014). The degradation was ascribed to the direct oxidation by the holes formed from the TiO_2/ZnO or the hydroxyl radicals produced from the water vapor in the presence of UV-light and TiO_2/ZnO (Gholami et al., 2014). In the case of TiO_2/WO_3, toluene removal efficiency reached ~90% under visible-light irradiation. It was approximately two times stronger than that achieved by corresponding pure components (TiO_2 nanofiber, P25, and WO_3 nanoparticles) (Zhang et al., 2017). The enhanced photocatalytic activity in toluene decomposition was probably due to the narrowed bandgap to visible-light range, which was coherent to the DRS results of the TiO_2/WO_3 (Zhang et al., 2017).

The use of carbon based nanomaterials as TiO_2 support was also an alternative to VOCs degradation. Among them, GO supported TiO_2 photocatalyst occupied a large portion in literature (Andryushina and Stroyuk, 2014; Roso et al., 2017; Ebrahimi and Fatemi, 2017; Wang et al., 2012; Jo and Kang, 2013; Roso et al., 2015; Mull et al., 2017). Insertion of graphene nanosheets to TiO_2 through hybrid synthesis resulted in an enhancement of the photocatalytic decomposition activity under different light sources (Andryushina and Stroyuk, 2014; Roso et al., 2017; Ebrahimi and Fatemi, 2017; Wang et al., 2012; Jo and Kang, 2013; Roso et al., 2015; Mull et al., 2017). This was reflected from the high conversion efficiency (Visible-light: 39–69% (Ebrahimi and Fatemi, 2017; Mull et al., 2017)) (UV-light: 80–100% (Roso et al., 2017; Ebrahimi and Fatemi, 2017; Roso et al., 2015; Mull et al., 2017)), low outlet/inlet VOCs ratio (Jo and Kang, 2013), or strong kinetics (Andryushina and Stroyuk, 2014; Wang et al., 2012) when compared to those of corresponding pure TiO_2 structures (Andryushina and Stroyuk, 2014; Wang et al., 2012; Jo and Kang, 2013) (conversion efficiency: 51–92% (visible-light) (Roso et al., 2015; Mull et al., 2017); 78–100% (UV) (Roso et al., 2017; Ebrahimi and Fatemi, 2017; Roso et al., 2015; Mull et al., 2017)). Such phenomenon resulted from (i) effective charge transfer from TiO_2 to the adsorbed VOCs molecules via graphene due to the narrowing of the bandgap (Wang et al., 2012; Jo and Kang, 2013), (ii) interaction between TiO_2 and graphene nanosheets support for the acceptance of photoelectron to target VOCs molecule (Andryushina and Stroyuk, 2014; Roso et al., 2015; Mull et al., 2017), or (iii) existence of both factors as mentioned above (Roso et al., 2017; Ebrahimi and Fatemi, 2017).

Relatively, the use of carbon fiber (ACF) supported TiO_2 (Tian et al., 2017; M. Li et al., 2017), CNT supported TiO_2 (Wongaree et al., 2016) and g-C_3N_4 supported TiO_2 (Yu et al., 2013; Munoz-Batista et al., 2014) were relatively few in number in the VOCs investigations. In this group of photocatalysts, they exhibited strong activity in the VOCs decomposition with removal efficiency in the range of 1.6–100% under UV-light (Tian et al., 2017; M. Li et al., 2017; Yu et al., 2013; Munoz-Batista et al., 2014) or 1.4–52% under visible-light source (Munoz-Batista et al., 2014; Wongaree et al., 2016) for different kinds of VOCs as compared to that of pure TiO_2 (UV-light: 0.9–65.4%, visible-light: 0.9–18%) (Tian et al., 2017; M. Li et al., 2017; Munoz-Batista et al., 2014; Wongaree et al., 2016). Some of the tests showed that the catalyst exhibited strong stability after multiple runs with low activity depreciation (Tian et al., 2017). Major reason of activity enhancement was the synergistic effect exhibited between TiO_2 and the carbon supports by (i) effective e^-/h^+ pairs separation due to the narrowing of bandgap (Tian et al., 2017; Yu et al., 2013; Munoz-Batista et al., 2014), (ii) effective adsorption of VOC molecules on photocatalyst surface (Wongaree et al., 2016), or (iii) combination of these factors (M. Li et al., 2017).

However, traditional PCO reactions also have some drawbacks, especially the photocatalyst deactivation, quick e^-/h^+ pairs recombination, and low efficiency (Ji et al., 2017; Huang et al., 2013; Huang et al., 2017b; Huang et al., 2017c; Fu et al., 2012; Zhang et al., 2004). Use of VUV lamp alone for the VOCs degradation also associated with the problem of ozone formation, which is a harmful secondary air pollutant (Shu et al., 2018; Huang et al., 2017c; Fu et al., 2012). In order to overcome the limitation mentioned previously, combining VUV and PCO became an alternative solution (Shu et al., 2018; Ji et al., 2017; Huang et al., 2017c; Fu et al., 2012; Zhang et al., 2004; Zhong et al., 2013; Farhanian and Haghighat, 2014). To maximize the efficiency of VOCs decomposition and the effective residual ozone decomposition throughout the VUV-PCO reactions, use of correct photocatalyst candidate became an important factor. TiO_2 based catalyst, no matter pure TiO_2 or chemically modified TiO_2 as listed in Table 1, played an important role in such reaction. Different results showed that the VOCs removal efficiency lied in the range of 7–100% for pure TiO_2 catalyzed VUV-PCO (Ji et al., 2017; Huang et al., 2017c; Zhang et al., 2004; Zhong et al., 2013; Farhanian and Haghighat, 2014) and 70–97.7% for the M-doped TiO_2 catalyzed VUV-PCO (Shu et al., 2018; Fu et al., 2012). The comparison of VUV-PCO and normal UV-PCO under identical reaction conditions and with same group of TiO_2 photocatalyst clearly showed that the use of VUV as light source enhanced the PCO assisted VOCs photodegradation strongly (2–3 times, Table 1) (Fu et al., 2012; Zhong et al., 2013). Sometime the use of nanoporous structure as supporting materials for the chemically modified TiO_2 could further enhance catalytic activity for VOCs degradation. Effective Mn/TiO_2/ZSM-5 catalyzed benzene degradation via VUV-PCO carried out by Huang's group was a representative, which achieved 100% benzene removal efficiency and could keep stable for 6 h when compared with corresponding pure components (i.e. Mn/ZSM-5, TiO_2, ZSM-5, and TiO_2/ZSM-5) (Huang et al., 2017b). Besides the presence of strong oxidizing species of ozone, the enhancements of the PCO VOCs decomposition was possibly caused by the following reasons. (i) Effective e^-/h^+ pairs separation by the reduction of bandgap in the M-doped TiO_2 photocatalyst for the effective production of hydroxyl radicals on the catalyst surface for the VOCs degradation (Shu et al., 2018; Fu et al., 2012); (ii) large specific surface area provided by TiO_2 photocatalyst (Zhong et al., 2013); (iii) optimum structure provided by the pure TiO_2 for proceeding VUV-PCO VOCs photodegradation (Ji

et al., 2017; Huang et al., 2017c); or (iv) synergistic effect exhibited between the dopant, TiO_2 and the nanoporous support for VOCs degradation via VUV-PCO (Huang et al., 2017b).

Up to date, such reactions only deal with single contaminant in the gaseous samples (Huang et al., 2013; Huang et al., 2017b; Fu et al., 2012), which could not reflect their actual ability with mixed contaminants. Some research groups were then carried out TiO_2 catalyzed UV-PCO reactions with a mixture of simulated indoor contaminants (Cai et al., 2014; Zhong et al., 2013). The simulated air sample composed of either 2 components (Acetone and ethanol) (Cai et al., 2014) or as much as 8 components in a single pass operation (Zhong et al., 2013). Even though only pure TiO_2 on the fiber substrate (TiO_2/FGFs) or commercial P25 was used as photocatalyst, they still exhibited strong activity in the UV-PCO assisted multi-VOCs decomposition (Cai et al., 2014; Zhong et al., 2013). This is reflected from the removal percentage in the range of 4–~100% as listed in Table 1. No matter pure TiO_2 or chemically modified TiO_2 were used, UV-PCO reaction was sensitive towards humidity and flow rate of inlet gas (Cai et al., 2014; Zhong et al., 2013), and even the amount of ozone in the system altogether (Huang et al., 2013; Fu et al., 2012; Zhong et al., 2013). Cai's group observed that the coexistence of either acetone or ethanol in the counterpart of the photodecomposition system resulted in activity inhabitation (Cai et al., 2014).

However, relative to the huge effort on the laboratory batch testing level in this topic, testing in the integration with air purifier level or under the emission chamber testing level only occupied a small fraction, no matter visible-light PCO (Mull et al., 2017), UV-PCO (Zhong et al., 2013; Farhanian and Haghighat, 2014; Wongaree et al., 2016; Mull et al., 2017), or UV-PCO/VUV-PCO type hybrid system (Zhong et al., 2013; Farhanian and Haghighat, 2014). For example, the air cleaning simulation of VOCs by TiO_2 loaded graphene showed strong toluene removal efficiency over 95% in a 20 L chamber under UV-light source carried out by Mull's group (Mull et al., 2017). On the other hand, the CNT/TiO_2 achieved 52% toluene removal in the visible-light driven air purifier simulator investigation performed by Suligoj's group (Wongaree et al., 2016). While in the UV-PCO/VUV-PCO simulator built up by Zhong et al. (2013) with the use of 4-ducts air cleaner simulator system as shown in Fig. 10, the efficiency for the simulated indoor air contaminants removal achieved by TiO_2/FGFs or TiO_2/CCFs filter equipped with UV-PCO/VUV-PCO air cleaning simulator lied in the range of 4–22.5% (TiO_2/FGFs) in UV-PCO, and 11.5–26% (TiO_2/FGFs) and 14–41% (TiO_2/CCFs) in VUV-PCO with the same group of simulated VOCs pollutants as listed in Table 1 (Zhong et al., 2013). As illustrated in Fig. 11, such system was effective for simultaneous comparison of the photocatalytic activity of UV-PCO against VUV-PCO in single run with TiO_2/FGFs and TiO_2/CCFs as air cleaning filter (Zhong et al., 2013). Farhanian and Haghighat (2014) studied VOCs degradation by TiO_2/FG and TiO_2/AC filters under VUV and UVC light sources in a similar reactor as Zhong et al. (2013). Results from Table 1 reflected that TiO_2/AC had better activity than TiO_2/FG in the VOCs removal under VUV light sources in air cleaners (Farhanian and Haghighat, 2014).

4.2. Degradation of nitrogen family air pollutants

Another important group of air pollutant is nitrogenous pollutants, such as nitric oxides (NO_x) (Xu et al., 2017; Trapalis et al., 2016; Y.X. Liu et al., 2017; Papailias et al., 2017; Y.X. Liu et al., 2018; Chaisiwamongkhol et al., 2017; Ma et al., 2016; Teramura et al., 2004; Han et al., 2016; Yuan et al., 2012; Song et al., 2012; Boyjoo et al., 2017) and NH_3 (Yamazoe et al., 2008; Kolinko and Kozlov, 2009). Common sources include the combustion of fossil fuel in industrial boilers and internal combustion engines, indoor construction materials like concrete freezing point depression admixture, fertilizer production, and exhaust gas from sewage treatment plants and sewage from chemical plants. They are regarded as the major sources of photochemical smog (Xu et al., 2017; Trapalis et al., 2016; Y.X. Liu et al., 2017; Y.X. Liu et al., 2018; Chaisiwamongkhol et al., 2017; Ma et al., 2016; Teramura et al., 2004; Han et al., 2016; Yuan et al., 2012; Song et al., 2012), acid rain (Xu et al., 2017; Trapalis et al., 2016; Y.X. Liu et al., 2017; Papailias et al., 2017; Y.X. Liu et al., 2018; Chaisiwamongkhol et al., 2017; Ma et al., 2016; Teramura et al., 2004; Han et al., 2016; Yuan et al., 2012; Song et al., 2012; Boyjoo et al., 2017), odor (Chaisiwamongkhol et al., 2017), ground-level ozone production (Xu et al., 2017; Boyjoo et al., 2017), fine particulates (PM2.5) (Y.X. Liu et al., 2017), and even global warming (Reli et al., 2016; Koci et al., 2017; Boyjoo et al., 2017). Exposure to them can cause serious disease such as respiratory attack (Trapalis et al., 2016; Chaisiwamongkhol et al., 2017; Boyjoo et al., 2017), immune system disease (Boyjoo et al., 2017), asthma (Seifvand and Kowsari, 2015), and on-job disease (Kolinko and Kozlov, 2009). This group of pollutant can also cause vegetation damage (Chaisiwamongkhol et al., 2017), building corrosion (Chaisiwamongkhol et al., 2017), haze (Y.X. Liu et al., 2018; Ma et al., 2016), tropospheric ozone layer depletion (Papailias et al., 2017; Yuan et al., 2012; Song et al., 2012; Koci et al., 2017), regional acid rain (Xu et al., 2017; Trapalis et al., 2016; Y.X. Liu et al., 2017; Papailias et al., 2017; Y.X. Liu et al., 2018; Chaisiwamongkhol et al., 2017; Ma et al., 2016; Teramura et al., 2004; Han et al., 2016; Yuan et al., 2012; Song

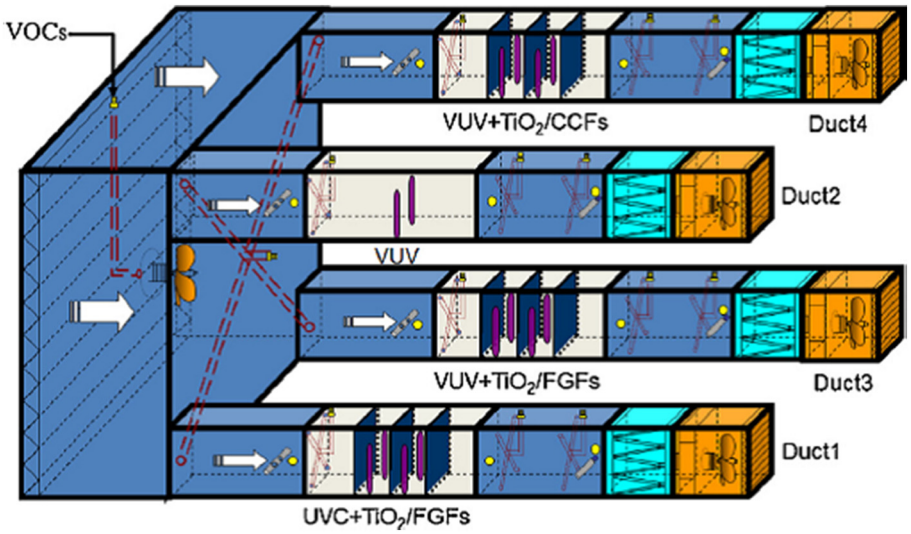

Fig. 10. Schematic diagram of the UV-PCO system (Zhong et al., 2013) (Reproduced with permission from Elsevier BV).

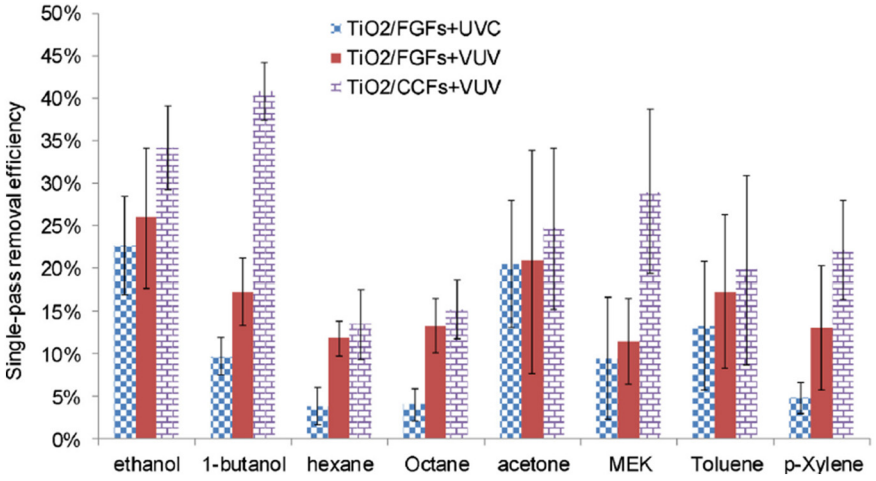

Fig. 11. Single-pass removal efficiencies of various VOCs under three different experimental scenarios (inlet concentration = 500 ppb, RH = 15–45%, airflow rate = 170 m^3/h, irradiance = 27–36 W/m^2) (Zhong et al., 2013) (Reproduced with permission from Elsevier BV).

et al., 2012; Boyjoo et al., 2017) and photochemical smog (Xu et al., 2017; Trapalis et al., 2016; Y.X. Liu et al., 2017; Y.X. Liu et al., 2018; Chaisiwamongkhol et al., 2017; Ma et al., 2016; Teramura et al., 2004; Han et al., 2016; Yuan et al., 2012; Song et al., 2012). Removing those nitrogenous pollutants became an urgent challenge. Same as VOCs decomposition, concept of photocatalytic oxidation (PCO) was also applied in the NO_x decomposition. TiO_2 based materials also played an important role in the gas phase photocatalytic nitrogen-containing pollutants decomposition (NO_x and NH_3). Pure TiO_2 (Chaisiwamongkhol et al., 2017; Yuan et al., 2012; Bianchi et al., 2015; Zhao et al., 2009; Zhao et al., 2008), metal doped (Xu et al., 2017; Seifvand and Kowsari, 2016; Rodriguez et al., 2017; Tan et al., 2017; Song et al., 2012), non-metallic elements doped (Janus et al., 2015), and multiple element doped TiO_2 based compounds (Han et al., 2016), and carbon nanomaterials supported TiO_2 (Trapalis et al., 2016; Papailias et al., 2017; Seifvand and Kowsari, 2015; Ma et al., 2016; Neppolian et al., 2015; Yang et al., 2017; Y.H. Li et al., 2017; Song et al., 2016; Reli et al., 2016; Koci et al., 2017; Paz, 2010) occupied a large portion. Corresponding activity was summarized in Table 2. In the topic of NO_x removal, mechanism of TiO_2 catalyzed photocatalytic NO_x degradation is summarized in Fig. 12 (Chaisiwamongkhol et al., 2017). Pure TiO_2 (or P25) generally has good NO_x removal performance under a UV-light source and the NO_x removal percentage lied in the range of 31–99% (Chaisiwamongkhol et al., 2017; Yuan et al., 2012; Bianchi et al., 2015; Zhao et al., 2009; Zhao et al., 2008), depending on the structure of the TiO_2 used in the NO_x removal process (Chaisiwamongkhol et al., 2017; Bianchi et al., 2015). However, some of the works showed a decline in activity to lower than 60% after 68–100 min operation when commercial TiO_2 (P25) or synthetic TiO_2 from different Ti precursors were used. Among them, synthetic TiO_2 exhibited better stability due to the lower decline rate of NO_x removal efficiency below 60% (Chaisiwamongkhol et al., 2017). In addition, its performance was humidity sensitive in the humidity range of 12–60%, where the best performance was recorded at the humidity of 12%. It was because the hydroxyl radical formation was inhibited under high humidity of 60% (Chaisiwamongkhol et al., 2017).

When the photocatalyst changed from pure TiO_2 to foreign material doped TiO_2, their performance was elevated like M-doped TiO_2 (e.g. Pd, Ag, Au, Pt, Ti) (Xu et al., 2017; Seifvand and Kowsari, 2016; Rodriguez et al., 2017; Tan et al., 2017). This is reflected from the strong NO_x removal efficiency in the range of 55–100% compared to that of pure TiO_2 (40–90%) with high stability and selectivity under the same reaction conditions but with different light sources as carried out by different groups (Xu et al., 2017; Seifvand and Kowsari, 2016; Rodriguez et al., 2017; Tan et al., 2017). Such strong activity came from (i) the narrowing of bandgap after the doping of TiO_2 by metals (Seifvand and Kowsari, 2016; Tan et al., 2017), or (ii) plasma effect exhibited by the metal (Ag, Au, Pt) dopant (Xu et al., 2017; Rodriguez et al., 2017) However, their activity was also strongly related to the loading level of the foreign materials (Xu et al., 2017), or the humidity of the reaction system (Rodriguez et al., 2017). Interestingly, one of the studies carried out by Song's group found that 0.5 wt% Pt-TiO_2 (pH 7) achieved strong NO degradation under UV-PCO reaction with the recorded value of 86% (Table 2), but the photocatalytic activity of Pt-TiO_2 was strongly dependent on the pH of the raw solution in the synthesis (Song et al., 2012).

In non-metal and multi-element doped TiO_2, such as C-N codoped TiO_2 (Janus et al., 2015), their activity towards NO_x photodecomposition was strongly affected by the amount of TiO_2 used in the gypsum loading process, and the treatment temperature throughout the carbon/nitrogen doping step. The best value of NO_x degradation efficiency (~20%) achieved over g + TiO_2/N-C-300-20% when 20 wt% TiO_2 and a treatment temperature of 300 °C was applied throughout the TiO_2/N-C synthesis (Janus et al., 2015). Such activity was 2.5–10 times stronger than those achieved by pure gypsum and 10 wt% TiO_2 modified gypsum in the same reaction. Activity depreciation was recorded when the recipe deviated from the optimum value of 300 °C and 10 wt% TiO_2 (Janus et al., 2015). Origin of such finding was proposed to be the presence of the ammonium group on the photocatalyst surface and the large surface area together based on the DRS result recorded by Janus' group (Janus et al., 2015). Another study carried out by Han's group involving the use of N-Zr-Ni tridoped TiO_2 under visible-light (Han et al., 2016). They showed that the visible-light induced PCO of NO decomposition achieved by this material (56.8%, Table 2) was much stronger than that of pure TiO_2 due to the mixing of the crystal structure between TiO_2 and dopants together (Han et al., 2016). It showed that the correct selection of dopant may be important to the TiO_2 activity enhancement in NO_x degradation.

The use of carbon materials supported TiO_2 also showed enhanced activity in NO_x degradation. When TiO_2 loaded graphene was used, the activity elevated to 31–43% in TiO_2/GO and TiO_2/rGO (vs ~16–24% in pure TiO_2), respectively (Trapalis et al., 2016; Seifvand and Kowsari, 2015). Origin of the activity enhancement was proposed to be the effective e^-/h^+ pair separation by the GO support (Trapalis et al., 2016; Seifvand and Kowsari, 2015). The only difference was that the activity was affected by the amount of GO used with the fixed amount of TiO_2 in the raw solution when synthesizing TiO_2/graphene as photocatalyst (Trapalis et al., 2016). In one of the studies carried out by Xu's group, the activity of TiO_2/graphene in NO_x removal under UV-light was better than that under visible-light as reflected from the NO_x removal

Table 2
Photocatalytic activity of TiO_2 based materials in nitrogen group pollutant decomposition.

Catalysts	Light source	Target	Efficiency (%)	Ref
1 wt% Ag/TiO_2	UV/visible-light	NO	100	(Xu et al., 2017)
TiO_2/G-1 (0.01%)	UV	NO/NO_2 mixture	35.40	(Trapalis et al., 2016)
TiO_2/G-1 (0.01%)	Visible-light	NO/NO_2 mixture	22.75	(Trapalis et al., 2016)
TiO_2/rGO-2 (0.1%)	UV	NO/NO_2 mixture	42.86	(Trapalis et al., 2016)
TiO_2/rGO-2 (0.1%)	Visible-light	NO/NO_2 mixture	22.34	(Trapalis et al., 2016)
MTi5	UV	NO/NO_2 mixture	22.5	(Papailias et al., 2017)
MTi5	Visible-light	NO/NO_2 mixture	18	(Papailias et al., 2017)
TTIP-TiO_2	UV	NO_2	60	(Chaisiwamongkhol et al., 2017)
TiO_2/FGO	UV	NO/NO_2 mixture	51	(Seifvand and Kowsari, 2015)
M400	UV	NO/NO_2 mixture	38	(Ma et al., 2016)
M400	Visible-light	NO/NO_2 mixture	27	(Ma et al., 2016)
JRC-TIO-4	UV-PSCR	NO	83	(Teramura et al., 2004)
Pd/IL-TiO_2	UV	NO_x mixture	88	(Seifvand and Kowsari, 2016)
N-Zr-Ni-TiO_2	Vis-PCO	NO	56.8	(Han et al., 2016)
TAS	UV	NO	31	(Yuan et al., 2012)
TiO_2	UV-A	NO/NO_2 mixture	97	(Bianchi et al., 2015)
P25	UV-A	NO/NO_2 mixture	99	(Bianchi et al., 2015)
Au-P	UV	NO	97	(Rodriguez et al., 2017)
Au-P	Visible-light	NO	10	(Rodriguez et al., 2017)
Au-C	UV	NO	90	(Rodriguez et al., 2017)
Au-C	Visible-light	NO	22	(Rodriguez et al., 2017)
Pt-P	UV	NO	45	(Rodriguez et al., 2017)
Pt-P	Visible-light	NO	13	(Rodriguez et al., 2017)
Pt-C	UV	NO	80	(Rodriguez et al., 2017)
Pt-C	Visible-light	NO	18	(Rodriguez et al., 2017)
Ti-TiO_2 mesocrystal	Visible-light	NO	55	(Tan et al., 2017)
Pt-TiO_2	UV-PCO	NO	86	(Song et al., 2012)
g + TiO_2/N, C-300-20%	UV	NO/NO_2 mixture	20	(Janus et al., 2015)
S15	Visible-light	NO	37.4	(Y.H. Li et al., 2017)
CT10	UV	NO	59.4	(Song et al., 2016)
CT10	Visible-light	NO	12.6	(Song et al., 2016)
(0.3/1) TiO_2/g-C_3N_4	UV	N_2O	57	(Reli et al., 2016)
TiO_2/g-C_3N_4 (1:2)	UV-C	N_2O	68	(Koci et al., 2017)
TiO_2/g-C_3N_4 (1:2)	UV-A	N_2O	68	(Koci et al., 2017)
TiO_2	UV	NO	50	(Zhao et al., 2009)
TiO_2	UV	NO	67	(Zhao et al., 2008)
TiO_2	UV-PSCO	NH_3	100	(Yamazoe et al., 2008)
1 wt% Ag($h\upsilon$)/TiO_2	UV-PCO	NH_3	75	(Kolinko and Kozlov, 2009)
1 wt% Ag($NaBH_4$)/TiO_2	UV-PCO	NH_3	73	(Kolinko and Kozlov, 2009)
1 wt% Au($h\upsilon$)/TiO_2	UV-PCO	NH_3	62	(Kolinko and Kozlov, 2009)
1 wt% Au($NaBH_4$)/TiO_2	UV-PCO	NH_3	48	(Kolinko and Kozlov, 2009)
1 wt% Pd/TiO_2	UV-PCO	NH_3	56	(Kolinko and Kozlov, 2009)
0.2 wt% Pt/TiO_2	UV-PCO	NH_3	58	(Kolinko and Kozlov, 2009)
0.01 wt% Fe_2O_3/TiO_2	UV-PCO	NH_3	70	(Kolinko and Kozlov, 2009)
0.1 wt% Fe_2O_3/TiO_2	UV-PCO	NH_3	4	(Kolinko and Kozlov, 2009)
0.5 wt% CoO/TiO_2	UV-PCO	NH_3	74	(Kolinko and Kozlov, 2009)
0.05 wt% MoO_3/TiO_2	UV-PCO	NH_3	38	(Kolinko and Kozlov, 2009)
0.05 wt% V_2O_5/TiO_2	UV-PCO	NH_3	55	(Kolinko and Kozlov, 2009)
1 wt% NiO/TiO_2	UV-PCO	NH_3	97	(Kolinko and Kozlov, 2009)
TiO_2	UV-PCO	NH_3	71	(Kolinko and Kozlov, 2009)
4 M H_2SO_4/TiO_2	UV-PCO	NH_3	65	(Kolinko and Kozlov, 2009)

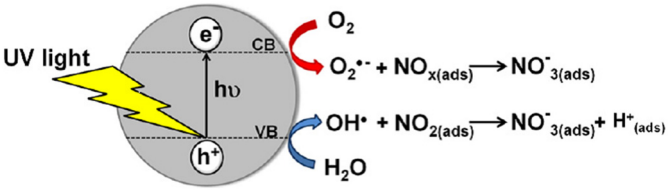

Fig. 12. Schematic diagram represents the overall mechanism of photocatalytic process of TiO_2 on NO_2 degradation. CB: conduction band; VB: valence band (Chaisiwamongkhol et al., 2017) (Reproduced with permission from Elsevier BV).

efficiency achieved under different light sources (Trapalis et al., 2016). Another investigation carried out by Kowsari's group showed that the TiO_2 loaded on functionalized GO support illustrated better activity than both pure TiO_2 and TiO_2/GO in UV-light assisted NO_x degradation under identical reaction condition (Seifvand and Kowsari, 2015). The use of non-graphene carbon based material supported TiO_2 for the NO_x reduction was also popular, g-C_3N_4 supported TiO_2 occupied a major portion among them with the use of different light sources (Papailias et al., 2017; Ma et al., 2016; Y.H. Li et al., 2017; Song et al., 2016; Reli et al., 2016; Koci et al., 2017). Generally, g-C_3N_4 supported TiO_2 photocatalyst exhibited excellent N_xO_y removal efficiency (visible-light: 12.6–37.4%, UV-light: 21.5–68%) (Papailias et al., 2017; Ma et al., 2016; Y.H. Li et al., 2017; Song et al., 2016; Reli et al., 2016; Koci et al., 2017) with high selectivity (Ma et al., 2016) when compared to corresponding pure TiO_2 catalyst (Conversion: 0–17% (visible-light), 23.3–68% (UV-light)) (Papailias et al., 2017; Ma et al., 2016; Y.H. Li et al., 2017; Song et al., 2016; Reli et al., 2016; Koci et al., 2017). Some of the studies showed high stability after multi-cycle operation (Song et al., 2016). The origin of the activity enhancement was proposed to be arisen from (i) bandgap reduction by interaction between g-C_3N_4 and TiO_2 (Papailias et al., 2017; Ma et al., 2016; Y.H. Li et al., 2017; Reli et al., 2016; Koci et al., 2017), or the effective e^-/h^+ pairs separation in the composite (Y.H. Li et al., 2017; Song et al., 2016; Reli et al., 2016; Koci et al., 2017); and (ii) the large surface area exhibited with

reduction in crystalline size from the TiO_2/g-C_3N_4 composite (Reli et al., 2016). Interestingly, Papailias et al. (2017) found that the addition of $CaCO_3$ as additive for the TiO_2/g-C_3N_4 synthesis (MTi5 and MTi10) can simultaneously remove the NO_x and purify air (i.e. toxicity reduction in air sample by suppressing NO_2 intermediates). This is reflected by the positive value of $DeNO_x$ index recorded from MTi5 and MTi10 under both UV-light and visible-light environment, while pure Ti or g-C_3N_4 generally achieved negative or very small positive $DeNO_x$ index in the same study (Papailias et al., 2017). This index was used for evaluating the effectiveness of NO_x abatement by MTi_x, which was obtained by subtracting the change in NO concentration (Δ(NO): ppm) with 3 times of the change in NO_2 concentration (Δ(NO_2): ppm) throughout the operation. Corresponding formula was shown below:

$$DeNO_x \text{ index} = \Delta(NO) - 3 \times \Delta(NO_2) \text{ [10]}$$

Besides light source induced PCO, use of selective catalytic reduction (SCR) reaction was another pathway. One example was TiO_2 catalyzed UV photo-SCR (UV-PSCR) for the NO removal carried out by Teramura's team, where NH_3 was used as additive for the NO photocatalytic reduction with the mechanism as proposed in Fig. 13 (Teramura et al., 2004). Results showed that the TiO_2 candidate of JRC-TIO-4 (Anatase + Rutile hybrid) showed the best performance in the UV-light induced PSCR NO removal, which is reflected from the NO conversion level of 83% with 96% selectivity towards N_2 as the ultimate product (Teramura et al., 2004). Strong activity of the photocatalyst was proposed to be the optimum surface acid properties of JRC-TIO-4 for the NH_3 adsorption throughout the NO removal process (Teramura et al., 2004).

Relative to the huge amount of works on the gas phase nitrogen oxides removal research as described previously, research on the gas phase NH_3 was relatively few in number to our best knowledge (Yamazoe et al., 2008; Kolinko and Kozlov, 2009). These reactions were PCO (Kolinko and Kozlov, 2009) or photo selective catalytic oxidation (PSCO) (Yamazoe et al., 2008). The overall reaction and mechanism using NH_3 PSCO as representative are shown as below (Yamazoe et al., 2008):

Overall reaction:

$$4NH_3 + 3O_2 \rightarrow 2N_2 + 6H_2O$$

Mechanism:

$$NH_3(+O) \rightarrow NH_2 + H^+(O) + e^-$$

$$NH_2 + O_2 \rightarrow NO + H_2O$$

$$NH_2 + NO \rightarrow NH_2NO$$

$$NH_2NO_2 \rightarrow N_2 + H_2O$$

Pure TiO_2 (Yamazoe et al., 2008; Kolinko and Kozlov, 2009) and M-doped TiO_2, MO_x-doped TiO_2 (Kolinko and Kozlov, 2009) were used as photocatalyst for NH_3 removal reaction. There was also systematic comparison between the M-doped TiO_2, MO_x-doped TiO_2, and pure TiO_2 as target investigation (Kolinko and Kozlov, 2009). Ultimate products were nitrogen (N_2), nitrate ions (NO_3^-), and molecular water (i.e. water vapor) through the PCO of gaseous NH_3 (Yamazoe et al., 2008; Kolinko and Kozlov, 2009). The efficiency achieved was 71–100% (Pure TiO_2 (Yamazoe et al., 2008) (in terms of conversion percentage to N_2 (Kolinko and Kozlov, 2009))), 48–75% (M/TiO_2 (M: Pd, Pt, Au, Ag)) and 4–97% (MO_x/TiO_2 (Fe_2O_3, V_2O_5, MoO_3, CoO, NiO)) in terms of conversion to N_2 (Kolinko and Kozlov, 2009) (Table 2) with N_2 selectivity > 94% by the TiO_2 based photocatalyst (Yamazoe et al., 2008). However, pure TiO_2 generally had the best performance in terms of the rate of NH_3 PCO (68.5–80.4 ppm (NH_3)/min), which was much higher than those achieved by M/TiO_2 (27.6–49.8) or MO_x/TiO_2

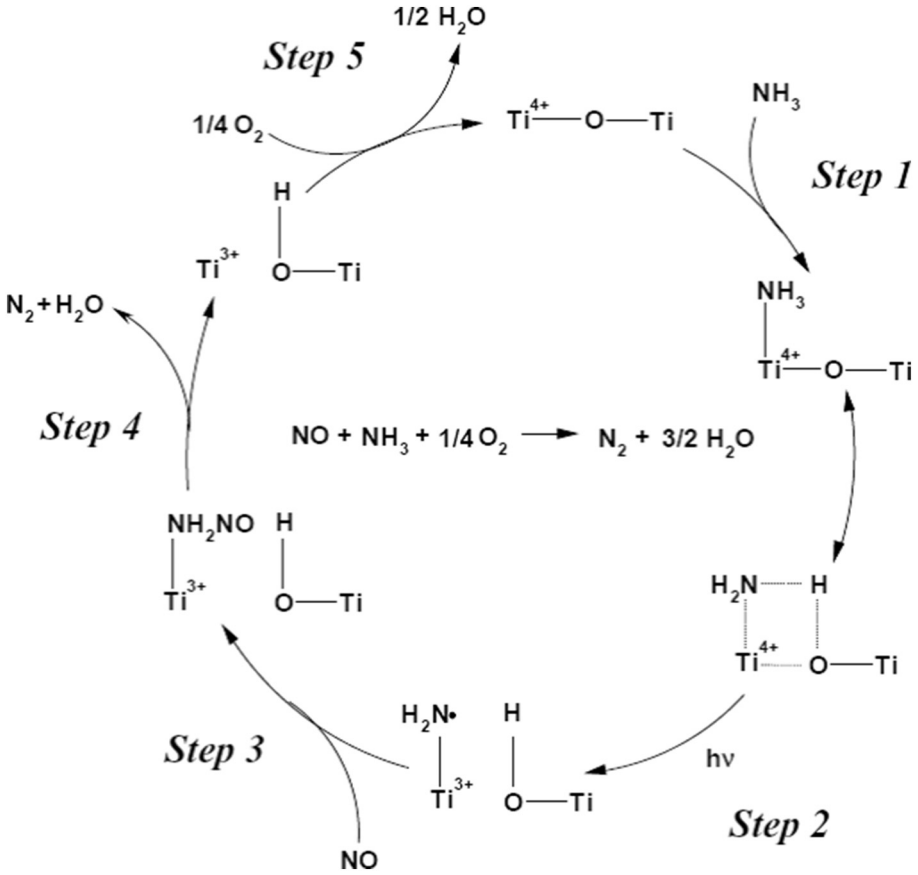

Fig. 13. Mechanism of TiO_2 catalyzed NH_3 PSCR (Teramura et al., 2004) (Reproduced with permission from Elsevier BV).

(2.9–39.8) in the same study (Kolinko and Kozlov, 2009). The cause of strong activity exhibited by pure TiO_2 was proposed to be the large surface available for the surface NO formation through the NH_3 PCO decomposition into N_2 (Yamazoe et al., 2008; Kolinko and Kozlov, 2009).

4.3. Degradation of sulphur family pollutants

Sulphur group pollutants, including SO_2 and H_2S which are generally produced from the combustion of fossil fuel from industrial boilers, internal combustion engines, and exhaust gas from landfill, sewage treatment plant or sewage from chemical plant in the river. They are regarded as the major cause of photochemical smog (Wang et al., 2016; Y.X. Liu et al., 2017; Y.X. Liu et al., 2018; Han et al., 2016; Yuan et al., 2012), acid rain (Wang et al., 2016; Y.X. Liu et al., 2017; Y.X. Liu et al., 2018; G.Y. Liu et al., 2018; Han et al., 2016; Yuan et al., 2012; Boyjoo et al., 2017), odor (Grzeskowiak et al., 2014; Alonso-Tellez et al., 2014; Kataoka et al., 2005; G.Y. Liu et al., 2018; Xu et al., 2014; Li et al., 2012; Boyjoo et al., 2017), fine particulates formation (PM2.5) (Wang et al., 2016; Y.X. Liu et al., 2017; Wang et al., 2017), and even global warming (G.Y. Liu et al., 2018). They can result in respiratory attack (Xu et al., 2014), bronchi constriction (Boyjoo et al., 2017), cardiovascular (Xu et al., 2014), asthma (Boyjoo et al., 2017), and nervous system attack (Xu et al., 2014), and are hazardous to health. This group of pollutants can also induce vegetation damage (Wang et al., 2017; Boyjoo et al., 2017), building facilities corrosion (Wang et al., 2017; Kataoka et al., 2005; G.Y. Liu et al., 2018; Boyjoo et al., 2017), and haze (Y.X. Liu et al., 2018; Wang et al., 2017), tropospheric ozone layer destruction (Yuan et al., 2012). As a result, removing them is important for air quality control. Photocatalytic decomposition of SO_2 and H_2S is one of the effective pathways. As oxygen was included in the simulated flue gas and it played an important role for either visible-light or UV-light driven SO_2 and H_2S decomposition which was similar to the conditions used in VOCs PCO degradation. As a result, these reactions were then classified as PCO reaction (Wang et al., 2017; Han et al., 2016; Yuan et al., 2012; Zhao et al., 2009; Zhao et al., 2008). One of the reasons for applying PCO in SO_2 and H_2S degradation was relatively low cost and energy saving properties (Wang et al., 2017). More important reasons behind include (i) the toxic intermediate of SO_2 produced throughout the gaseous H_2S photodecomposition would block the active site on the catalyst surface via adsorption (Wang et al., 2016), and adsorbed SO_2 would cause secondary pollution once it desorbed from the catalyst surface (Alonso-Tellez et al., 2014; Kataoka et al., 2005); and (ii) non gas-phase ultimate oxidation product of sulphate ion (SO_4^{2-}) and incomplete oxidation product of solid elemental sulphur (S) formed in the H_2S photodecomposition (Kataoka et al., 2005; Portela et al., 2007) and SO_2 photodecomposition (Wang et al., 2016) would block of active site of catalyst which results in the irreversible catalyst deactivation. In order to eliminate such drawbacks, use of UV-PCO with suitable photocatalyst mentioned above becomes the solution since this can be done by making use of strong oxidizing agent of hydroxyl radical generated from the chain reaction.

TiO_2 was commonly used for SO_2 and H_2S degradation. Since it was regarded as one of the most effective photocatalysts for the desulphurization from flue gas by its non-toxic, chemical stability (Wang et al., 2016). Large surface area provided by TiO_2 allowed the storage of poisoning sulphate and lowing the delaying the desorption of SO_2 (Alonso-Tellez et al., 2014). Reactivity of TiO_2 based photocatalysts involved in the sulphur family simulated pollutants with different light sources was summarized in Table 3. In the SO_2 group, most of the work involved the use of ordinary UV-light sources (Wang et al., 2017; Yuan et al., 2012; Zhao et al., 2009; Zhao et al., 2008), only few cases involving the use of visible-light as light source (Han et al., 2016). The SO_2 degradation efficiency achieved lied in the range of 33–98% for UV-light driven PCO reaction (Wang et al., 2017; Yuan et al., 2012; Zhao et al., 2009; Zhao et al., 2008) and 60% for visible-light driven PCO reaction (Han et al., 2016). Interestingly, most of the UV-assisted SO_2 degradation involved the use of pure TiO_2 as photocatalyst (Yuan et al., 2012; Zhao et al., 2009; Zhao et al., 2008), only rare cases involved the use of M-doped TiO_2 (Wang et al., 2017). While the catalyst used in visible-light driven reaction was multiple element doped TiO_2 (Han et al., 2016). The origin of reaction enhancement involving the use of foreign element doped TiO_2 was proposed to be the effective charge separation in the case of N-Zr-Ni tridoped TiO_2, CeTNs and CuTNs catalyst due to the narrow down of bandgap after the doping process according to the UV–Vis DRS characterization (Wang et al., 2017; Han et al., 2016). While those of pure TiO_2 in UV-PCO SO_2 degradation may be due to the large surface area provided by TiO_2 photocatalyst, no matter free-standing or supported on secondary materials (Yuan et al., 2012; Zhao et al., 2009; Zhao et al., 2008). Efficiencies of such reactions were also temperature, oxygen, and humidity sensitive in nature (Wang et al., 2017; Han et al., 2016; Yuan et al., 2012; Zhao et al., 2009; Zhao et al., 2008). In addition, all of these reactions were simultaneous reaction with NO_x photocatalytic decomposition in nature (Wang et al., 2017; Han et al., 2016; Yuan et al., 2012; Zhao et al., 2009; Zhao et al., 2008), where competitive adsorption between SO_2 and NO on the catalyst surface would be eventually taken place (Yuan et al., 2012). As a result, the presence of NO in optimum level became the key to success for the simultaneous NO and SO_2 PCO degradation in some of the studies (Wang et al., 2017; Yuan et al., 2012). Study carried out by Yuan's team showed that the presence of NO in SO_2 photodegradation would cause reduced removal efficiency of SO_2 (Yuan et al., 2012). Similar observation was recorded when SO_2 presented in the NO PCO degradation when the humidity, oxygen concentration in the flue gas were fixed (Yuan et al., 2012). However, another study carried out by Wang's group inversely showed that the presence of NO enhanced the PCO photodegradation of counterpart (SO_2) (Wang et al., 2017). Nature of ordinary PCO or so-called wet flue gas desulphurization (WFGD) (Yuan et al., 2012) and dry PCO (DPCO) or so-called dry flue gas desulphurization (DFGD) (Wang et al., 2017) in the above two studies may explain the difference in the observed results. This reflected from the difference in the setup shown in Figs. 14 and 15 (Wang et al., 2017; Yuan et al., 2012). From the mechanism of chain reaction in simultaneous NO_x/SO_2 degradation as shown below (Wang et al., 2017):

$$NO + O_2 \rightarrow NO_2 + O$$

$$NO + 2^{\cdot}OH \rightarrow NO_2 + H_2O_{(ads)}$$

$$NO_2 + SO_2 \rightarrow NO + SO_3$$

$$SO_3 + H_2O_{(ads)} \rightarrow H_2SO_{4(ads)}$$

$$SO_2 + O + H_2O_{(ads)} \rightarrow H_2SO_{4(ads)}$$

Since hydroxyl radical was the major participating species in the SO_2 and NO photodegradation based on the mechanism of the two species degradation, competition between SO_2, NO and hydroxyl radicals in the WFGD system would cause adverse effect to the counter part's degradation due to the coexistence of water in the flue gas (Yuan et al., 2012). However, such phenomenon reversely enhanced the simultaneous degradation of NO and SO_2 when DFGD was applied due to the use of water moisture removal device in the batch reactor (i.e. water vapor was removed, Fig. 15 (Wang et al., 2017)). The active oxygen species favored the formation of NO_2 and water molecule from NO in the dry SO_2 and NO mixture in cooperation with CeTN or CuTN photocatalyst (Wang et al., 2017). Consequently, the NO_2 generated favored the degradation of SO_2 into sulphuric acid via SO_3 formation, NO_2 was transformed back to NO for next round of SO_2 chain degradation (Wang et al., 2017).

Deactivation of TiO_2 photocatalyst in SO_2 degradation was also the research interest since it strongly affected the future application. This was shown from one of the investigations focused on the deactivation

Table 3
Photocatalytic activity of TiO_2 based materials in sulphur group pollutants decomposition.

Catalysts	Light source	Target	Efficiency (%)	Ref
CuTNs	UV-PCO	SO_2	32 (with BFG)	(Wang et al., 2017)
CeTNs	UV-PCO	SO_2	15 (with BFG)	(Wang et al., 2017)
N-Zr-Ni-TiO_2	Visible-light-PCO	SO_2	60	(Han et al., 2016)
TAS	UV-PCO	SO_2	33	(Yuan et al., 2012)
TiO_2	UV-PCO	SO_2	98	(Zhao et al., 2009)
TiO_2	UV-PCO	SO_2	98	(Zhao et al., 2008)
TiO_2/quartz wool	UV-A/visible-PCO	H_2S	50	(Grzeskowiak et al., 2014)
5 wt% WO_3/TiO_2 UV100	UV-A-PCO	H_2S	60	(Alonso-Tellez et al., 2014)
TiO_2	UV-PCO	H_2S	90	(Kataoka et al., 2005)
1 wt% Co-TiO_2	UV-PCO	H_2S	0.1	(G.Y. Liu et al., 2018)
1 wt% Cu-TiO_2	UV-PCO	H_2S	0.6	(G.Y. Liu et al., 2018)
1 wt% Ni-TiO_2	UV-PCO	H_2S	2.9	(G.Y. Liu et al., 2018)
1 wt% Mn-TiO_2	UV-PCO	H_2S	3.1	(G.Y. Liu et al., 2018)
TiO_2-nickel foam	UV (254 nm)	H_2S	39.1	(Li et al., 2012)
TiO_2-nickel foam	Ozone lamp (185 nm)	H_2S	97.4	(Li et al., 2012)
TiO_2-nickel foam	Black light (365 nm)	H_2S	33.1	(Li et al., 2012)
TiO_2-PET	UV-PCO	H_2S	30	(Portela et al., 2007)
T6	Visible-light	H_2S	N/A	(Bhirud et al., 2015)
TiO_2/glass fiber	UV-PCO	H_2S	99	(Brancher et al., 2016)
1 wt% Co-TiO_2	VUV-PCO	H_2S	76.9	(G.Y. Liu et al., 2018)
1 wt% Cu-TiO_2	VUV-PCO	H_2S	73.8	(G.Y. Liu et al., 2018)
1 wt% Ni-TiO_2	VUV-PCO	H_2S	71.3	(G.Y. Liu et al., 2018)
1 wt% Mn-TiO_2	VUV-PCO	H_2S	89.9	(G.Y. Liu et al., 2018)

characteristics of TiO_2 based catalyst in SO_2 degradation by both kinetic modelling and experiment carried out in a fixed bed reactor (Wang et al., 2016). The fitted results of computational kinetic model and experimental operation showed that performance depreciation of TiO_2 photocatalyst in SO_2 photodegradation was related to water content (humidity) in the flue gas (Wang et al., 2016). The main reason for this phenomenon was the water adsorbed on TiO_2 catalyst surface may inversely inhibit the formation of active oxygen or hydroxyl radicals when the water content in the flue gas was higher than optimum value as indicated from both computational and experimental results. Such finding may also explain the difference in the desulphurization efficiency between DFGD and WFGD mentioned previously as the SO_2 removal efficiency was the best at 0% humidity, and it was reduced when humidity increased from 0 to 4% in Wang's study due to the competitive adsorption between SO_2 and water vapor (Wang et al., 2017). As a result, the application of DFGD with careful control of flue gas humidity may be the best way to prevent the catalytic deactivation in order to achieve effective photocatalytic SO_2 removal from flue gas.

Same as SO_2 photodecomposition, use of PCO technology was the mainstream in the TiO_2 nanomaterials catalyzed gaseous H_2S photodecomposition (Grzeskowiak et al., 2014; Alonso-Tellez et al., 2014; Kataoka et al., 2005; G.Y. Liu et al., 2018; Li et al., 2012; Portela et al., 2007; Brancher et al., 2016). The reaction mechanism was illustrated as below (Li et al., 2012):

$$TiO_2 + h\upsilon \rightarrow h^+ + e^-$$

$$h^+ + H_2O \rightarrow {}^{\cdot}OH + H^+$$

$$O_3 + e^- \rightarrow O_3^{-\cdot}$$

$$H^+ + {}^{\cdot}O_3^- \rightarrow HO_3^{\cdot}$$

$$HO_3^{\cdot} \rightarrow O_2 + {}^{\cdot}OH$$

$$O_3 + h\upsilon(\lambda < 310\ nm) \rightarrow O^{\cdot} + O_2$$

$${}^{\cdot}O + H_2O \rightarrow 2{}^{\cdot}OH$$

$$h^+ + OH^- \rightarrow {}^{\cdot}OH$$

$$O_2 + 2H^+ + 2e^- \rightarrow H_2O_2$$

$$H_2S + 2{}^{\cdot}OH \rightarrow S\downarrow + 2H_2O \text{ (Incomplete oxidation 1)}$$

$$H_2S + 8{}^{\cdot}OH \rightarrow SO_4^{2-} + 2H^+ + 4H_2O$$

$$H_2S + H_2O_2 \rightarrow S\downarrow + 2H_2O \text{ (Incomplete oxidation 2)}$$

$$H_2S + 4H_2O_2 \rightarrow SO_4^{2-} + 2H^+ + 4H_2O$$

Up to date, most of the H_2S removal research involved the use of UV lamp as light source in the PCO process, which showed strong efficiency in the H_2S removal with a range of 30–99% achieved by pure TiO_2 based photocatalyst as listed in Table 3 (Grzeskowiak et al., 2014; Alonso-Tellez et al., 2014; Kataoka et al., 2005; Li et al., 2012; Portela et al., 2007; Brancher et al., 2016). In contrast, even though foreign materials loaded TiO_2 (i.e. Co-TiO_2, Pd-TiO_2, Pt-TiO_2, and Au-TiO_2) showed superior activity in UV-PCO assisted VOCs degradation (51.5–68.8%, Table 1), the efficiency of UV-PCO assisted H_2S degradation achieved by M-doped TiO_2 was only 0.1–3.1% as illustrated

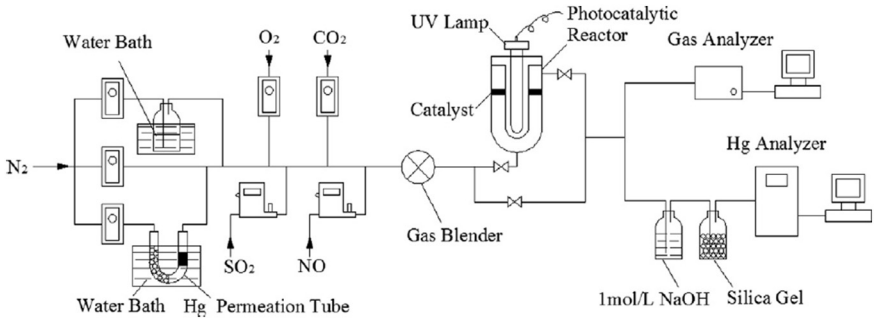

Fig. 14. Schematic diagram of the experimental system (WFGD) (Yuan et al., 2012) (Reproduced with permission from Elsevier BV).

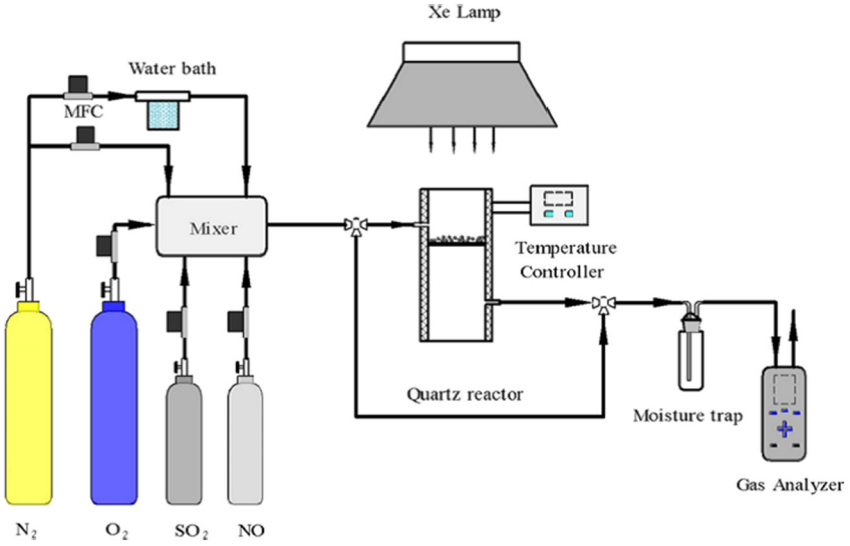

Fig. 15. Schematic diagram of the SO_2 oxidation fixed bed system (DFGD) (Wang et al., 2017) (Reproduced with permission from ACS).

in Table 3. This value was even smaller than that achieved by pure TiO_2 in the same reaction (G.Y. Liu et al., 2018). The possible reason for the strong difference between pure TiO_2 and M-doped TiO_2 in the UV-PCO assisted H_2S photodegradation may be due to the surface area available on the pure TiO_2 was much larger than that of M-doped TiO_2. This may unfavored the adsorption of H_2S and the e^-/h^+ pairs separation on the M-doped TiO_2 under ordinary UV condition (G.Y. Liu et al., 2018). Compared to the majority of UV-catalyzed H_2S reaction, there was an only exception of H_2S degradation, which was carried out in aqueous media by Bhirud's team (Bhirud et al., 2015). H_2S gas was pumped into aqueous sodium hydroxide solution, and the reaction was carried out under visible-light irradiation with N-doped TiO_2/graphene (N-TiO_2/Gr) as photocatalyst. The result showed that N-TiO_2/Gr with 2% loading of graphene achieved the best activity in terms of the hydrogen evolution with an amount of ~41,000 μmol H_2 produced from the H_2S/NaOH solution under visible-light irradiation (Bhirud et al., 2015). Possible reason for such strong activity throughout the H_2S splitting process achieved was the effect e^-/h^+ pairs separation due to the bandgap reduction after the hybridization between N-TiO_2 and graphene nanosheets (Bhirud et al., 2015).

Based on the successful experience on the application of VUV assisted PCO reaction for VOCs degradation, such technology was then applied to H_2S photodegradation (G.Y. Liu et al., 2018). Up to date, M-doped TiO_2 exhibited strong activity in the demonstration of H_2S degradation via VUV-PCO reaction. Compared to identical PCO reaction operated by ordinary UV-light source, H_2S degradation efficiency was sharply elevated to the range of 71.3–89.9% when compared to that of UV-PCO catalyzed by identical group of photocatalysts (i.e. Co-TiO_2, Cu-TiO_2, Ni-TiO_2, Mn-TiO_2) as listed in Table 3 (G.Y. Liu et al., 2018). The origin for the obvious enhancement of H_2S removal efficiency was proposed to be (i) effective removal of the residual ozone throughout the chain reaction of H_2S degradation; and (ii) the reduction of bandgap to the visible-light range after the doping process (G.Y. Liu et al., 2018).

Since the effectiveness of H_2S removal was controlled by key factors including the H_2S concentration, humidity of the system and UV light wavelength (Grzeskowiak et al., 2014), especially the factors of humidity and H_2S concentration were the potential reasons for deactivation of TiO_2 photocatalyst throughout the H_2S photodegradation. In addition, by-products of SO_2 and elemental S would also deactivate the TiO_2 catalyst via adsorption on active site on the TiO_2 surface mentioned previously (Kataoka et al., 2005; Portela et al., 2007). As a result, careful control of the initial H_2S concentration and the humidity of the H_2S flue gas became the possible way to prevent from the TiO_2 catalyst deactivation.

Similar to the case of VOCs activity research, application development on the reaction simulator level was also very few compared to huge efforts on the batch experiment level. Li et al. (2012) developed a reaction simulator for H_2S removal, as shown in Fig. 16. The system with TiO_2-nickel foam catalyst showed the best H_2S removal performance in the simulator equipped with ozone lamp (185 nm), which is

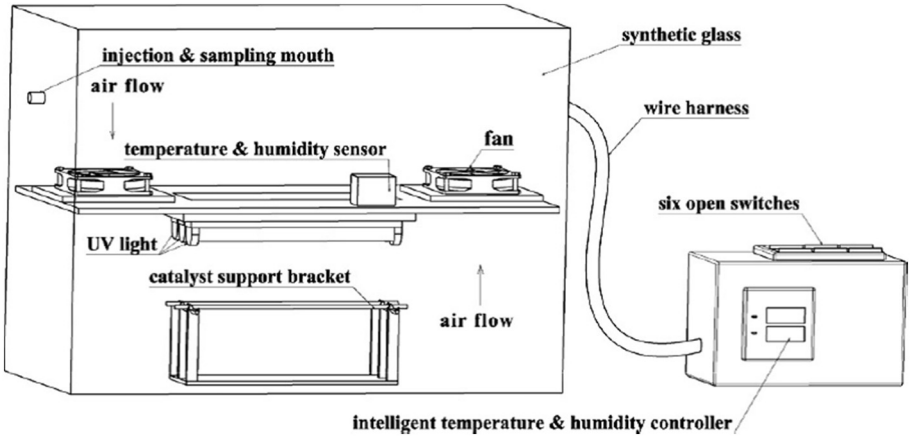

Fig. 16. Scheme of the experimental apparatus utilized for H_2S degradation (Li et al., 2012) (Reproduced with permission from Elsevier BV).

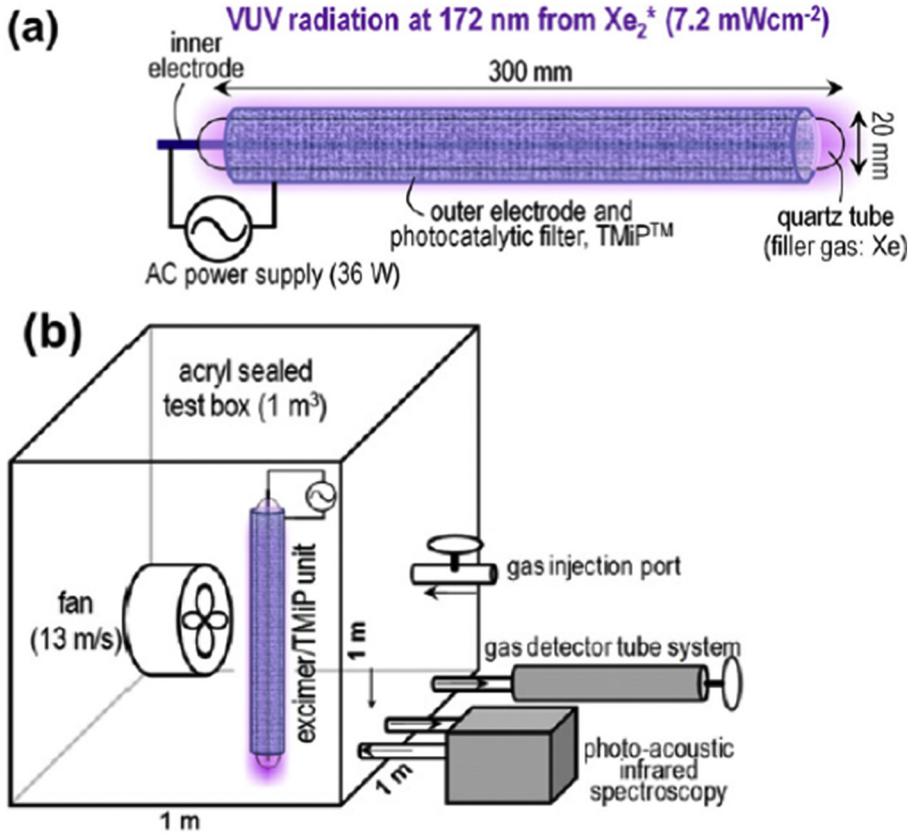

Fig. 17. Schematic illustrations of (a) the photocatalyst-excimer-lamp unit (excimer/TMiP unit). (b) The test method for evaluation of air-purification ability of the unit (Ochiai et al., 2013) (Reproduced with permission from Elsevier BV).

revealed by the high removal percentage (97.4%) as illustrated in Table 3 (Li et al., 2012).

4.4. Application in appliance scale and multi-pollutant treatment

Besides the TiO_2 based photocatalysis studies for air pollutant degradation in air cleaner simulator scale as described previously (Zhong et al., 2013; Farhanian and Haghighat, 2014; Wongaree et al., 2016; Mull et al., 2017), demonstration on the capability of TiO_2 photocatalyst equipped with a specific light source for air pollutant degradation was also carried out (Ochiai et al., 2013). VUV lamp with TiO_2 coated titanium mesh filter (excimer/TMiP) for hybrid environment purification unit developed by Ochiai's group was selected as representative (Ochiai et al., 2013). Design of the filter equipped VUV lamp for indoor air purification was shown in Fig. 17 (Ochiai et al., 2013). The result showed that the excimer/TMiP UVU lamp exhibited extremely strong activity in the gaseous acetaldehyde decomposition within 1.5 h as compared with other UV and VUV sources (Ochiai et al., 2013).

Sometimes TiO_2 based photocatalysts were employed for the simultaneous removal of multiple air pollutants in a single operation (Yuan et al., 2012). A representative was the TiO_2-aluminum silicate fiber (TAS) developed for simultaneous removal of NO, SO_2 and mercury ion (Hg^{2+}) in the flue gas sample. The TAS equipped batch reactor showed that the removal performance of SO_2 and NO was enhanced in the presence of Hg^{2+} in the flue gas under a UV source. This demonstrated the potential of using TiO_2 based photocatalysts for simultaneous removal of multiple air pollutants in the future (Yuan et al., 2012). Another work carried out by Huang et al. (2011) demonstrated that toluene degradation and air disinfection can both be achieved in a honeycomb type PCO reactor with TiO_2/γ-Al_2O_3/NF, as shown in Fig. 18. High toluene removal efficiency of 82% was achieved and *E. coli* could be completely inactivated within 5 min (Huang et al., 2011). This showed that the TiO_2 based filter can be further developed for air disinfection and cleaning dual-purpose in future.

4.5. Photocatalyst deactivation

Even though TiO_2 has been widely used as a practical photocatalyst for VOCs purification and many methods have been developed to modify its photocatalytic activity, the problem of photocatalyst deactivation is an important issue in application. Accumulation of recalcitrant reaction intermediates on the photocatalyst surface ascribed to be one of the reasons for deactivation. Sun et al. (2012) have investigated the photocatalytic degradation of gaseous toluene on Fe-TiO_2 under visible-light irradiation in a batch reactor with consecutive runs. Results showed that the photocatalytic activity of Fe-TiO_2 was partially depreciated after 20 consecutive reaction runs. They pointed out that the reason of deactivation can be attributed to the formation of stable intermediates, such as benzaldehyde and benzoic acid, which occupied the active sites on the photocatalyst surface as indicated in in-situ DRIFTS experiment. However, the deactivated photocatalyst could be regenerated completely after they removed the adsorbed benzaldehyde and benzoic acid with heat treatment at 653 K for 3 h, as shown in Fig. 19 (Sun et al., 2012). Abbas et al. (2011) studied the deactivation of optimized titania nanoparticles (TNPs) used as photo-catalyst for the abatement of mixtures of important VOCs including ethylene, propylene, and toluene. They observed the deactivation behavior of the TNPs treated with a mixture of VOCs through FT-IR investigation, together with a comparison of the individual gases and the fresh catalyst. The result is shown in Table 4. Different by-products adsorbed on the active sites of the photocatalysts, such as polyethylene/polypropylene, aldehydes, carboxylic acids, alcohols and adsorbed toluene itself were found to be responsible for the deactivation of the photocatalysts.

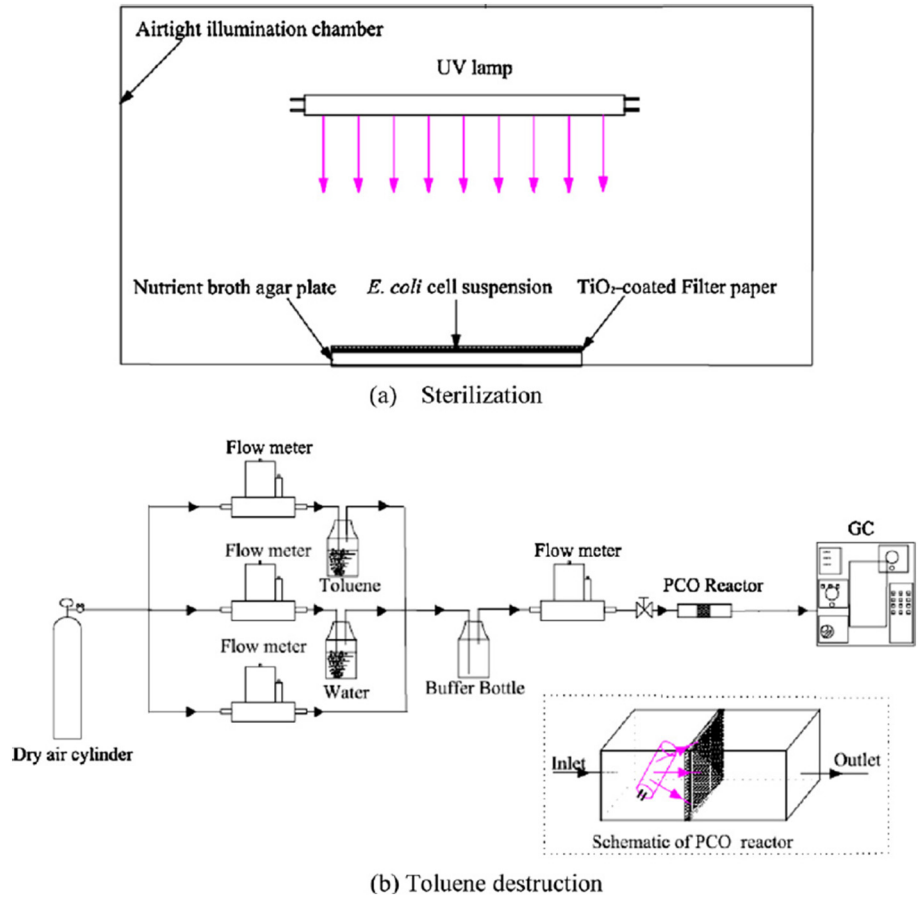

Fig. 18. Experimental setup: (a) sterilization; (b) toluene destruction (Huang et al., 2011) (Reproduced with permission from Elsevier BV).

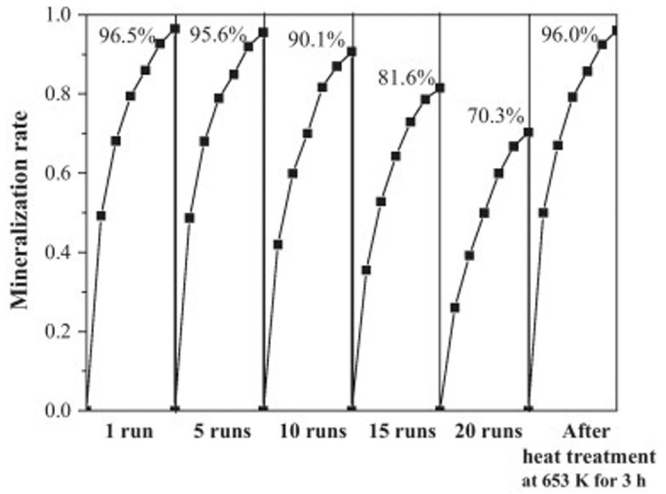

Fig. 19. Stability test of 0.7% Fe-TiO_2 for repeated photocatalytic degradation of toluene under visible-light irradiation ($\lambda > 400$ nm). The initial concentration of toluene is 370 ppm; the R.H. condition is 60% (Sun et al., 2012) (Reproduced with permission from Elsevier BV).

Most of the experiments mentioned above were performed using batch-type reactor, they usually need a long time for the complete mineralization of the target pollutants. In practical photocatalytic degradation of VOCs, the ideal reaction time should be as short as possible. Thus photocatalytic degradation performed on real effluents has to be investigated under dynamic condition which is the best way to mimic real VOCs treatment systems with short reaction time. Thevenet et al. (2014) have investigated the photocatalytic oxidation of acetylene using a continuous flow reactor. The photocatalyst consisted of P25 (Degussa) nanoparticles deposited on glass fibers. The result showed a saturation of intermediate organic acids such as formic, oxalic and acetic acids on the photocatalyst surface, causing deactivation. Finally, > 80% of the adsorbed acids can be removed and converted into CO_2 under synthetic air so that the photocatalytic regeneration of the saturated surface can be efficiently achieved. What's more, this approach allowed the photocatalyst perform well, ensuring mineralization of 85% of the acetylene with short contact time. Similar phenomenon was also observed in the pure TiO_2 catalyzed NH_3 PCO reaction carried out by Kolinko's team (Kolinko and Kozlov, 2009), which is reflected from the increased time taken for achieving 100% NH_3 conversion level from 50 to 100 min in 5 repeated operations. The possible reason was due to the TiO_2 deactivation caused by the NO_3^- accumulated on the active surface of TiO_2 during each successive run (Kolinko and Kozlov, 2009).

In order to regenerate the deactivated photocatalyst, many methods have been reported in the literature. These not only include the above mentioned methods (i.e. heat treatment (Sun et al., 2012) and synthetic air (Thevenet et al., 2014)), but also include many other methods, such as the use of basifying agents like NaOH (Tuprakay and Liengcharensit, 2005) or NH_4OH (Rosso et al., 2001), UV irradiation (Prieto et al., 2007), washing (Jing et al., 2004) and oxidation with H_2O_2 combined with UV irradiation (Miranda-Garcia et al., 2014) etc.

Sometimes the deactivation of catalyst was not caused by the simulated pollutant. This was shown from one of the investigations focused on the deactivation characteristics of TiO_2 based catalyst in SO_2 degradation by both kinetic modelling and experiment carried out in a fixed bed reactor (Wang et al., 2016). The fitted results of computational kinetic model and experimental operation showed that performance depreciation of TiO_2 photocatalyst in SO_2 photodegradation was

Table 4
Comparison table of the different groups present on titania (Abbas et al., 2011) (Reproduced with permission from Elsevier BV).

Compounds detected by FT-IR for TNP	FT-IR frequencies for different compounds (cm^{-1})	Unused catalyst	Used with individual gases	Used with mixture of gases
Long chain alkanes	1220	No	Present	No
Aromatic aldehydes	1352	No	No	Present
Alcohols	1440	No	Present	Present
OH groups from water	1640	Yes	Reduced	Reduced
Carbon dioxide	2345	Yes	Yes	Yes
Aldehydes	1690,2875	No	Present	Present
Epoxide	3054	No	Present	Present
Toluene	1690,3250	No	Only present in toluene test	Present
Carboxylic acids attached with OH groups	3400	No	Present	Present

related to water content (humidity) in the flue gas (Wang et al., 2016). The main reason for this phenomenon was the water adsorbed on TiO_2 catalyst surface may inversely inhibit the formation of active oxygen or hydroxyl radicals when the water content in the flue gas was higher than optimum value as indicated from both computational and experimental results. Computation modelling and experimental results were highly matched with each other (Wang et al., 2016) which proved and explained the main origin of the TiO_2 deactivation in SO_2 degradation (Wang et al., 2016). Another study carried out by Han's team involving the use of N-Zr-Ni tridoped TiO_2 showed that its activity was also depreciated when reaction temperature increased to higher than the optimum value which would reduce the physical adsorption ability of photocatalyst and finally cause activity reduction (Han et al., 2016). Similar phenomenon was also observed from VOCs photodegradation. In one of the studies carried out by Zhang's group, they observed that the toluene removal efficiency was strongly affected by relative humidity throughout the TiO_2 catalyzed photocatalytic toluene degradation under UV-light (Zhang et al., 2004). The maximum toluene removal efficiency (40%) was achieved at a humidity of 24%, activity was depreciated when the humidity was out of 24% and varied strongly (Zhang et al., 2004).

Not only intermediates or reaction environment can cause photocatalytic deactivation, many other factors can also cause activity depreciation. Dolat et al. (2012) chose a one-step, hydrothermal method to synthesize the nitrogen-carbon co-doped titanium dioxide (N,C-TiO_2) photocatalysts. Ammonia and alcohols with different chain lengths (methanol, ethanol, isopropanol, 1-butanol, 2-butanol, tert-butanol) were used as nitrogen and carbon dopant precursors, respectively. Under the same experimental condition, the N,C-TiO_2 prepared from 2-butanol, and 1-butanol as carbon precursor exhibited much stronger resistance to deactivation during multiple cycles compared to pristine TiO_2 and commercial Degussa P25 photocatalysts. Additionally, Fresno et al. (2008) have researched the influence of the heteroatom distribution on deactivation through the photocatalytic degradation of toluene by doped and coupled (Ti, M)O_2 (M = Sn or Zr) nanocrystalline oxides. The coupled photocatalysts have been proved to have a higher degradation rate due to the absence of the deactivation process. The lack of deactivation is attributed to a lower accumulation of adsorbed intermediates during the photocatalytic reaction for the coupled catalysts, as shown by the DRIFT spectra and solid-liquid extraction of the used catalysts. They further pointed out that the resistance to deactivation of the coupled photocatalysts observed in toluene PCO is mainly due to more accessible adsorbed water formed, due to the presence of the second oxide, that increase the capacity for the removal of adsorbed reaction intermediates. In addition, dopant itself may be the sources of activity depreciation. Such as iron in Fe-TiO_2 synthesized by Yang's group (Yang et al., 2015), its activity under UV-light for the same BTEX removal reaction was relatively worse than pure TiO_2, possible reason for this was because of the Fe was acted as the recombination centre under the UV-light source (Yang et al., 2015). More strange case was that, from the Pd-TiO_2, Pt-TiO_2, and Au-TiO_2 synthesized by Fu's group for formaldehyde decomposition, minimum activity was achieved by Pd-TiO_2 among the three photocatalysts under different types of light sources (Fu et al., 2012). The most possible reason for this was the formation of palladium oxide converted from the Pd-TiO_2 which resulted in the depreciation in PCO VOCs degradation (Fu et al., 2012). Treatment temperature may also cause reduction in activity, such as N-doped TiO_2 synthesized by Tryba's team (Tryba et al., 2018). Its activity in both UV and visible-light assisted reaction was depreciated when the treatment temperature was out of the optimum value (300 °C) during the synthesis. The possible reason for this was both dual bandgap observed in N-T300 together with the large specific surface area for acetaldehyde decomposition (Tryba et al., 2018).

Even though the chemically modified TiO_2 catalyst can be developed with different dopant concentrations, different structures of pure TiO_2 catalyst, or use of support materials with different support concentrations, photocatalytic activity depreciation would still be taken place with different aspects. In the aspect of activity associated with the amount of the supporting materials for TiO_2, especially the graphene and g-C_3N_4 supports, its activity will be depreciated when amount of TiO_2 and graphene (Andryushina and Stroyuk, 2014; Ebrahimi and Fatemi, 2017; Wang et al., 2012; Jo and Kang, 2013; Mull et al., 2017), g-C_3N_4 (Ma et al., 2016; Y.H. Li et al., 2017; Song et al., 2016; Reli et al., 2016; Koci et al., 2017; Yu et al., 2013; Munoz-Batista et al., 2014), or CNT (Wongaree et al., 2016) used was out of the optimum value. This can also be related to the structure of the graphene nanostructure used (Andryushina and Stroyuk, 2014; Roso et al., 2017). Such phenomenon may result from (i) the recombination of e^-/h^+ pairs throughout the charge transfer (Wang et al., 2012), or excessive amount TiO_2 loaded on the carbon support surface will act as the e^-/h^+ pairs recombination centre (Yu et al., 2013); (ii) excessive absorbance with scattering by GO support (Jo and Kang, 2013) or excessive amount of g-C_3N_4 (Y.H. Li et al., 2017), which inhibited the irradiation of light to TiO_2 loaded on the composite surface; or (iii) the blockage of the active surface against effective light irradiation (Roso et al., 2017; Ebrahimi and Fatemi, 2017) or shielding effect exhibited by the excessive carbon support which inhibited the light reaching TiO_2 surface (Yu et al., 2013). While in the case of dopant loading level, photocatalytic activity would be depreciated when the loading was out of optimum level. For example, when the Co loading in Co-TiO_2 was out of the optimum level (1 wt% Co), overall 185 nm-PCO activity was depreciated from Huang's experiments (Huang et al., 2013). Even though 5 wt% Co-TiO_2 exhibited maximum benzene removal percentage in 185 nm-PCO reaction, the residual ozone removal at the outlet was not as strong as that achieved by 1 wt% Co-TiO_2 (Huang et al., 2013). As a result, overall activity was still regarded as depreciated by comparing 5 wt% and 1 wt % Co-TiO_2 photocatalyst (Huang et al., 2013). It means the loading content of dopant in the resulting chemically modified TiO_2 was the key factor. Even though the loading level of dopant was low (< 1 wt%) in the chemically modified TiO_2 photocatalyst, their activity depreciation compared to the pure TiO_2 may be due to the direct blocking of the active surface area for the adsorption of target pollutant. Such phenomenon was obvious in the case of NH_3 adsorption during NH_3 PCO as an example (Kolinko and Kozlov, 2009). Thickness of the chemically

modified TiO_2 film on substrate surface may also affect their activity under visible-light, the main reason seems to be contributed from the agglomerated and flocculated N-TiO_2 particles on the film surface when the thickness was 9.26 μm (1 wt% N-TiO_2) which inhibited the visible-light penetrate to the film surface (Kannangara et al., 2018).

Generally speaking, we are optimistic to believe that through continued efforts of researches, the phenomenon of photocatalytic deactivation can be effectively controlled and resolved.

5. Other semiconductor oxides based photocatalyst

Due to the drawbacks of the titania family as VOCs photocatalysts mentioned in previous sections, alternative materials for overcoming such problems become the focus recently. Number of sulphides, nitrides, and oxynitrides (CdS, Ta_3N_5, and TaON are among the most promising examples) have been investigated as alternative materials for visible-light or solar photocatalysis (Osterloh, 2008), but owing to the drawback of some of the visible-light catalysts (such as toxicity of CdS), these photocatalysts cannot become the alternative of TiO_2. As a result, exploiting complex metal oxides as novel photocatalytic materials have been made during the last decade with huge efforts. These materials include niobates, tantalates (TiO_3^{2-}), vanadates (VO_4^{2-}) and germanates, which contained the cations of d^0 or d^{10} electronic configurations such as In^{3+}, Ga^{3+}, Sb^{5+}, Bi^{5+}, and Ag^+ (Zou et al., 2001; Ouyang et al., 2009a; Ouyang et al., 2009b; Li et al., 2008; Ouyang et al., 2006; Tang et al., 2004a; Ye et al., 2003; Zou et al., 2002a; Zou et al., 2002b; Zou et al., 2002c; Ye et al., 2002; Kako et al., 2007). These novel semiconductors have proved to be among the most successful photocatalysts. For example, $NiO_x/In_{1-x}Ni_xTaO_4$ was the first material found to catalyze overall water photolysis under visible-light irradiation (Zou et al., 2001).

ZnO is the commonest alternative to TiO_2 in semiconductor photocatalysis (Poulios and Tsachpinis, 1999; Poulios et al., 2000), with a similar energy bandgap (E_g = 3.3 eV) (Kaidashev et al., 2003), low-cost and non-toxicity. It can be prepared in a variety of forms and structures and it has comparable photocatalytic activity to TiO_2, but is known to be a photo-corroding material (Georgieva et al., 2012). Even though it has such weakness, the use of ZnO based photocatalyst for air pollutant (VOCs) removal was also active after loading to nanomaterial support like graphene, as it eliminated the problem of e^-/h^+ pair recombination (Y-C. Chen et al., 2015). Y-C. Chen et al. (2015) studied the decomposition of gaseous acetaldehyde into CO_2 with different loadings of ZnO in ZnO/Graphene (ZG) under UV-light source. Overall activity of ZG was better than pure ZnO with the optimum GO content of 3 wt%, which decomposed all the acetaldehyde within 1 h (Y-C. Chen et al., 2015). Another way to eliminate such problems was the use of metal modified ZnO like Ag/ZnO developed by Nagaraju's group (Nagaraju et al., 2017). This material showed red shift in the bandgap from 3.29 eV in pure ZnO to 3.19 eV, which was resulted from the mix up of crystal structure between Ag and ZnO (Nagaraju et al., 2017). Such red shifting enhanced the visible-light photocatalytic activity, as is reflected from the high efficiency of methylene blue (MB) decomposition under visible-light (45 min) against the pure ZnO (90 min) to achieve 100% MB decomposition (Nagaraju et al., 2017).

Cu_2O (and CuO) is a p-type semiconductor with band-gap energy of 1.8–2.5 eV (1.21–2.00 eV for CuO) (Minami et al., 2004; Ogwu et al., 2005) that absorbs visible-light and is abundant in nature. (Note that Cu_2O can also be prepared as an n-type semiconductor, though with more effort.) Although it is mainly used in solar cells, applications in organics photo-oxidation have also appeared in the literature (L. Huang et al., 2009; Kakuta and Abe, 2009; Chu et al., 2011).

Another demonstrated TiO_2 alternative was MnO_x supported on carbon (MnO_x/C) developed by Zhou et al. (2018), MnO_2/C showed excellent activity in the visible-light driven gas phase VOCs (toluene) removal. The ε-MnO_2/0.45-C synthesized from 8 mL $Mn(NO_3)_2$/0.45 g glucose mixture solution exhibited strong visible-light absorption at the range of 850–900 nm from DRS analysis, and achieved the highest catalytic toluene removal efficiency of 87.4% in 70 min gas phase operation under visible-light (Zhou et al., 2018).

Besides d-block metal oxides, other semiconductor oxides were also drawn attention recently. One example is Bi_2O_3 which can be either of a p- or n-type (Metikoshukovic, 1981). With a bandgap of 2.8 eV, it exhibits visible-light activity too and it is mainly used in combination with other semiconductors (Park et al., 1994; Li et al., 2011; Myung et al., 2011). There are also many single phase mixed oxides with semiconducting properties, of which strontium titanate, $SrTiO_3$ (see for example (Miyauchi et al., 2000; Zhang et al., 2010)) and bismuth vanadate, $BiVO_4$, (see for example (Myung et al., 2011; Chatchai et al., 2010; Long et al., 2006)) are the most characteristic examples. $SrTiO_3$ has the same energy bandgap as TiO_2 (3.2 eV (Kung et al., 1977)) and (similar to TiO_2 and ZnO) can be used alone as an efficient photocatalyst for organics electrooxidation since its valence and conduction bands are at energy levels, able to produce OH radicals from water oxidation and superoxide radicals by oxygen reduction (Lianos, 2011). On the other hand, $BiVO_4$ (with a bandgap of 2.8 eV (Myung et al., 2011)) is mainly used as a visible-active additive to other semiconductors (Myung et al., 2011; Chatchai et al., 2010; Long et al., 2006). $BiVO_4$ has been found to show excellent visible-light driven photocatalytic activity for water splitting and for the degradation of organic contaminants (Liu et al., 2009; Zhou et al., 2006; Kudo et al., 1998). Fig. 20 shows the XRD pattern and FE-SEM image of $BiVO_4$ nanosheets (Zhang et al., 2006).

Other semiconducting oxides containing bismuth with narrow bandgap, such as Bi_2WO_6 (Zhuo et al., 2013; Zhang et al., 2009), and

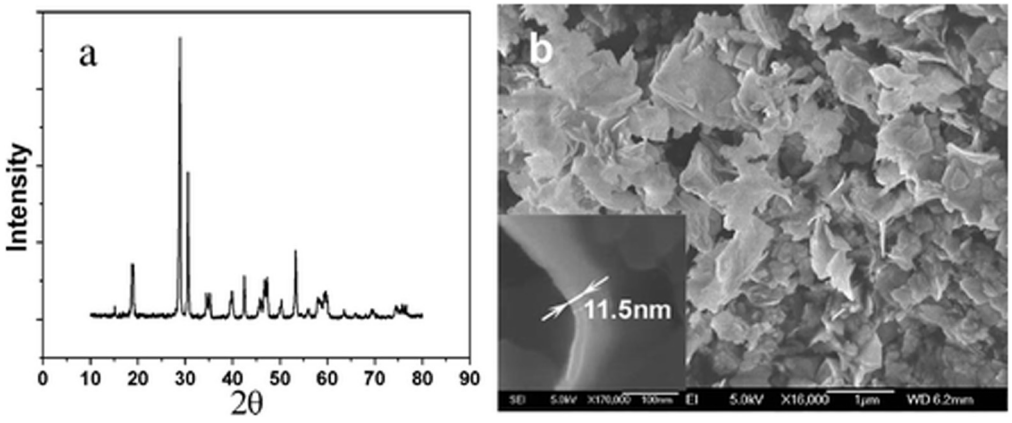

Fig. 20. XRD pattern (a) and FE-SEM image (b) of $BiVO_4$ nanosheets. The inset in b is a single nanosheet standing on edge (Zhang et al., 2006) (Reproduced with permission from ACS).

Bi_2MoO_6 (Tian et al., 2013) have received intensive interest by the same reason of their visible-light driven photocatalytic activities. Tang et al., 2004b reported that Bi_2WO_6 could degrade organic compound under visible-light irradiation.

6. Conclusion and forecast

In this review, background of using TiO_2 family based photocatalyst, and its variations for activity enhancement was introduced and discussed. The topics covered the degradation of VOCs, NO_x, SO_2, H_2S for indoor air quality improvement, odorous gas removal, and atmospheric pollutant degradation by different photocatalytic techniques developed in past decades. The factors of TiO_2 based photocatalyst's activity depreciation and brief discussion on the TiO_2 alternatives were also reviewed.

Nowadays as the number of publications on photocatalysis has increased exponentially, and people have a deep understanding of photocatalysis, here we have our mind for future exploration. First of all, among all investigated TiO_2 based materials catalyzed photocatalytic air pollutant removal works up to date, UV or VUV light ($\lambda < 400$ nm) induced one was still the majority group. While visible-light ($\lambda \geq 400$ nm) induced reaction only occupied a small portion. In order to make TiO_2 active under visible-light, various kinds of dopant were applied in the synthesis. The use of appropriate supporting materials seems to be alternatives. Even though their visible-light catalytic activity can be enhanced, its application value was still limited due to the fact that such materials cannot be used directly as the bulk sample are in powder form, or required to be fabricated on a secondary substrate for equipping in the reactor. Secondly, most of the works on air pollutant removal area were still at the batch reactor level with only few examples of simulator device level. This cannot reflect the actual value of the TiO_2 based photocatalyst for the real commercially available device. Consequently, their future development will still be limited, i.e. it is hard to break through from the batch research level.

Recently, the development of 3D structured nanoporous materials as TiO_2 support becomes a new alternative, such as graphene aerogel (Chen et al., 2018; Nawaz et al., 2017). Since graphene aerogel based materials can be used directly due to its free-standing nature after the hydrothermal synthesis and showed strong activity in the catalytic reaction under visible-light (Chen et al., 2018; Nawaz et al., 2017). However, their application was still limited in aqueous media reactions up to date (Chen et al., 2018; Nawaz et al., 2017). As a result, by making use of the superior VOCs removal ability of 2D TiO_2 loaded graphene, there is room for the further development of TiO_2 loaded graphene aerogel in gas phase air pollutant removal research.

In order to deal with the bottleneck situation, the use of free-standing TiO_2 based 3D catalyst like TiO_2 loaded graphene aerogel or other free-standing macroporous supports can be the solution. In addition, the use of such materials should also be merged with commercial air cleaner system for the evaluation of their actual value in the air purification or even the disinfection for the IAQ improvement. All listing above may constitute series of objectives for future research in photocatalysis.

Abbreviations

SCR	selective catalytic reduction
VOCs	volatile organic compounds
BTEX	monoaromatic hydrocarbons (benzene, toluene, ethyl benzene, xylene)
THAc-15	TiO_2 nanocrystals synthesized in 15 M acetic acid
$THNO_3$-0.75	TiO_2 nanocrystals synthesized in 0.75 M nitric acid
TNS-F	TiO_2 nanosheets synthesized in presence of hydrofluoric acid
TMiP	TiO_2 nanoparticles-modified Ti mesh sheet
MA	micropore-anatase TiO_2 composite
MEK	methyl ethyl ketone
PAN/GO + TiO_2	TiO_2 loaded graphene oxide on polyacrylonitrile
T400	mesoporous TiO_2 calcinated at 400 °C
N-T300	N-TiO_2 calcinated at 300 °C
T6	N-TiO_2/(2%)Gr containing 2% graphene in the N-doped TiO_2/Gr composite
g + TiO_2/N, C-300-20%	N,C codoped 20% TiO_2 on gypsum support
g-C_3N_4	graphitic carbon nitrile
S15	CN QDs-rTiO_2 with CN QDs:rTiO_2 ratio of 0.15:1
CT10	g-C_3N_4/TiO_2 with 10 wt% g-C_3N_4
U100	g-C_3N_4-TiO_2 synthesized from urea/P25 with weight ratio (wt%) = 100:1
M400	g-C_3N_4-TiO_2 synthesized from melamine/P25 with weight ratio (wt%) = 400:1
MWCNT	multiwall carbon nanotubes
TAS	TiO_2 supported on aluminum silicate
TIFF-TiO_2	TiO_2 synthesized from titanium isopropoxide
CuTN	copper doped titania based nanofiber
CeTN	cerium doped titania based nanofiber
Ag($h\upsilon$)/TiO_2	Ag/TiO_2 synthesized by photoreduction
Au($h\upsilon$)/TiO_2	Au/TiO_2 synthesized by photoreduction
Ag($NaBH_4$)/TiO_2	Ag/TiO_2 synthesized by chemical reduction with $NaBH_4$
Au($NaBH_4$)/TiO_2	Au/TiO_2 synthesized by chemical reduction with $NaBH_4$
ACFF	activated carbon fiber flet
TiNF	titania nanofiber
ACF	activated carbon fiber
MTi5	5 wt% calcium treated g-C_3N_4/TiO_2 (Ca^{2+}/g-C_3N_4/TiO_2)
VUV	vacuum ultraviolet
WFGD	wet flue gas desulphurization
DPCO	dry photocatalytic oxidation
BFG	basic flue gas
FGFs	fiberglass fibers
CCFs	carbon cloth fibers
PCO	photocatalytic oxidation
PSCO	photo-selective catalytic oxidation
PSCR	photo-selective catalytic reduction

Acknowledgement

This work described in this paper was substantially supported by the National Natural Science Foundation of China (NSFC) and the Research Grants Council (RGC) of Hong Kong Joint Research Scheme (No. 51561165015 and No. N_HKU718/15), NSFC (21677179), the Guangdong Special Fund for Science & Technology Development (Hong Kong Technology Cooperation Funding Scheme) (No. 2016A050503022), the Innovation Platform Construction of Guangdong and Hong Kong (No. 2017B050504001), Guangzhou Science and Technology Project (No. 201504301654288), the Key Fundamental Research Fund for the Central Universities (17lgjc17) and the National Key Research and Development Program of China (No. 2016YFC0204800).

References

Abbas, N., Hussain, M., Russo, N., Saracco, G., 2011. Studies on the activity and deactivation of novel optimized TiO_2 nanoparticles for the abatement of VOCs. Chem. Eng. J. 175, 330–340.

Alonso-Tellez, A., Robert, D., Keller, V., Keller, N., 2014. H_2S photocatalytic oxidation over WO_3/TiO_2 Hombikat UV100. Environ. Sci. Pollut. Res. 21, 3503–3514.

Andryushina, N.S., Stroyuk, O.L., 2014. Influence of colloidal graphene oxide on photocatalytic activity of nanocrystalline TiO_2 in gas-phase ethanol and benzene oxidation. Appl. Catal. B Environ. 148–149, 543–549.

Anpo, M., Takeuchi, M., 2003. The design and development of highly reactive titanium oxide photocatalysts operating under visible light irradiation. J. Catal. 216, 505–516.

Asahi, R., Morikawa, T., Ohwaki, T., Aoki, K., Taga, Y., 2001. Visible-light photocatalysis in nitrogen-doped titanium oxides. Science 293, 269–271.

Assadi, A.A., Bouzaza, A., Merabet, S., Wolbert, D., 2014. Modeling and simulation of VOCs removal by nonthermal plasma discharge with photocatalysis in a continuous

reactor: synergetic effect and mass transfer. Chem. Eng. J. 258, 119–127.
Belver, C., Bellod, R., Fuerte, A., Fernandez-Garcia, M., 2006. Nitrogen-containing TiO_2 photocatalysts-part 1. Synthesis and solid characterization. Appl. Catal. B Environ. 65, 301–308.
Bhachu, D.S., Egdell, R.G., Sankar, G., Carmalt, C.J., Parkin, I.P., 2017. Electronic properties of antimony-doped anatase TiO_2 thin films prepared by aerosol assisted chemical vapour deposition. J. Mater. Chem. C 5, 9694–9701.
Bhirud, A.P., Sathaye, S.D., Waichal, R.P., Ambekar, J.D., Park, C.J., Kale, B.B., 2015. In-situ preparation of N-TiO_2/graphene nanocomposite and its enhanced photocatalytic hydrogen production by H_2S splitting under solar light. Nanoscale 7, 5023–5034.
Bianchi, C.L., Gatto, S., Pirola, C., Naldoni, A., Di Michele, A., Cerrato, G., et al., 2014. Photocatalytic degradation of acetone, acetaldehyde and toluene in gas-phase: comparison between nano and micro-sized TiO_2. Appl. Catal. B Environ. 146, 123–130.
Bianchi, C.L., Pirola, C., Galli, F., Cerrato, G., Morandi, S., Capucci, V., 2015. Pigmentary TiO_2: a challenge for its use as photocatalyst in NO_x air purification. Chem. Eng. J. 261, 76–82.
Boyjoo, Y., Sun, H.Q., Liu, J., Pareek, V.K., Wang, S.B., 2017. A review on photocatalysis for air treatment: from catalyst development to reactor design. Chem. Eng. J. 310, 537–559.
Brancher, M., Franco, D., Lisboa, H.D., 2016. Photocatalytic oxidation of H_2S in the gas phase over TiO_2-coated glass fiber filter. Environ. Technol. 37, 2852–2864.
Cai, W., Gu, W., Zhu, L.X., Lv, W., Xia, C.L., Ding, B., 2014. Photocatalytic oxidation of gaseous acetone and ethanol mixtures over titanium dioxide powders. Bulg. Chem. Commun. 46, 911–917.
Chaisiwamongkhol, K., Manoyen, N., Suttiponparnit, M., Nacapricha, D., Smith, S.M., Uraisin, K., 2017. Development of gas flow reactor with on-line monitoring system for nitrogen dioxide removal. Microchem. J. 135, 199–206.
Chang, F., Zhang, J., Xie, Y.C., Chen, J., Li, C.L., Wang, J., et al., 2014. Fabrication, characterization, and photocatalytic performance of exfoliated g-C_3N_4-TiO_2 hybrids. Appl. Surf. Sci. 311, 574–581.
Chatchai, P., Kishioka, S.Y., Murakami, Y., Nosaka, A.Y., Nosaka, Y., 2010. Enhanced photoelectrocatalytic activity of FTO/WO_3/$BiVO_4$ electrode modified with gold nanoparticles for water oxidation under visible light irradiation. Electrochim. Acta 55, 592–596.
Chen, X.B., Liu, L., Yu, P.Y., Mao, S.S., 2011. Increasing solar absorption for photocatalysis with black hydrogenated titanium dioxide nanocrystals. Science 331, 746–750.
Chen, K.Y., Zhu, L.Z., Yang, K., 2015. Acid-assisted hydrothermal synthesis of nanocrystalline TiO_2 from titanate nanotubes: influence of acids on the photodegradation of gaseous toluene. J. Environ. Sci. 27, 232–240.
Chen, Y.-C., Katsumata, K.-i., Chiu, Y.-H., Okada, K., Matsushita, N., Hsu, Y.-J., 2015. ZnO-graphene composites as practical photocatalysts for gaseous acetaldehyde degradation and electrolytic water oxidation. Appl. Catal. A Gen. 490, 1–9.
Chen, L., Yang, S.D., Mu, L., Ma, P.C., 2018. Three-dimensional titanium dioxide/graphene hybrids with improved performance for photocatalysis and energy storage. J. Colloid Interface Sci. 512, 647–656.
Chu, S., Zheng, X.M., Kong, F., Wu, G.H., Luo, L.L., Guo, Y., et al., 2011. Architecture of Cu_2O@TiO_2 core-shell heterojunction and photodegradation for 4-nitrophenol under simulated sunlight irradiation. Mater. Chem. Phys. 129, 1184–1188.
Cloteaux, A., Gerardin, F., Thomas, D., Midoux, N., Andre, J.C., 2014. Fixed bed photocatalytic reactor for formaldehyde degradation: experimental and modeling study. Chem. Eng. J. 249, 121–129.
Cometto, C., Kuriki, R., Chen, L.J., Maeda, K., Lau, T.C., Ishitani, O., et al., 2018. A carbon nitride/Fe quaterpyridine catalytic system for photostimulated CO_2-to-CO conversion with visible light. J. Am. Chem. Soc. 140, 7437–7440.
Cong, Y., Zhang, J.L., Chen, F., Anpo, M., He, D.N., 2007. Preparation, photocatalytic activity, and mechanism of nano-TiO_2 co-doped with nitrogen and iron (III). J. Phys. Chem. C 111, 10618–10623.
Debe, M.K., 2012. Electrocatalyst approaches and challenges for automotive fuel cells. Nature 486, 43–51.
Devaraji, P., Sathu, N.K., Gopinath, C.S., 2014. Ambient oxidation of benzene to phenol by photocatalysis on Au/$Ti_{0.98}V_{0.02}O_2$: role of holes. ACS Catal. 4, 2844–2853.
Devipriya, S., Yesodharan, S., 2005. Photocatalytic degradation of pesticide contaminants in water. Sol. Energy Mater. Sol. Cells 86, 309–348.
Dinh, C.T., Burdyny, T., Kibria, M.G., Seifitokaldani, A., Gabardo, C.M., de Arquer, F.P.G., et al., 2018. CO_2 electroreduction to ethylene via hydroxide-mediated copper catalysis at an abrupt interface. Science 360, 783–787.
Dolat, D., Quici, N., Kusiak-Nejman, E., Morawski, A.W., Puma, G.L., 2012. One-step, hydrothermal synthesis of nitrogen, carbon co-doped titanium dioxide (N,C-TiO_2) photocatalysts. Effect of alcohol degree and chain length as carbon dopant precursors on photocatalytic activity and catalyst deactivation. Appl. Catal. B Environ. 115-116, 81–89.
Ebrahimi, A., Fatemi, S., 2017. Titania-reduced graphene oxide nanocomposite as a promising visible light-active photocatalyst for continuous degradation of VVOC in air purification process. Clean Techn. Environ. Policy 19, 2089–2098.
Erjavec, B., Tisler, T., Tchernychova, E., Plahuta, M., Pintar, A., 2017. Self-doped Cu-deposited titania nanotubes as efficient visible light photocatalyst. Catal. Lett. 147, 1686–1695.
Falk, G.S., Borlaf, M., Lopez-Munoz, M.J., Farinas, J.C., Neto, J.B.R., Moreno, R., 2018. Microwave-assisted synthesis of TiO_2 nanoparticles: photocatalytic activity of powders and thin films. J. Nanopart. Res. 20, 23.
Farhanian, D., Haghighat, F., 2014. Photocatalytic oxidation air cleaner: identification and quantification of by-products. Build. Environ. 72, 34–43.
Fasciani, C., Lanterna, A.E., Giorgi, J.B., Scaiano, J.C., 2017. Visible light production of hydrogen by ablated graphene: water splitting or carbon gasification? J. Am. Chem. Soc. 139, 11024–11027.
Feng, F., Yang, W.Y., Gao, S., Sun, C.X., Li, Q., 2018. Postillumination activity in a single-phase photocatalyst of Mo-doped TiO_2 nanotube array from its photocatalytic "memory". ACS Sustain. Chem. Eng. 6, 6166–6174.
Fischer, K., Gawel, A., Rosen, D., Krause, M., Latif, A.A., Griebel, J., et al., 2017. Low-temperature synthesis of anatase/rutile/brookite TiO_2 nanoparticles on a polymer membrane for photocatalysis. Catalysts 7, 209.
Fresno, F., Hernandez-Alonso, M.D., Tudela, D., Coronado, J.M., Soria, J., 2008. Photocatalytic degradation of toluene over doped and coupled (Ti,M)O_2 (M = Sn or Zr) nanocrystalline oxides: influence of the heteroatom distribution on deactivation. Appl. Catal. B Environ. 84, 598–606.
Fu, P.F., Zhang, P.Y., Li, J., 2011. Photocatalytic degradation of low concentration formaldehyde and simultaneous elimination of ozone by-product using palladium modified TiO_2 films under UV254 + 185 nm irradiation. Appl. Catal. B Environ. 105, 220–228.
Fu, P.F., Zhang, P.Y., Li, J., 2012. Simultaneous elimination of formaldehyde and ozone byproduct using noble metal modified TiO_2 films in the gaseous VUV photocatalysis. Int. J. Photoenergy, 174862.
Fujishima, A., Honda, K., 1972. Electrochemical photolysis of water at a semiconductor electrode. Nature 238, 37–38.
Gaidau, C., Petica, A., Ignat, M., Popescu, L.M., Piticescu, R.M., Tudor, J.A., et al., 2017. Preparation of silica doped titania nanoparticles with thermal stability and photocatalytic properties and their application for leather surface functionalization. Arab. J. Chem. 10, 985–1000.
Georgieva, J., Valova, E., Armyanov, S., Philippidis, N., Poulios, I., Sotiropoulos, S., 2012. Bi-component semiconductor oxide photoanodes for the photoelectrocatalytic oxidation of organic solutes and vapours: a short review with emphasis to TiO_2-WO_3 photoanodes. J. Hazard. Mater. 211-212, 30–46.
Gholami, M., Nassehinia, H.R., Jonidi-Jafari, A., Nasseri, S., Esrafili, A., 2014. Comparison of benzene & toluene removal from synthetic polluted air with use of nano photocatalytic TiO_2/ZnO process. J. Environ. Health Sci. Eng. 12, 45.
Ghosh, A.K., Maruska, H.P., 1977. Photoelectrolysis of water in sunlight with sensitized semiconductor electrodes. J. Electrochem. Soc. 124, 1516–1522.
Grzeskowiak, M., Wrobel, R.J., Moszynski, D., Mozia, S., Grzechulska-Damszel, J., Morawski, A.W., et al., 2014. TiO_2 supported on quartz wool for photocatalytic oxidation of hydrogen sulphide. Adsorpt. Sci. Technol. 32, 765–773.
Gui, M.M., Chai, S.P., Xu, B.Q., Mohamed, A.R., 2014. Enhanced visible light responsive MWCNT/TiO_2 core-shell nanocomposites as the potential photocatalyst for reduction of CO_2 into methane. Sol. Energy Mater. Sol. Cells 122, 183–189.
Guo, H., Ling, Z.H., Cheng, H.R., Simpson, I.J., Lyu, X.P., Wang, X.M., et al., 2017. Tropospheric volatile organic compounds in China. Sci. Total Environ. 574, 1021–1043.
Haldorai, Y., Rengaraj, A., Kwak, C.H., Huh, Y.S., Han, Y.-K., 2014. Fabrication of nano TiO_2@graphene composite: reusable photocatalyst for hydrogen production, degradation of organic and inorganic pollutants. Synth. Met. 198, 10–18.
Han, Y.H., Zhang, J.J., Zhao, Y., 2016. Visible-light-induced photocatalytic oxidation of nitric oxide and sulfur dioxide: discrete kinetics and mechanism. Energy 103, 725–734.
Han, S.Y., Pan, D.L., Chen, H., Bu, X.B., Gao, Y.X., Gao, H., et al., 2018. A methylthio-functionalized-MOF photocatalyst with high performance for visible-light-driven H_2 evolution. Angew. Chem. Int. Ed. 57, 9864–9869.
Helm, M.L., Stewart, M.P., Bullock, R.M., DuBois, M.R., DuBois, D.L., 2011. A synthetic nickel electrocatalyst with a turnover frequency above 100,000 s^{-1} for H_2 production. Science 333, 863–866.
Hoffmann, M.R., Martin, S.T., Choi, W.Y., Bahnemann, D.W., 1995. Environmental applications of semiconductor photocatalysis. Chem. Rev. 95, 69–96.
Hou, C., Zhang, Q., Li, Y., Wang, H., 2012. P25-graphene hydrogels: room-temperature synthesis and application for removal of methylene blue from aqueous solution. J. Hazard. Mater. 205–206, 229–235.
Huang, H.J., Li, D.Z., Lin, Q., Zhang, W.J., Shao, Y., Chen, Y.B., et al., 2009. Efficient degradation of benzene over $LaVO_4$/TiO_2 nanocrystalline heterojunction photocatalyst under visible light irradiation. Environ. Sci. Technol. 43, 4164–4168.
Huang, L., Peng, F., Yu, H., Wang, H.J., 2009. Preparation of cuprous oxides with different sizes and their behaviors of adsorption, visible-light driven photocatalysis and photocorrosion. Solid State Sci. 11, 129–138.
Huang, H.B., Leung, D.Y.C., Li, G.S., Leung, M.K.H., Fu, X.L., 2011. Photocatalytic destruction of air pollutants with vacuum ultraviolet (VUV) irradiation. Catal. Today 175, 310–315.
Huang, H.B., Ye, X.G., Huang, H.L., Hu, P., Zhang, L., Leung, D.Y.C., 2013. Photocatalytic oxidation of gaseous benzene under 185 nm UV irradiation. Int. J. Photoenergy, 890240.
Huang, H.L., Huang, H.B., Zhan, Y.J., Liu, G.Y., Wang, X.M., Lu, H.X., et al., 2016. Efficient degradation of gaseous benzene by VUV photolysis combined with ozone-assisted catalytic oxidation: performance and mechanism. Appl. Catal. B Environ. 186, 62–68.
Huang, H.B., Lu, H.X., Zhan, Y.J., Liu, G.Y., Feng, Q.Y., Huang, H.L., et al., 2017a. VUV photo-oxidation of gaseous benzene combined with ozone-assisted catalytic oxidation: effect on transition metal catalyst. Appl. Surf. Sci. 391, 662–667.
Huang, H.B., Huang, H.L., Feng, Q.Y., Liu, G.Y., Zhan, Y.J., Wu, M.Y., et al., 2017b. Catalytic oxidation of benzene over Mn modified TiO_2/ZSM-5 under vacuum UV irradiation. Appl. Catal. B Environ. 203, 870–878.
Huang, H.B., Liu, G.Y., Zhan, Y.J., Xu, Y., Lu, H.X., Huang, H.L., et al., 2017c. Photocatalytic oxidation of gaseous benzene under VUV irradiation over TiO_2/zeolites catalysts. Catal. Today 281, 649–655.
Hunge, Y.M., Yadav, A.A., Mahadik, M.A., Bulakhe, R.N., Shim, J.J., Mathe, V.L., et al., 2018. Degradation of organic dyes using spray deposited nanocrystalline stratified

WO_3/TiO_2 photoelectrodes under sunlight illumination. Opt. Mater. 76, 260–270.
Ihara, T., Miyoshi, M., Iriyama, Y., Matsumoto, O., Sugihara, S., 2003. Visible-light-active titanium oxide photocatalyst realized by an oxygen-deficient structure and by nitrogen doping. Appl. Catal. B Environ. 42, 403–409.
Irokawa, Y., Morikawa, T., Aoki, K., Kosaka, S., Ohwaki, T., Taga, Y., 2006. Photodegradation of toluene over $TiO_{2-x}N_x$ under visible light irradiation. Phys. Chem. Chem. Phys. 8, 1116–1121.
Islam, S.Z., Nagpure, S., Kim, D.Y., Rankin, S.E., 2017. Synthesis and catalytic applications of non-metal doped mesoporous titania. Inorganics 5, 15.
Janus, M., Bubacz, K., Zatorska, J., Kusiak-Nejman, E., Czyzewski, A., Morawski, A.W., 2015. NO_x photocatalytic degradation on gypsum plates modified by TiO_2-N,C photocatalysts. Pol. J. Chem. Technol. 17, 8–12.
Ji, J., Xu, Y., Huang, H.B., He, M., Liu, S.L., Liu, G.Y., et al., 2017. Mesoporous TiO_2 under VUV irradiation: enhanced photocatalytic oxidation for VOCs degradation at room temperature. Chem. Eng. J. 327, 490–499.
Jing, L.Q., Xin, B.F., Yuan, F.L., Wang, B.Q., Shi, K.Y., Cai, W.M., et al., 2004. Deactivation and regeneration of ZnO and TiO_2 nanoparticles in the gas phase photocatalytic oxidation of n-C_7H_{16} or SO_2. Appl. Catal. A Gen. 275, 49–54.
Jing, J., Zhang, Y., Li, W., Yu, W.W., 2014. Visible light driven photodegradation of quinoline over TiO_2/graphene oxide nanocomposites. J. Catal. 316, 174–181.
Jo, W.K., Kang, H.J., 2013. Titanium dioxide-graphene oxide composites with different ratios supported by Pyrex tube for photocatalysis of toxic aromatic vapors. Powder Technol. 250, 115–121.
Jo, W.K., Kim, J.T., 2009. Application of visible-light photocatalysis with nitrogen-doped or unmodified titanium dioxide for control of indoor-level volatile organic compounds. J. Hazard. Mater. 164, 360–366.
Kaidashev, E.M., Lorenz, M., von Wenckstern, H., Rahm, A., Semmelhack, H.C., Han, K.H., et al., 2003. High electron mobility of epitaxial ZnO thin films on c-plane sapphire grown by multistep pulsed-laser deposition. Appl. Phys. Lett. 82, 3901–3903.
Kako, T., Zou, Z.G., Katagiri, M., Ye, J.H., 2007. Decomposition of organic compounds over $NaBiO_3$ under visible light irradiation. Chem. Mater. 19, 198–202.
Kakuta, S., Abe, T.A., 2009. Novel example of molecular hydrogen generation from formic acid at visible-light-responsive photocatalyst. ACS Appl. Mater. Interfaces 1, 2707–2710.
Kaky, K.M., Lakshminarayana, G., Baki, S.O., Kityk, I.V., Taufiq-Yap, Y.H., Mahdi, M.A., 2017. Structural, thermal and optical absorption features of heavy metal oxides doped tellurite rich glasses. Results Phys. 7, 166–174.
Kannangara, Y.Y., Wijesena, R., Rajapakse, R.M.G., de Silva, K.M.N., 2018. Heterogeneous photocatalytic degradation of toluene in static environment employing thin films of nitrogen-doped nano-titanium dioxide. Int. Nano Lett. 8, 31–39.
Karousis, N., Tagmatarchis, N., Tasis, D., 2010. Current progress on the chemical modification of carbon nanotubes. Chem. Rev. 110, 5366–5397.
Kataoka, S., Lee, E., Tejedor-Tejedor, M.I., Anderson, M.A., 2005. Photocatalytic degradation of hydrogen sulfide and in situ FT-IR analysis of reaction products on surface of TiO_2. Appl. Catal. B Environ. 61, 159–163.
Kim, K.J., Ahn, H.G., 2012. The effect of pore structure of zeolite on the adsorption of VOCs and their desorption properties by microwave heating. Microporous Mesoporous Mater. 152, 78–83.
Kim, J.K., Chai, S.U., Cho, Y., Cai, L.L., Kim, S.J., Park, S., et al., 2017. Ultrafast flame annealing of TiO_2 paste for fabricating dye-sensitized and perovskite solar cells with enhanced efficiency. Small 13, 1702260.
Koci, K., Reli, M., Troppova, I., Sihor, M., Kupkova, J., Kustrowski, P., et al., 2017. Photocatalytic decomposition of N_2O over TiO_2/g-C_3N_4 photocatalysts heterojunction. Appl. Surf. Sci. 396, 1685–1695.
Kolinko, P.A., Kozlov, D.V., 2009. Products distribution during the gas phase photocatalytic oxidation of ammonia over the various titania based photocatalysts. Appl. Catal. B Environ. 90, 126–131.
Konstantinou, I.K., Albanis, T.A., 2003. Photocatalytic transformation of pesticides in aqueous titanium dioxide suspensions using artificial and solar light: intermediates and degradation pathways. Appl. Catal. B Environ. 42, 319–335.
Kubacka, A., Munoz-Batista, M.J., Ferrer, M., Fernandez-Garcia, M., 2018. Er-W codoping of TiO_2-anatase: structural and electronic characterization and disinfection capability under UV-vis, and near-IR excitation. Appl. Catal. B Environ. 228, 113–129.
Kudo, A., Ueda, K., Kato, H., Mikami, I., 1998. Photocatalytic O_2 evolution under visible light irradiation on $BiVO_4$ in aqueous $AgNO_3$ solution. Catal. Lett. 53, 229–230.
Kung, H.H., Jarrett, H.S., Sleight, A.W., Ferretti, A., 1977. Semiconducting oxide anodes in photoassisted electrolysis of water. J. Appl. Phys. 48, 2463–2469.
Kwon, Y.T., Song, K.Y., Lee, W.I., Choi, G.J., Do, Y.R., 2000. Photocatalytic behavior of WO_3-loaded TiO_2 in an oxidation reaction. J. Catal. 191, 192–199.
Leary, R., Westwood, A., 2011. Carbonaceous nanomaterials for the enhancement of TiO_2 photocatalysis. Carbon 49, 741–772.
Li, F.B., Li, X.Z., Ao, C.H., Lee, S.C., Hou, M.F., 2005. Enhanced photocatalytic degradation of VOCs using Ln^{3+}-TiO_2 catalysts for indoor air purification. Chemosphere 59, 787–800.
Li, X.K., Ouyang, S.X., Kikugawa, N., Ye, J.H., 2008. Novel Ag_2ZnGeO_4 photocatalyst for dye degradation under visible light irradiation. Appl. Catal. A Gen. 334, 51–58.
Li, G.T., Yip, H.Y., Hu, C., Wong, P.K., 2011. Preparation of grape-like Bi_2O_3/Ti photoanode and its visible light activity. Mater. Res. Bull. 46, 153–157.
Li, X., Zhang, G.Q., Pan, H.G., 2012. Experimental study on ozone photolytic and photocatalytic degradation of H_2S using continuous flow mode. J. Hazard. Mater. 199–200, 255–261.
Li, J., Zhou, S.L., Hong, G.-B., Chang, C.-T., 2013. Hydrothermal preparation of P25-graphene composite with enhanced adsorption and photocatalytic degradation of dyes. Chem. Eng. J. 219, 486–491.
Li, G.Y., Nie, X., Chen, J.Y., Jiang, Q., An, T.C., Wong, P.K., et al., 2015. Enhanced visible-light-driven photocatalytic inactivation of *Escherichia coli* using g-C_3N_4/TiO_2 hybrid photocatalyst synthesized using a hydrothermal-calcination approach. Water Res. 86, 17–24.
Li, Y., Yang, J., Zheng, S.H., Zeng, W.W., Zhao, N., Shen, M., 2016. One-pot synthesis of 3D TiO_2-reduced graphene oxide aerogels with superior adsorption capacity and enhanced visible-light photocatalytic performance. Ceram. Int. 42, 19091–19096.
Li, M., Lu, B., Ke, Q.F., Guo, Y.J., Guo, Y.P., 2017. Synergetic effect between adsorption and photodegradation on nanostructured TiO_2/activated carbon fiber felt porous composites for toluene removal. J. Hazard. Mater. 333, 88–98.
Li, Y.H., Lv, K.L., Ho, W.K., Dong, F., Wu, X.F., Xia, Y., 2017. Hybridization of rutile TiO_2 ($rTiO_2$) with g-C_3N_4 quantum dots (CN QDs): an efficient visible-light-driven Z-scheme hybridized photocatalyst. Appl. Catal. B Environ. 202, 611–619.
Lianos, P., 2011. Production of electricity and hydrogen by photocatalytic degradation of organic wastes in a photoelectrochemical cell the concept of the photofuelcell: a review of a re-emerging research field. J. Hazard. Mater. 185, 575–590.
Liu, G., Chen, Z.G., Dong, C.L., Zhao, Y.N., Li, F., Lu, G.Q., et al., 2006. Visible light photocatalyst: iodine-doped mesoporous titania with a bicrystalline framework. J. Phys. Chem. B 110, 20823–20828.
Liu, Y.Y., Huang, B.B., Dai, Y., Zhang, X.Y., Qin, X.Y., Jiang, M.H., et al., 2009. Selective ethanol formation from photocatalytic reduction of carbon dioxide in water with $BiVO_4$ photocatalyst. Catal. Commun. 11, 210–213.
Liu, J., Liu, Y., Liu, N.Y., Han, Y.Z., Zhang, X., Huang, H., et al., 2015. Metal-free efficient photocatalyst for stable visible water splitting via a two-electron pathway. Science 347, 970–974.
Liu, Y.X., Xu, W., Zhao, L., Wang, Y., Zhang, J., 2017. Absorption of NO and simultaneous absorption of SO_2/NO using a vacuum ultraviolet light/ultrasound/$KHSO_5$ system. Energy Fuel 31, 12364–12375.
Liu, G.Y., Ji, J., Huang, H.B., Xie, R.J., Feng, Q.Y., Shu, Y.J., et al., 2017. UV/H_2O_2: an efficient aqueous advanced oxidation process for VOCs removal. Chem. Eng. J. 324, 44–50.
Liu, W., Cao, L.L., Cheng, W.R., Cao, Y.J., Liu, X.K., Zhang, W., et al., 2017. Single-site active cobalt-based photocatalyst with a long carrier lifetime for spontaneous overall water splitting. Angew. Chem. Int. Ed. 56, 9312–9317.
Liu, Y.X., Wang, Y., Wang, Q., Pan, J.F., Zhang, J., 2018. Simultaneous removal of NO and SO_2 using vacuum ultraviolet light (VUV)/heat/peroxymonosulfate (PMS). Chemosphere 190, 431–441.
Liu, G.Y., Ji, J., Hu, P., Lin, S.X., Huang, H.B., 2018. Efficient degradation of H_2S over transition metal modified TiO_2 under VUV irradiation: performance and mechanism. Appl. Surf. Sci. 433, 329–335.
Liu, J., Li, Y., Ke, J., Wang, S.B., Wang, L.D., Xiao, H.N., 2018. Black NiO-TiO_2 nanorods for solar photocatalysis: recognition of electronic structure and reaction mechanism. Appl. Catal. B Environ. 224, 705–714.
Long, M., Cai, W.M., Cai, J., Zhou, B.X., Chai, X.Y., 2006. Wu YH. Efficient photocatalytic degradation of phenol over Co_3O_4/$BiVO_4$ composite under visible light irradiation. J. Phys. Chem. B 110, 20211–20216.
Luna-Flores, A., Sosa-Sanchez, J.L., Morales-Sanchez, M.A., Agustin-Serrano, R., Luna-Lopez, J.A., 2017. An easy-made, economical and efficient carbon-doped amorphous TiO_2 photocatalyst obtained by microwave assisted synthesis for the degradation of rhodamine B. Materials 10, 1447.
Luo, S., Nguyen-Phan, T.D., Vovchok, D., Waluyo, I., Palomino, R.M., Gamalski, A.D., et al., 2018. Enhanced, robust light-driven H_2 generation by gallium-doped titania nanoparticles. Phys. Chem. Chem. Phys. 20, 2104–2112.
Lyu, J.Z., Gao, J.X., Zhang, M., Fu, Q., Sun, L.N., Hu, S., et al., 2017. Construction of homojunction-adsorption layer on anatase TiO_2 to improve photocatalytic mineralization of volatile organic compounds. Appl. Catal. B Environ. 202, 664–670.
Ma, J.Z., Wang, C.X., He, H., 2016. Enhanced photocatalytic oxidation of NO over g-C_3N_4-TiO_2 under UV and visible light. Appl. Catal. B Environ. 184, 28–34.
Maeda, K., Teramura, K., Lu, D.L., Takata, T., Saito, N., Inoue, Y., et al., 2006. Photocatalyst releasing hydrogen from water-enhancing catalytic performance holds promise for hydrogen production by water splitting in sunlight. Nature 440, 295.
Mazabuel-Collazos, A., Rodriguez-Paez, J.E., 2018. Chemical synthesis and characterization of ZnO-TiO_2 semiconductor nanocomposites: tentative mechanism of particle formation. J. Inorg. Organomet. Polym. Mater. 28, 1739–1752.
Metikoshukovic, M., 1981. The photoelectrochemical properties of anodic Bi_2O_3 films. Electrochim. Acta 26, 989–1000.
Minami, T., Tanaka, H., Shimakawa, T., Miyata, T., Sato, H., 2004. High-efficiency oxide heterojunction solar cells using Cu_2O sheets. Jpn. J. Appl. Phys. 2 Lett. 43, L917–L919.
Miranda-Garcia, N., Suarez, S., Maldonado, M.I., Malato, S., Sanchez, B., 2014. Regeneration approaches for TiO_2 immobilized photocatalyst used in the elimination of emerging contaminants in water. Catal. Today 230, 27–34.
Miyauchi, M., Nakajima, A., Fujishima, A., Hashimoto, K., Watanabe, T., 2000. Photoinduced surface reactions on TiO_2 and $SrTiO_3$ films: photocatalytic oxidation and photoinduced hydrophilicity. Chem. Mater. 12, 3–5.
Miyauchi, M., Ikezawa, A., Tobimatsu, H., Irie, H., Hashimoto, K., 2004. Zeta potential and photocatalytic activity of nitrogen doped TiO_2 thin films. Phys. Chem. Chem. Phys. 6, 865–870.
Monai, M., Montini, T., Fornasiero, P., 2017. Brookite: nothing new under the sun? Catalysts 7, 304.
Moradi, V., Jun, M.B.G., Blackburn, A., Herring, R.A., 2018. Significant improvement in visible light photocatalytic activity of Fe doped TiO_2 using an acid treatment process. Appl. Surf. Sci. 427, 791–799.
Morales-Torres, S., Pastrana-Martinez, L.M., Figueiredo, J.L., Faria, J.L., Silva, A.M.T., 2013. Graphene oxide-P25 photocatalysts for degradation of diphenhydramine pharmaceutical and methyl orange dye. Appl. Surf. Sci. 275, 361–368.
Mull, B., Mohlmann, L., Wilke, O., 2017. Photocatalytic degradation of toluene, butyl

acetate and limonene under UV and visible light with titanium dioxide-graphene oxide as photocatalyst. Environments 4, 9.
Munoz-Batista, M.J., Kubacka, A., Fernandez-Garcia, M., 2014. Effect of g-C_3N_4 loading on TiO_2-based photocatalysts: UV and visible degradation of toluene. Cat. Sci. Technol. 4, 2006–2015.
Myung, N., Ham, S., Choi, S., Chae, Y., Kim, W.G., Jeon, Y.J., et al., 2011. Tailoring interfaces for electrochemical synthesis of semiconductor films: $BiVO_4$, Bi_2O_3, or composites. J. Phys. Chem. C 115, 7793–7800.
Nagaraju, G., Udayabhanu, Shivaraj, Prashanth, S.A., Shastri, M., Yathish, K.V., et al., 2017. Electrochemical heavy metal detection, photocatalytic, photoluminescence, biodiesel production and antibacterial activities of Ag-ZnO nanomaterial. Mater. Res. Bull. 94, 54–63.
Natarajan, T.S., Lee, J.Y., Bajaj, H.C., Jo, W.K., Tayade, R.J., 2017. Synthesis of multiwall carbon nanotubes/TiO_2 nanotube composites with enhanced photocatalytic decomposition efficiency. Catal. Today 282, 13–23.
Nawaz, M., Miran, W., Jang, J., Lee, D.S., 2017. One-step hydrothermal synthesis of porous 3D reduced graphene oxide/TiO_2 aerogel for carbamazepine photodegradation in aqueous solution. Appl. Catal. B Environ. 203, 85–95.
Neppolian, B., Vinoth, R., Bianchi, C.L., Ashokkumar, M., 2015. Degradation of 4-chlorophenol and NO_x using ultrasonically synthesized TiO_2 loaded graphene oxide photocatalysts. Sci. Adv. Mater. 7, 1149–1155.
Nethi, S.K., Anand, P.N.A., Rico-Oller, B., Rodriguez-Dieguez, A., Gomez-Ruiz, S., Patra, C.R., 2017. Design, synthesis and characterization of doped-titanium oxide nanomaterials with environmental and angiogenic applications. Sci. Total Environ. 599–600, 1263–1274.
Nolan, N.T., Seery, M.K., Pillai, S.C., 2009. Spectroscopic investigation of the anatase-to-rutile transformation of sol-gel-synthesized TiO_2 photocatalysts. J. Phys. Chem. C 113, 16151–16157.
Ochiai, T., Masuko, K., Tago, S., Nakano, R., Niitsu, Y., Kobayashi, G., et al., 2013. Development of a hybrid environmental purification unit by using of excimer VUV lamps with TiO_2 coated titanium mesh filter. Chem. Eng. J. 218, 327–332.
Ogwu, A.A., Bouquerel, E., Ademosu, O., Moh, S., Crossan, E., Placido, F., 2005. The influence of rf power and oxygen flow rate during deposition on the optical transmittance of copper oxide thin films prepared by reactive magnetron sputtering. J. Phys. D. Appl. Phys. 38, 266–271.
Ohtani, B., 2014. Revisiting the original works related to titania photocatalysis: a review of papers in the early stage of photocatalysis studies. Electrochemistry 82, 414–425.
Osterloh, F.E., 2008. Inorganic materials as catalysts for photochemical splitting of water. Chem. Mater. 20, 35–54.
Ouyang, S.X., Zhang, H.T., Li, D.F., Yu, T., Ye, J.H., Zou, Z.G., 2006. Electronic structure and photocatalytic characterization of a novel photocatalyst $AgAlO_2$. J. Phys. Chem. B 110, 11677–11682.
Ouyang, S.X., Kikugawa, N., Zou, Z.G., Ye, J.H., 2009a. Effective decolorizations and mineralizations of organic dyes over a silver germanium oxide photocatalyst under indoor-illumination irradiation. Appl. Catal. A Gen. 366, 309–314.
Ouyang, S.X., Kikugawa, N., Chen, D., Zou, Z.G., Ye, J.H., 2009b. A systematical study on photocatalytic properties of $AgMO_2$ (M = Al, Ga, In): effects of chemical compositions, crystal structures, and electronic structures. J. Phys. Chem. C 113, 1560–1566.
Papailias, I., Todorova, N., Giannakopoulou, T., Yu, J.G., Dimotikali, D., Trapalis, C., 2017. Photocatalytic activity of modified g-C_3N_4/TiO_2 nanocomposites for NO_x removal. Catal. Today 280, 37–44.
Park, S.Y., Cho, B.W., Yun, K.S., Lee, E.C., 1994. Photoelectrochemical properties of bismuth-doped titanium-oxide electrodes. J. Appl. Electrochem. 24, 1133–1138.
Paz, Y., 2010. Application of TiO_2 photocatalysis for air treatment: patents' overview. Appl. Catal. B Environ. 99, 448–460.
Pelizzetti, E., Minero, C., 1999. Role of oxidative and reductive pathways in the photocatalytic degradation of organic compounds. Colloids Surf. A Physicochem. Eng. Asp. 151, 321–327.
Petronella, F., Curri, M.L., Striccoli, M., Fanizza, E., Mateo-Mateo, C., Alvarez-Puebla, R.A., et al., 2015. Direct growth of shape controlled TiO_2 nanocrystals onto SWCNTs for highly active photocatalytic materials in the visible. Appl. Catal. B Environ. 178, 91–99.
Petronella, F., Truppi, A., Ingrosso, C., Placido, T., Striccoli, M., Curri, M.L., et al., 2017. Nanocomposite materials for photocatalytic degradation of pollutants. Catal. Today 281, 85–100.
Portela, R., Sanchez, B., Coronado, J.M., Candal, R., Suarez, S., 2007. Selection of TiO_2-support: UV-transparent alternatives and long-term use limitations for H_2S removal. Catal. Today 129, 223–230.
Poulios, I., Tsachpinis, I., 1999. Photodegradation of the textile dye reactive black 5 in the presence of semiconducting oxides. J. Chem. Technol. Biotechnol. 74, 349–357.
Poulios, I., Avranas, A., Rekliti, E., Zouboulis, A., 2000. Photocatalytic oxidation of auramine O in the presence of semiconducting oxides. J. Chem. Technol. Biotechnol. 75, 205–212.
Prieto, O., Fermoso, J., Irusta, R., 2007. Photocatalytic degradation of toluene in air using a fluidized bed photoreactor. Int. J. Photoenergy, 32859.
Qiao, X.X., Li, Q.Q., Schaugaard, R.N., Noffke, B.W., Liu, Y.J., Li, D.P., et al., 2017. Well-defined nanographene-rhenium complex as an efficient electrocatalyst and photocatalyst for selective CO_2 reduction. J. Am. Chem. Soc. 139, 3934–3937.
Ratova, M., Kelly, P.J., West, G.T., Tosheva, L., Edge, M., 2017. Reactive magnetron sputtering deposition of bismuth tungstate onto titania nanoparticles for enhancing visible light photocatalytic activity. Appl. Surf. Sci. 392, 590–597.
Ravikumar, C.H., Sakar, M., Mahto, A., Nanjundaiah, R.T., Thippeswamy, R., Teixeira, S.R., et al., 2018. Observation of oxo-bridged yttrium in TiO_2 nanostructures and their enhanced photocatalytic hydrogen generation under UV/visible light irradiations. Mater. Res. Bull. 104, 212–219.
Reli, M., Huo, P.W., Sihor, M., Ambrozova, N., Troppova, I., Matejova, L., et al., 2016. Novel TiO_2/C_3N_4 photocatalysts for photocatalytic reduction of CO_2 and for photocatalytic decomposition of N_2O. J. Phys. Chem. A 120, 8564–8573.
Ren, L., Li, Y.Z., Hou, J.T., Bai, J.L., Mao, M.Y., Zeng, M., et al., 2016. The pivotal effect of the interaction between reactant and anatase TiO_2 nanosheets with exposed {001} facets on photocatalysis for the photocatalytic purification of VOCs. Appl. Catal. B Environ. 181, 625–634.
Rodriguez, M.J.H., Melian, E.P., Santiago, D.G., Diaz, O.G., Navio, J.A., Rodriguez, J.M.D., 2017. NO photooxidation with TiO_2 photocatalysts modified with gold and platinum. Appl. Catal. B Environ. 205, 148–157.
Rolison, D.R., 2003. Catalytic nanoarchitectures-the importance of nothing and the unimportance of periodicity. Science 299, 1698–1701.
Roso, M., Lorenzetti, A., Boaretti, C., Hrelja, D., Modesti, M., 2015. Graphene/TiO_2 based photo-catalysts on nanostructured membranes as a potential active filter media for methanol gas-phase degradation. Appl. Catal. B Environ. 176–177, 225–232.
Roso, M., Boaretti, C., Pelizzo, M.G., Lauria, A., Modesti, M., Lorenzetti, A., 2017. Nanostructured photocatalysts based on different oxidized graphenes for VOCs removal. Ind. Eng. Chem. Res. 56, 9980–9992.
Rosso, I., Garrone, E., Geobaldo, F., Onida, B., Saracco, G., Specchia, V., 2001. Sulphur poisoning of $LaMn_{1-x}Mg_xO_3$ catalysts for natural gas combustion. Appl. Catal. B Environ. 30, 61–73.
Seifvand, N., Kowsari, E., 2015. Novel TiO_2/graphene oxide functionalized with a cobalt complex for significant degradation of NO_x and CO. RSC Adv. 5, 93706–93716.
Seifvand, N., Kowsari, E., 2016. Synthesis of mesoporous Pd-doped TiO_2 templated by a magnetic recyclable ionic liquid for efficient photocatalytic air treatment. Ind. Eng. Chem. Res. 55, 10533–10543.
Shakir, S., Abd-ur-Rehman, H.M., Yunus, K., Iwamoto, M., Periasamy, V., 2018. Fabrication of un-doped and magnesium doped TiO_2 films by aerosol assisted chemical vapor deposition for dye sensitized solar cells. J. Alloys Compd. 737, 740–747.
Shayegan, Z., Lee, C.S., Haghighat, F., 2018. TiO_2 photocatalyst for removal of volatile organic compounds in gas phase-a review. Chem. Eng. J. 334, 2408–2439.
Shu, Y.J., Ji, J., Xu, Y., Deng, J.G., Huang, H.B., He, M., et al., 2018. Promotional role of Mn doping on catalytic oxidation of VOCs over mesoporous TiO_2 under vacuum ultraviolet (VUV) irradiation. Appl. Catal. B Environ. 220, 78–87.
Singh, I., Kumar, R., Birajdar, B.I., 2017. Zirconium doped TiO_2 nano-powder via halide free non-aqueous solvent controlled sol-gel route. J. Environ. Chem. Eng. 5, 2955–2963.
Song, S.Z., Sheng, Z.Y., Liu, Y., Wang, H.Q., Wu, Z.B.A., 2012. Influences of pH value in deposition-precipitation synthesis process on Pt-doped TiO_2 catalysts for photocatalytic oxidation of NO. J. Environ. Sci. 24, 1519–1524.
Song, X., Hu, Y., Zheng, M.M., Wei, C.H., 2016. Solvent-free in situ synthesis of g-C_3N_4/{001}TiO_2 composite with enhanced UV- and visible-light photocatalytic activity for NO oxidation. Appl. Catal. B Environ. 182, 587–597.
Song, F., Bai, L.C., Moysiadou, A., Lee, S., Hu, C., Liardet, L., et al., 2018. Transition metal oxides as electrocatalysts for the oxygen evolution reaction in alkaline solutions: an application-inspired renaissance. J. Am. Chem. Soc. 140, 7748–7759.
Stucchi, M., Bianchi, C.L., Pirola, C., Cerrato, G., Morandi, S., Argirusis, C., et al., 2016. Copper NPs decorated titania: a novel synthesis by high energy US with a study of the photocatalytic activity under visible light. Ultrason. Sonochem. 31, 295–301.
Stucchi, M., Galli, F., Bianchi, C.L., Pirola, C., Boffito, D.C., Biasioli, F., et al., 2018. Simultaneous photodegradation of VOC mixture by TiO_2 powders. Chemosphere 193, 198–206.
Su, C., Tseng, C.M., Chen, L.F., You, B.H., Hsu, B.C., Chen, S.S., 2006. Sol-hydrothermal preparation and photocatalysis of titanium dioxide. Thin Solid Films 498, 259–265.
Sun, H.Q., Wang, S.B., Ang, H.M., Tade, M.O., Li, Q., 2010. Halogen element modified titanium dioxide for visible light photocatalysis. Chem. Eng. J. 162, 437–447.
Sun, H.Q., Ullah, R., Chong, S.H., Ang, H.M., Tade, M.O., Wang, S.B., 2011. Room-light-induced indoor air purification using an efficient Pt/N-TiO_2 photocatalyst. Appl. Catal. B Environ. 108–109, 127–133.
Sun, S., Ding, J.J., Bao, J., Gao, C., Qi, Z.M., Yang, X.Y., et al., 2012. Photocatalytic degradation of gaseous toluene on Fe-TiO_2 under visible light irradiation: a study on the structure, activity and deactivation mechanism. Appl. Surf. Sci. 258, 5031–5037.
Tan, B.Y., Zhang, X.H., Li, Y.J., Chen, H., Ye, X.Z., Wang, Y., et al., 2017. Anatase TiO_2 mesocrystals: green synthesis, in situ conversion to porous single crystals, and self-doping Ti^{3+} for enhanced visible light driven photocatalytic removal of NO. Chem. Eur. J. 23, 5478–5487.
Tang, J.W., Zou, Z.G., Ye, J.H., 2004a. Efficient photocatalytic decomposition of organic contaminants over $CaBi_2O_4$ under visible-light irradiation. Angew. Chem. Int. Ed. 43, 4463–4466.
Tang, J.W., Zou, Z.G., Ye, J.H., 2004b. Photocatalytic decomposition of organic contaminants by Bi_2WO_6 under visible light irradiation. Catal. Lett. 92, 53–56.
Teramura, K., Tanaka, T., Yamazoe, S., Arakaki, K., Funabiki, T., 2004. Kinetic study of photo-SCR with NH_3 over TiO_2. Appl. Catal. B Environ. 53, 29–36.
Thevenet, F., Guillard, C., Rousseau, A., 2014. Acetylene photocatalytic oxidation using continuous flow reactor: gas phase and adsorbed phase investigation, assessment of the photocatalyst deactivation. Chem. Eng. J. 244, 50–58.
Tian, G.H., Chen, Y.J., Meng, X.Y., Zhou, J., Zhou, W., Pan, K., et al., 2013. Hierarchical composite of Ag/AgBr nanoparticles supported on Bi_2MoO_6 hollow spheres for enhanced visible-light photocatalytic performance. ChemPlusChem 78, 117–123.
Tian, M.J., Liao, F., Ke, Q.F., Guo, Y.J., Guo, Y.P., 2017. Synergetic effect of titanium dioxide ultralong nanofibers and activated carbon fibers on adsorption and photodegradation of toluene. Chem. Eng. J. 328, 962–976.
Trapalis, A., Todorova, N., Giannakopoulou, T., Boukos, N., Speliotis, T., Dimotikali, D., et al., 2016. TiO_2/graphene composite photocatalysts for NO_x removal: a comparison of surfactant-stabilized graphene and reduced graphene oxide. Appl. Catal. B Environ. 180, 637–647.
Tryba, B., Wozniak, M., Zolnierkiewicz, G., Guskos, N., Morawski, A., Colbeau-Justin, C.,

et al., 2018. Influence of an electronic structure of N-TiO_2 on its photocatalytic activity towards decomposition of acetaldehyde under UV and fluorescent lamps irradiation. Catalysts 8, 85.
Tsitonaki, A., Petri, B., Crimi, M., Mosbaek, H., Siegrist, R.L., Bjerg, P.L., 2010. In situ chemical oxidation of contaminated soil and groundwater using persulfate: a review. Crit. Rev. Environ. Sci. Technol. 40, 55–91.
Tuprakay, S., Liengcharensit, W., 2005. Lifetime and regeneration of immobilized titania for photocatalytic removal of aqueous hexavalent chromium. J. Hazard. Mater. 124, 53–58.
Wang, Y.Q., Cheng, H.M., Hao, Y.Z., Ma, J.M., Li, W.H., Cai, S.M., 1999. Photoelectrochemical properties of metal-ion-doped TiO_2 nanocrystalline electrodes. Thin Solid Films 349, 120–125.
Wang, S.B., Ang, H.M., Tade, M.O., 2007. Volatile organic compounds in indoor environment and photocatalytic oxidation: state of the art. Environ. Int. 33, 694–705.
Wang, Y.W., Huang, Y., Ho, W.K., Zhang, L.Z., Zou, Z.G., Lee, S.C., 2009. Biomolecule-controlled hydrothermal synthesis of C-N-S-tridoped TiO_2 nanocrystalline photocatalysts for NO removal under simulated solar light irradiation. J. Hazard. Mater. 169, 77–87.
Wang, W.G., Yu, J.G., Xiang, Q.J., Cheng, B., 2012. Enhanced photocatalytic activity of hierarchical macro/mesoporous TiO_2-graphene composites for photodegradation of acetone in air. Appl. Catal. B Environ. 119-120, 109–116.
Wang, H.M., Xie, D., Chen, Q., You, C.F., 2016. Kinetic modeling for the deactivation of TiO_2 during the photocatalytic removal of low concentration SO_2. Chem. Eng. J. 303, 425–432.
Wang, L.L., Zhao, Y.C., Zhang, J.Y., 2017. Photochemical removal of SO_2 over TiO_2-based nanofibers by a dry photocatalytic oxidation process. Energy Fuel 31, 9905–9914.
Wang, H.P., Li, X.B., Gao, L., Wu, H.L., Yang, J., Cai, L., et al., 2018. Three-dimensional graphene networks with abundant sharp edge sites for efficient electrocatalytic hydrogen evolution. Angew. Chem. Int. Ed. 57, 192–197.
Weng, X., Meng, Q., Liu, J., Jiang, W., Pattisson, S., Wu, Z., 2019. Catalytic oxidation of chlorinated organics over lanthanide perovskites: effects of phosphoric acid etching and water vapor on chlorine desorption behavior. Environ. Sci. Technol.
Woan, K., Pyrgiotakis, G., Sigmund, W., 2009. Photocatalytic carbon-nanotube-TiO_2 composites. Adv. Mater. 21, 2233–2239.
Wongaree, M., Chiarakorn, S., Chuangchote, S., Sagawa, T., 2016. Photocatalytic performance of electrospun CNT/TiO_2 nanofibers in a simulated air purifier under visible light irradiation. Environ. Sci. Pollut. Res. 23, 21395–21406.
Xiao, G.C., Wang, X.C., Li, D.Z., Fu, X.Z., 2008. $InVO_4$-sensitized TiO_2 photocatalysts for efficient air purification with visible light. J. Photochem. Photobiol. A Chem. 193, 213–221.
Xie, H., Liu, B.S., Zhao, X.J., 2016. Facile process to greatly improve the photocatalytic activity of the TiO_2 thin film on window glass for the photodegradation of acetone and benzene. Chem. Eng. J. 284, 1156–1164.
Xu, J.H., Li, C.L., Liu, P., He, D., Wang, J.F., Zhang, Q., 2014. Photolysis of low concentration H_2S under UV/VUV irradiation emitted from high frequency discharge electrodeless lamps. Chemosphere 109, 202–207.
Xu, M.X., Wang, Y.H., Geng, J.F., Jing, D.W., 2017. Photodecomposition of NO_x on Ag/TiO_2 composite catalysts in a gas phase reactor. Chem. Eng. J. 307, 181–188.
Yamashita, H., Honda, M., Harada, M., Ichihashi, Y., Anpo, M., Hirao, T., et al., 1998. Preparation of titanium oxide photocatalysts anchored on porous silica glass by a metal ion-implantation method and their photocatalytic reactivities for the degradation of 2-propanol diluted in water. J. Phys. Chem. B 102, 10707–10711.
Yamazoe, S., Hitomi, Y., Shishido, T., Tanaka, T., 2008. Kinetic study of photo-oxidation of NH_3 over TiO_2. Appl. Catal. B Environ. 82, 67–76.
Yan, Y.B., Yu, Y.L., Huang, S.L., Yang, Y.J., Yang, X.D., Yin, S.G., et al., 2017. Adjustment and matching of energy band of TiO_2-based photocatalysts by metal ions (Pd, Cu, Mn) for photoreduction of CO_2 into CH_4. J. Phys. Chem. C 121, 1089–1098.
Yang, L.P., Liu, Z.Y., Shi, J.W., Zhang, Y.Q., Hu, H., Shangguan, W.F., 2007. Degradation of indoor gaseous formaldehyde by hybrid VUV and TiO_2/UVprocesses. Sep. Purif. Technol. 54, 204–211.
Yang, S.B., Chun, H.H., Tayade, R.J., Jo, W.K., 2015. Iron-functionalized titanium dioxide on flexible glass fibers for photocatalysis of benzene, toluene, ethylbenzene, and o-xylene (BTEX) under visible- or ultraviolet-light irradiation. J. Air Waste Manage. Assoc. 65, 365–373.
Yang, Y.L., Li, Y.L., Wang, J.S., Wu, J.S., He, D., An, Q., 2017. Graphene-TiO_2 mesoporous spheres assembled by anatase and rutile nanowires for efficient NO photooxidation. J. Alloys Compd. 699, 47–56.
Ye, J.H., Zou, Z.G., Oshikiri, M., Matsushita, A., Shimoda, M., Imai, M., et al., 2002. A novel hydrogen-evolving photocatalyst $InVO_4$ active under visible light irradiation. Chem. Phys. Lett. 356, 221–226.
Ye, J.H., Zou, Z.G., Matsushita, A., 2003. A novel series of water splitting photocatalysts NiM_2O_6 (M = Nb, Ta) active under visible light. Int. J. Hydrog. Energy 28, 651–655.
Yu, J.C., Yu, J.G., Ho, W.K., Jiang, Z.T., Zhang, L.Z., 2002. Effects of F^- doping on the photocatalytic activity and microstructures of nanocrystalline TiO_2 powders. Chem. Mater. 14, 3808–3816.
Yu, J.C., Ho, W.K., Yu, J.G., Hark, S.K., Iu, K., 2003. Effects of trifluoroacetic acid modification on the surface microstructures and photocatalytic activity of mesoporous TiO_2 thin films. Langmuir 19, 3889–3896.
Yu, C.L., Yu, J.C., Chan, M., 2009. Sonochemical fabrication of fluorinated mesoporous titanium dioxide microspheres. J. Solid State Chem. 182, 1061–1069.
Yu, J.G., Wang, W.G., Cheng, B., Su, B.L., 2009. Enhancement of photocatalytic activity of mesporous TiO_2 powders by hydrothermal surface fluorination treatment. J. Phys. Chem. C 113, 6743–6750.
Yu, J.G., Wang, S.H., Low, J.X., Xiao, W., 2013. Enhanced photocatalytic performance of direct Z-scheme g-C_3N_4-TiO_2 photocatalysts for the decomposition of formaldehyde in air. Phys. Chem. Chem. Phys. 15, 16883–16890.
Yuan, Y., Zhang, J.Y., Li, H.L., Li, Y., Zhao, Y.C., Zheng, C.G., 2012. Simultaneous removal of SO_2, NO and mercury using TiO_2-aluminum silicate fiber by photocatalysis. Chem. Eng. J. 192, 21–28.
Zdravkov, A.V., Gorbunova, V.A., Volkova, A.V., Khimich, N.N., 2018. Preparation of photocatalytically active titanium dioxide doped with transition metal oxides. Russ. J. Gen. Chem. 88, 528–531.
Zehraoui, A., Hassan, A.A., Sorial, G.A., 2012. Effect of methanol on the biofiltration of n-hexane. J. Hazard. Mater. 219, 176–182.
Zhan, Y.J., Ji, J., Huang, H.B., He, M., Leung, D.Y.C., Liu, S.L., et al., 2018. A facile VUV/H_2O system without auxiliary substances for efficient degradation of gaseous toluene. Chem. Eng. J. 334, 1422–1429.
Zhang, J.T., Dai, L.M., 2016. Nitrogen, phosphorus, and fluorine tri-doped graphene as a multifunctional catalyst for self-powered electrochemical water splitting. Angew. Chem. Int. Ed. 55, 13296–13300.
Zhang, Z.B., Wang, C.C., Zakaria, R., Ying, J.Y., 1998. Role of particle size in nanocrystalline TiO_2-based photocatalysts. J. Phys. Chem. B 102, 10871–10878.
Zhang, P.Y., Liu, J., Zhang, Z.L., 2004. VUV photocatalytic degradation of toluene in the gas phase. Chem. Lett. 33, 1242–1243.
Zhang, L., Chen, D.R., Jiao, X.L., 2006. Monoclinic structured $BiVO_4$ nanosheets: hydrothermal preparation, formation mechanism, and coloristic and photocatalytic properties. J. Phys. Chem. B 110, 2668–2673.
Zhang, L.F., Sawell, S., Moralejo, C., Anderson, W.A., 2007. Heterogeneous photocatalytic decomposition of gas-phase chlorobenzene. Appl. Catal. B Environ. 71, 135–142.
Zhang, L.W., Wang, Y.J., Cheng, H.Y., Yao, W.Q., Zhu, Y.F., 2009. Synthesis of porous Bi_2WO_6 thin films as efficient visible-light-active photocatalysts. Adv. Mater. 21, 1286–1290.
Zhang, J., Bang, J.H., Tang, C.C., Kamat, P.V., 2010. Tailored TiO_2-$SrTiO_3$ heterostructure nanotube arrays for improved photoelectrochemical performance. ACS Nano 4, 387–395.
Zhang, D., Pu, X., Ding, G., Shao, X., Gao, Y., Liu, J., et al., 2013. Two-phase hydrothermal synthesis of TiO_2-graphene hybrids with improved photocatalytic activity. J. Alloys Compd. 572, 199–204.
Zhang, L., Qin, M.K., Yu, W., Zhang, Q.H., Xie, H.Y., Sun, Z.G., et al., 2017. Heterostructured TiO_2/WO_3 nanocomposites for photocatalytic degradation of toluene under visible light. J. Electrochem. Soc. 164, H1086–H1090.
Zhang, X.Y., Zhang, Y., Zhou, L.G., Li, X.K., Guo, X.Y., 2018. In situ C,N-codoped mesoporous TiO_2 nanocrystallites with high surface areas and worm-like structure for efficient photocatalysis. J. Porous. Mater. 25, 571–579.
Zhao, Y., Zhao, L., Jing, H., Xu, Y.Y., Wang, S.Q., 2008. Study on method and mechanism for simultaneous desulfurization and denitrification of flue gas based on the TiO_2 photocatalysis. Sci. China, Ser. E: Technol. Sci. 51, 268–276.
Zhao, Y., Han, J., Shao, Y., Feng, Y., 2009. Simultaneous SO_2 and NO removal from flue gas based on TiO_2 photocatalytic oxidation. Environ. Technol. 30, 1555–1563.
Zhao, W.R., Dai, J.S., Liu, F.F., Bao, J.Z., Wang, Y., Yang, Y., et al., 2012. Photocatalytic oxidation of indoor toluene: process risk analysis and influence of relative humidity, photocatalysts, and VUV irradiation. Sci. Total Environ. 438, 201–209.
Zhong, L.X., Haghighat, F., Lee, C.S., Lakdawala, N., 2013. Performance of ultraviolet photocatalytic oxidation for indoor air applications: systematic experimental evaluation. J. Hazard. Mater. 261, 130–138.
Zhou, L., Wang, W.Z., Liu, S.W., Zhang, L.S., Xu, H.L., Zhu, W., 2006. A sonochemical route to visible-light-driven high-activity $BiVO_4$ photocatalyst. J. Mol. Catal. A Chem. 252, 120–124.
Zhou, J.L., Wu, M., Zhang, Y.J., Zhu, C.G., Fang, Y.W., Li, Y.F., et al., 2018. 3D hierarchical structures MnO_2/C: a highly efficient catalyst for purification of volatile organic compounds with visible light irradiation. Appl. Surf. Sci. 447, 191–199.
Zhuo, Y.Q., Huang, J.F., Cao, L.Y., Ouyang, H.B., Wu, J.P., 2013. Photocatalytic activity of snow-like Bi_2WO_6 microcrystalline for decomposition of rhodamine B under natural sunlight irradiation. Mater. Lett. 90, 107–110.
Zou, Z.G., Ye, J.H., Sayama, K., Arakawa, H., 2001. Direct splitting of water under visible light irradiation with an oxide semiconductor photocatalyst. Nature 414, 625–627.
Zou, Z.G., Ye, J.H., Sayama, K., Arakawa, H., 2002a. Photocatalytic hydrogen and oxygen formation under visible light irradiation with M-doped $InTaO_4$ (M = Mn, Fe, Co, Ni and Cu) photocatalysts. J. Photochem. Photobiol. A Chem. 148, 65–69.
Zou, Z.G., Ye, J.H., Arakawa, H., 2002b. Surface characterization of nanoparticles of NiO_x/$In_{0.9}Ni_{0.1}TaO_4$: effects on photocatalytic activity. J. Phys. Chem. B 106, 13098–13101.
Zou, Z.G., Arakawa, H., Ye, J.H., 2002c. Substitution effect of Ta^{5+} by Nb^{5+} on photocatalytic, photophysical, and structural properties of $BiTa_{1-x}Nb_xO_4$ ($0 \le x \le 1.0$). J. Mater. Res. 17, 1446–1454.